1997

The Computational Study of "Model" Pollutants in Clay Montmorillonite

Sung-Ho Park
Loyola University Chicago

LOYOLA UNIVERSITY CHICAGO

THE COMPUTATIONAL STUDY OF "MODEL" POLLUTANTS IN CLAY MONTMORILLONITE

A DISSERTATION SUBMITTED TO
THE FACULTY OF THE GRADUATE SCHOOL
IN CANDIDACY FOR THE DEGREE OF
DOCTOR OF PHILOSOPHY

DEPARTMENT OF CHEMISTRY

BY

SUNG-HO PARK

CHICAGO, ILLINOIS

MAY, 1997

ACKNOWLEDGMENTS

There are so many people who I would like to thank for my study at Loyola. First I would like to thank my advisor, Dr. Alanah Fitch for her sincere guidance. She supported in every way from answering questions to financial support. I also learned a lot from her in reading articles, summarizing ideas, and so on. She is an excellent reader, scientific writer, professor, and play writer. I am sometimes amazed by how much she really can work within a limited time.

I also would like to express thanks to all my committee members. Professor Kenneth Olsen answered questions regarding molecular dynamics simulations. I also learned broad utility of molecular dynamics simulations from his course. He also allowed me to use all the departmental workstations as well as my old friend Indigo, and it really helped me when I had to run several calculations at the last minute.

I also would like to thank Professor Albert Herlinger who I needed to see to get answers for the inorganic questions. He pointed out that not only the chemical probes in my study are inorganic but also clay itself is inorganic. You were absolutely right and I had to understand a lot of inorganic chemistry for the correct considerations in modeling.

I would like to thank Professor Willetta Greene-Johnson who also is a physical chemist with a lot of background in surface chemistry and computational studies. She

recommended that I wait until I got a complete package of software for the simulations instead of making my own codes for the problem. You were definitely right and I acquired a good computational package from MSI/Biosym thereafter.

I also would like to express special thanks to Professor George Schatz at Northwestern University. He served as an outside committee member and was kind enough to help me in several meetings.

I am also indebted to the people in our group including Sean Mellican, Sue Macha, Yunlong Wang, Simona Dragun, Scott Baker, Joe Lohr, and other former group members. I enjoyed working in our group due to their kindness and friendship.

I would like to thank greatly to my parents in Korea. They were so much supportive in many ways that all of my achievements came from them. My sisters, Sung-Hee and Sung-Jee have been supportive and I thank them, too.

During the entire course of study, my wife Yoo-Hee has been cheering me up by playing the piano and by being a nice friend during the ups and downs. I thank you a lot, too. My sons, Peter and Daniel were also helpful simply by showing their lovely faces in front of me. Peter recently told me that he liked to be either a chemist or a medical doctor. I believe that you will need a lot of chemistry and I hope I will be helpful at the time when you need assistance.

Chicago is a wonderful city in terms of many different things. Especially, I enjoyed listening to WMBI (Moody Bible Institute radio) every time I drive back and

forth between my home and the lab. I believe their programs and gospel music help my spiritual health during the study. Therefore, I also thank the people at Moody Bible.

Finally, I would like to express my greatest thanks to the God. He knows all the chemistry and physics from alpha to omega and created me, studying chemistry!

CONTENTS

LIST OF TABLES

Table **Page**

LIST OF FIGURES

Figure **Page**

LIST OF ABBREVIATIONS

CEC	Cationic Exchange Capacity
CME	Clay-modified Electrode
CMS	Clay Mineral Society
CNDO	Complete Neglect of Differential Overlap
HOC	Hydrophobic Organic Compounds
HOMO	Highest Occupied Molecular Orbital
INDO	Intermediate Neglect of Differential Overlap
IR	Infrared (Spectroscopy)
LUMO	Lowest Unoccupied Molecular Orbital
MC	Monte Carlo (Simulation)
MCY	Matsouka-Clementi-Yoshimine (Method)
MD	Molecular Dynamics (Simulation)
MINDO	Modified Intermediate Neglect of Differential Overlap
MSCV	Multi-Sweep Cyclic Voltammetry
MSD	Mean Squared Displacement
PSTHP	Phenylsulfonyl Tetrahydropyran

SCE	Saturated Calomel Electrode
SPCMEs	Spin-coated Clay-Modified Electrodes
TOT	Tetrahedra-Octahedra-Tetrahedra
XPS	X-ray Photoelectron Spectroscopy
XRD	X-ray Diffraction (Technique)
en	ethylenediamine
sep	sepulchrate (1,3,6,8,10,13,16,19-octaazabicyclo[6.6.6]icosane)
bpy	2,2´-bipyridine
bpm	2,2´-bipyrazine
bpz	2,2´-bipyrimidine
$Co(bpy)_3^{2+}$	tris(2,2´-bipyridine)cobalt(2+)
$Co(bpm)_3^{2+}$	tris(2,2´-bipyrimidine)cobalt(2+)
$Co(bpz)_3^{2+}$	tris(2,2´-bipyrazine)cobalt(2+)
$Co(sep)^{3+}$	(1,3,6,8,10,13,16,19-octaazabicyclo[6.6.6]icosane)cobalt(3+)
$Co(en)_3^{3+}$	tris(ethylenediamine)cobalt(3+)
$Co(NH_3)_6^{3+}$	hexaaminecobalt(3+)
$Ru(NH_3)_6^{3+}$	hexaaminеruthenium(3+)

ABSTRACT

The adsorption of $Ru(NH_3)_6^{3+}$, $Co(sep)^{3+}$ (sep=$C_{12}H_{30}N_8$), $Co(en)_3^{3+}$ (en=$C_2H_8N_2$), and $Co(bpy)_3^{3+}$ (bpy = 2,2′-bipyridine) in clay montmorillonite was studied using UV spectroscopy and electrochemistry. The observed potential shift between divalent and trivalent species at clay-modified electrode (CME) was correlated with the calculated adsorption energy difference from lattice minimizations. CME was also used to monitor the diffusion of the metal complexes through the clay over time. Molecular dynamics simulation based on atomistic modeling was performed to compare with these experimental observations. The calculated rate of diffusion measured by mean squared displacement (MSD) was consistent with the observations monitored by CME. The same study was repeated for the divalent cobalt trisbipyridal complexes, $Co(bpm)_3^{2+}$ (bpm = 2,2′-bipyrimidine), $Co(bpy)_3^{2+}$, and $Co(bpz)_3^{2+}$ (bpz = 2,2′-bipyrazine). Relative order of calculated diffusion rate by MSD analysis of these cobalt complexes in clay interlayer region was again consistent with the experimental results. These cobalt tris-ligand complexes were also studied for the quantum mechanical electronic structure calculations. The previously observed divalent ruthenium trisbipyridine complex was used for the computation to make sure if our computational approach is valid. The trends in calculated LUMO energies were consistent with the trends in electrochemical reduction potential of ruthenium trisbipyridine complex. Trends in calculated electronic

transition energies for the metal-to-ligand charge transfer (MLCT) were also consistent with the trends for observed spectroscopic results. Cobalt trisbipyridal complexes were studied for comparison of calculated LUMOs and reduction potentials. Good correlation was obtained for trends with these cobalt tris-ligand complexes. The previously proposed mechanism of electrochemical cleavage of phenylsulfones was elucidated by quantum mechanical electronic structure calculations. The results from the Hartree-Fock calculations were consistent with the proposed mechanism of two electron reduction scheme. The molecular orbital surface and spin density was used to interpret the possible site of electron transfer. The calculated Mulliken and Löwdin bond orders were also consistent with the possible location of reduction of 6-substituted PSTHPs (5-phenylsulfonyl-3,4,5,6-tetrahydropyran-2-one). Overall, the computational technique based on atomistic modeling with molecular dynamics simulation as well as quantum mechanical Hartree-Fock calculations produced good consistency with trends in electrochemical and spectroscopic observations.

Chapter I.

Clay and Clay Minerals

A. Background

1. Contents of Clay

a. Clay, the Definition.

Clay minerals are hydrous aluminosilicates formed at the Earth surface as a result of chemical-weathering of primary minerals in rocks (Bleam et al., 1993). Recently, both the nomenclature committees of AIPEA and CMS reported the agreed definition of clay and clay mineral (Guggenheim et al., 1995). Here, those definitions are rephrased for the better understanding.

The term "clay" refers to a naturally occurring material composed primarily of fine-grained minerals, which is generally plastic at appropriate water contents and will harden with dried or fired. Although clay usually contains phyllosilicates, it may contain other materials that impart plasticity and harden when dried or fired. Associated phases in clay may include materials that do not impart plasticity and organic matter.

The term "clay mineral" refers to phyllosilicate minerals and to minerals which impart plasticity to clay and which harden upon drying and firing.

b. Formation of the clay; The difference from soils

Soils are porous media created at the land surface by weathering processes

derived from biological, geological, and hydrologic phenomena. From the chemical point of view, soils are multi-component, open, biogeochemical systems containing solids, liquids, and gases. Soils exchange both matter and energy with the surroundings such as atmosphere, biosphere, and hydrosphere. These flows of matter and energy cause the development of soil profiles and govern the patterns of soil fertility (Sposito, 1989).

The term clay mineral is often used to refer to minerals with the sheet silicate structures of the phyllosilicates. They are called clay minerals because the clay-sized fraction of many soils consists largely of phyllosilicates, plus small amounts of other crystalline and amorphous materials. Clay minerals also can refer to soil inorganic materials less than 2 μm in effective diameter. Due to its sheet-like structure of phyllosilicates, the term layer silicate is often used as a descriptive name for the clay mineral (Bohn et al., 1979).

c. Structure of Clay Minerals

The scientific importance of clay minerals is due to their large surface and their characteristic lattice structure. This layered structure is a key feature used to distinguish different types of clay minerals:

1) The 2:1 type consisting of two layers of SiO_4-tetrahedrons, all tetrahedrons sharing corners with each other and with an octahedral layer of e.g. $AlO_4(OH)_2$, situated in between. The thickness of this three-layered unit, to be referred to as "platelet", is about 10 Å.

2) The 1:1 type, in which one tetrahedral SiO_4-layer shares corners with an octahedral layer of e.g. $AlO_2(OH)_4$. The thickness of this two-layered unit is about 7 Å.

In both types, aluminum ions in the octahedral layer may be substituted by magnesium ions. This layered structure explains why the clay minerals occur in plate-shaped crystals. One way to visualize this extremely thin clay layer is that the area to mass ratio of these plates is hundreds of square meters per gram (Bolt et al., 1978).

d. What is the Classification of Clay Minerals/Phyllosilicates?

Depending on the number of tetrahedral and octahedral units, clay minerals usually are classified into three layer types, 1:1 layer type, 2:1 layer type, and the 2:1 layer with hydroxide interlayer. With respect to the different kinds of isomorphic cation substitutions, clay minerals are also categorized into five subgroups. The layer types are shown in Figure 1, and the five groups are shown in Table 1.

There are three soil clay mineral groups with this structure in the 2:1 layer type. They are illite, vermiculite, and smectite. Among the smectites, those in which the substitution of Al for Si exceeds that of Fe(II) or Mg for Al are called beidellite, and those in which the reverse is true are called montmorillonite. The sample chemical formula in Table 1 for smectite represents montmorillonite. In any of these 2:1 minerals, the layer charge is balanced by cations that reside on or in the cavities of the basal plane of the oxygen atoms of the tetrahedral sheet. These interlayer cations are represented by M in the chemical formula (Table 1). The 2:1 layer type with hydroxide interlayer is represented by dioctahedral chlorite in soil clays (Sposito, 1989).

Table 1. Clay Mineral Groups

Layer Structure	Clay Group	Layer Charge[1] × -1.0 (e)	Basal Spacing[2] (Å)	CEC[3] (meq/100 g)	Chemical Formula*
1:1	Kaolins (Kaolinite)	< 0.01	7.14	1-10	$[Si_4]Al_4O_{10}(OH)_8 \cdot nH_2O$ (n=0 or 4)
2:1	Smectite (Montmorillonite)	0.5-1.2	12.4-17	80-120	$M_x[Si_8]Al_{3.2}Fe_{0.2}Mg_{0.6}O_{20}(OH)_4$
	Vermiculites	1.2-1.8	9.3-14	120-150	$M_x[Si_7Al]Al_3Fe_{0.5}Mg_{0.5}O_{20}(OH)_4$
	Illite (Hydrous Micas)	1.4-2.0	10.0	~ 30	$M_x[Si_{6.8}Al_{1.2}]Al_3Fe_{0.25}Mg_{0.75}O_{20}(OH)_4$
2:1with Hydroxide	Chlorite	Variable	14.0	10-40	$(Al(OH)_{2.55})_4[Si_{6.8}Al_{1.2}]Al_{3.4}Mg_{0.6}O_{20}(OH)_4$

[1] Sposito, G. *The Chemistry of Soils*; Oxford University Press: New York, 1989.
[2] Tan, K. H. *Principles of Soil Chemistry*; 2nd ed.; Marcel Dekker, Inc.: New York, 1993.
[3] Bohn, H.; McNeal, B.; O'Connor, G. *Soil Chemistry*; John Wiley & Sons, Inc.: New York, 1979.

Figure 1. Clay Layer Types

The figure shows three kinds of clay layer types.

(a) 1:1 layer type; eg. Kaolinite

(b) 2:1 layer type; eg. Montmorillonite

(c) 2:1 layer with hydroxide layer; eg. Chlorite

Blue (dark shaded) spheres are the hydroxides and red (light shaded) spheres are oxygens. The small dots indicate silicon ions (Si^{4+}) and the large dots indicate metal ions (aluminum: Al^{3+}, Mg^{2+}, or Fe^{2+}).

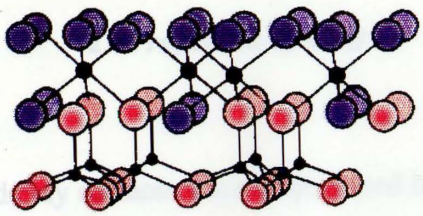

(a)

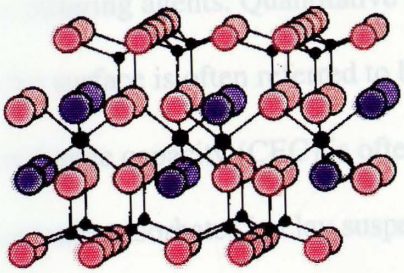

(b)

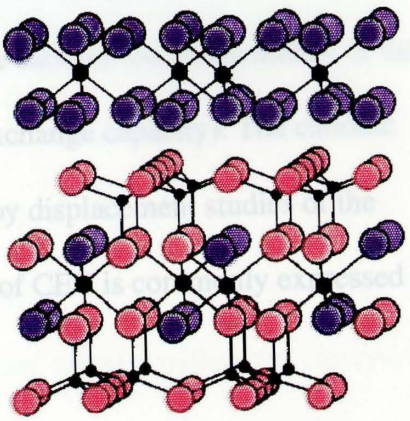

(c)

2. *Properties of Clay*

a. Cationic Exchange

Negatively charged clay surfaces are compensated by cations from the bulk solution, and a cation excess and an anion deficit is found at the surface as a result (Newman, 1987). One common example of this kind is the replacement of the univalent interlayer salt (such as Na^+) by an incoming divalent adsorbate (such as Fe^{2+} and Co^{2+}) or pillaring agents. Quantitative measurements of the cationic exchange ability of the clay surface is often referred to be CEC[1] (cationic exchange capacity). The cationic exchange capacity (CEC) is often calculated easily by displacement studies of the cationic adsorbates in clay suspension. The amount of CEC is commonly expressed in mequiv/g.

b. Colloidal Property

The physical size of a colloid is between 0.01 and 10 μm in its diameter. Water insoluble colloids remain as a solid phase in suspension which are easily visible. The chemical composition of clay colloidal suspension is different depending on the type of the clay. Colloidal suspensions are considered to be stable unless there is a measurable gravitational settling of the suspension over practical time periods (e.g., 2-24 h). Stable suspensions of soil colloids lead to soil erosion and clay illuviation[2] because the

[1] the number of ionic sites on the packing that can take part in the exchange process
[2] The deposition in an underlying soil layer of colloids, soluble salts, and mineral particles leached out of an overlying soil layer.

particles entrained by the soil solution remain highly mobile (Sposito, 1989). Stable suspensions also have an effect on the mobility of inorganic and organic adsorbates. Therefore the chemical transport in clay is also influenced by the colloidal stability.

If the colloidal suspension becomes unstable, gravitational settling leads to coagulation[1]. Depending on the surface chemistry, geometry of the colloids, pH, ionic strength, and composition of the soil suspension, either flocculation[2] or aggregation[3] occurs.

c. Water-Clay Swelling

In clay minerals, Si, Al, Fe, and Mn, and some organic macromolecules are responsible for most wettability properties. Wettability of clay minerals is a crucial problem, faced in various industrial technologies, such as metallurgy (molding sands), drilling fluids, painting, oil refining and decolorization, water clarification, catalysis, and production of ceramics, papers, adhesives, portland cements[4], plastics, rubber, medicines, cosmetics, etc. (Schrader et al., 1992).

For our montmorillonite clay, which is a 2:1 TOT (Tetrahedra-Octahedra-Tetrahedra) type clay, crystalline clay swelling was attributed to the interlayer water content. This interlayer space of a TOT clay mineral is the space between two parallel silicate layers, sandwiched by two oxygen planes of siloxane groups. The clay swelling in the interlayer space is the result of (i) thermal motion of water molecules in the

---

[1] The process by which a colloidal suspension becomes unstable and undergoes gravitational settling.
[2] bulky, settled masses of particles with high water contents
[3] dense and organized masses of settled particles
[4] or Portland cement. A hydraulic cement made by heating a mixture of limestone and clay in a kiln and pulverizing the resulting material.

environment of the mineral, (ii) electrostatic attraction forces between water molecules, and the exchangeable cationic species, and (iii) attraction and dispersion forces between the TOT layers (Schrader et al., 1992). The geometric organization of different types of smectites was related to clay swelling using TEM analysis (Hetzel et al., 1994). Significant uptake of water content causes expansion of the clay crystal along the *c* axis which defines the direction between two parallel silicate layers of clay, and this expansion can be monitored by the use of adsorption isotherms. The interlayer water swelling was measured with XRD (X-ray Diffraction) technique in terms of the c-spacing data (Shang et al., 1995).

In most cases swelling has been determined under air atmosphere or under various controlled humidities. Clay interlayer swelling was studied in aqueous suspensions (Slade et al., 1991) and under the influence of water vapor (Mooney et al., 1952a; Mooney et al., 1952b). Changes in the properties of a water swelled montmorillonite interpreted as a "hysteresis" during the adsorption and desorption of water vapor have been studied (Fu et al., 1990).

3. Environments and Clay

The disposal of nuclear wastes produced by nuclear installations has been a important matter last decades. The most commonly accepted method for disposing of low-level solid wastes is shallow land burial. For high-level nuclear wastes, a deep bedrock repository method has been favored but currently there are no operating sites (Lee et al., 1985). Due to its importance in environmental utility, the sorption properties of clays for dissolved radionuclides in aqueous solutions have been investigated under a

variety of geochemical conditions (Serne et al., 1977). The mechanisms involved in radionuclide removal from liquid phase by clay are ion exchange sorption, chemisorption, and precipitation. Ion exchange of clay was already mentioned above. Chemisorption is usually characterized by a very limited exchangeability of adsorbed ions as a result of the high adsorption energy (Haan et al., 1976). On the other hand, ions which penetrate the coordination shell are bound by covalent bonds directly via their oxide and hydroxyl groups to the structural cation (Schwertmann et al., 1977).

Because the swelling capacity varies among clay minerals, preparation of properly mixed clay has been proposed to control the swelling capacity to have a desired mixture for sealer and backfill material (Chen et al., 1975). In waste disposal and repository systems, clays are potentially effective retardation media for radionuclides in the waste and fluid flow within the hydrologic compartment as in situ mineral components in soils, residua, and host rocks. The chemical and hydrological retardations will delay the transit period from a point source to accessible environment for hundreds to thousands of years. The major portion of radioactivity would decay during the containment periods.

Clay swelling also has played an important role in the petroleum industry. During oil and gas exploration and production, serious problems are frequently encountered in shale formations which contain a high fraction of compacted 2:1 clay minerals such as smectites. These problems include borehole instability, associated with the uptake of water by smectites from the drilling fluid (Boek et al., 1995a; Boek et al., 1995b).

B. Experimental Studies of Clay Adsorption

Pillaring, adsorption, sorption, racemic adsorption, intercalation, interlamellar[1] binding, and surface selective dispersion are the vocabularies that may describe the study of adsorption of material (chemical compounds here) to the clay. There have been numerous reports of clay's adsorption properties due to its ionic (charge bearing) characteristics and large surface areas (van Olphen, 1991; Güven, 1988). The experimental studies of clay adsorption are summarized here because the present study is based on clay-chemical compound interaction (or adsorption).

The sorption of organic cations on soils and clays was first reported by Lloyd in 1916 when he found that fuller's earth adsorbed nicotine from aqueous solution, especially when the alkaloid was in the salt form (Zhang et al., 1993). The definition of the adsorption as the net accumulation of matter at the interface between a solid phase and an aqueous solution phase and the different types of adsorption mechanisms were explained and categorized by Sposito (Sposito, 1989). Clay adsorption studies performed on the colloidal form of clay rather than clay surface may require special attention. The clay-modified electrode study is based on well ordered clay surface while the clay suspension lacks well oriented structure. (See chapter II for more details on well ordered clay structure in clay-modified electrode). Although the basic process or the mechanism to form a clay-chemical adsorption product is attributed mostly to the

---

[1] Lamella means a thin plate or layer in Latin. Therefore interlamellar can be used to describe the region between two thin clay platelets. Also known as interlayer.

coulombic interaction between the adsorbate[1] and the adsorbent[2], the intercalation or interlamellar binding describe more accurately the interaction behavior occurred during the diffusional transport of electrochemical species through the interlamellar region of the clay in CME.

Yamagishi and co-workers found that there is a chiral selectivity in the adsorption of clay with metal complexes by using the colloidal clay (Yamagishi, 1983; Yamagishi et al., 1981; Yamagishi, 1982; Yamagishi, 1985). Binding of the selected enantiomeric[3] and racemic[4] metal complexes with sodium montmorillonite were studied by means of X-ray diffraction and electric dichroism measurements (Taniguchi et al., 1991). Abdo and co-workers reported the photochemical and photocatalytic properties of adsorbed organometallic compounds in the interlamellar space of clay by using infrared spectroscopy (IR) and X-ray photoelectron spectroscopy (XPS) techniques performed on colloidal form of clay suspension (Abdo et al., 1981). Giannelis and Pinnavaia found that the intercalation of metal complexes in smectite clay is governed by the accessibility of Na^+ exchange ions on the basal surfaces[5] (Giannelis et al., 1985b). The same metal complexes are selectively dispersed at or near edge surface sites and the greater degree of cluster dispersion was reported (Giannelis et al., 1985a).

---

[1] A solid, liquid, or gas which is adsorbed as molecules, atoms, or ions by such substances as charcoal, silica, metals, water, and mercury. In this study, the interlamellar cationic complexes.

[2] A solid or liquid that adsorbs other substances; for example, charcoal, silica, metals, water, and mercury. In this study, the clay surface or colloidal form of clay.

[3] One of an isomeric pair of crystalline forms or compounds whose molecules are non-superimposable mirror images.

[4] Often called as racemic mixture, compound which is a mixture of equal quantities of optical isomers (enantiomers).

[5] The surface perpendicular to the long, or c, axis in all crystals except those of the isometric system.

When the intercalated cations function as molecular props or pillars between the silicate layers, they create a highly porous structure with a large intracrystalline surface area suitable for molecular absorption and catalysis (Christiano et al., 1985). Cationic surfactants[1] including quaternary amines and thiol functionalities have been studied heavily recently due to the promoted sorption of hydrophobic organic compounds (HOC) to the modified surface (Wagner et al., 1994; Mercier et al., 1995; Smith et al., 1994; Zhang et al., 1993; Xu et al., 1995). Clay adsorption studies have also been extended to the preparation of the cyclodextrin within the interlayer region of the montmorillonite clay (Kijima et al., 1984). They proposed this immobilized artificial enzyme to model the membrane enzymes.

C. Clay Adsorption Modeling

1.Introduction

Modeling of clay can be attempted in many different ways. Here the basic modeling schemes of clay attempted in the past are reviewed. Past modeling works with clays place more emphasis on Monte-Carlo simulations. Finally, the studies of molecular mechanics and molecular dynamics which most likely represent the clay-intercalated chemical reaction we are interested in are reviewed. Here "clay adsorption" modeling includes adsorption of water (swelling) as well as adsorbate cationic compounds.

[1] Surface-active agent

2. Basic (General) Modeling

Adsorption of nucleotides on homoionic bentonite clays were modeled by semiempirical quantum mechanical calculation INDO (Intermediate Neglect of Differential Overlap) by Liebmann and co-workers (Liebmann et al., 1982). They characterized the binding of five different nucleotides when they are adsorbed in the interlamellar space of bentonite clays. The energetics of complex formation and modes of cation-nucleotide binding were also obtained and the preference of the bindings among nucleotides was studied.

A model to describe the structural disorder in natural kaolinite material was proposed, based on the stacking of two 1:1 layers and their enantiomorphs[1] by Artioli and co-workers (Artioli et al., 1995). Their computer simulations used a general recursive[2] algorithm applied to a new structural model of the stacking disorder based on the X-ray diffraction powder patterns of kaolinites.

A macroscopic energy balance model for crystalline swelling of 2:1 phyllosilicates was devised by Laird (Laird, 1996). The method uses a balance among the potential energies of attraction, repulsion and resistance. They predicted the basal spacing of the clay swelling as a function of interlayer cation and layer charge. However, their modeling results did not support the experimental findings in basal

---

[1] Either of a pair of crystals, molecules, or compounds that are mirror images of each other but are not identical. Also called *enantiomer*.

[2] A function that calls itself, either directly or indirectly, is referred to as recursive function (Lippman, 1993).

spacing. This discrepancy was attributed to the wrong assumption of their continuous and non-hysteretic[1] crystalline swelling.

The electronic structures of the phyllosilicates were investigated using *ab-initio* molecular orbital calculation by Gibbs and Newton (Newton et al., 1980; Gibbs, 1982). They obtained optimized linked silicate (SiO_4^{4-}) tetrahedral structure in terms of bond lengths and bond angles to represent a clay structure. They compared the geometries and charge distributions for H_4SiO_4 and $H_6Si_2O_7$ with experimental values for silicates and siloxanes.

A model for the occurrence of isopotential[2] points in tris(2,2´-bipyridine) cobalt(+2)-montmorillonite clay adsorption/diffusion study on clay-modified electrode was developed in our group (Edens et al., 1991). The results from this model supplied the information of the reaction between the metal complex and the clay as a function of pore size of the clay film and the presence of the competing ion-exchange cations.

British scientists, Skipper and co-workers performed computer calculations of water-clay interactions using atomic pair potentials (Skipper et al., 1989). They used an MCY (Matsouka-Clementi-Yoshimine) model (Matsouka et al., 1976) for water-water interactions. They also proposed the energetically preferable site for water molecules to reside as the top of the interlayer hydroxyl groups located inside of the unique hexagonal holes of silicon oxide tetrahedral layer.

---

[1] The lagging of an effect behind its cause, as when the change in magnetism of a body lags behind changes in the magnetic field. Clay swelling and interlayer cation content is in hysteretic relation.

[2] At isopotential of MSCV (**M**ultisweep **C**yclic **V**oltammogram) of CME, the peak decrease of previously enhanced peak is changed into another peak development. Throughout the MSCV observation, the isopotential point remains at the same potential.

3. Monte Carlo Simulations on Clay Modeling.

Monte Carlo (MC) simulations on the clay adsorption system have been studied by many researchers worldwide during the last 5-6 years. The use of MC on clay was popular because this stochastic Metropolis algorithm has been used for many other liquid phase chemical systems successfully. This method has strong advantages in sampling conformational surface, and this advantageous technique was used to find the clay-adsorbate low energy conformation.

One of the earliest application of MC for the clay system was done by Skipper and co-workers (Skipper et al., 1991). Their use of MC in the study of the interaction between clay, water, and interlayer cations to find a starting point of the clay swelling properties enabled them to calculate the interlayer spacings of hydrated Na and Mg smectites. They proposed an interlayer cation solvation model with water forming octahedrally coordinated 6(H_2O) complexes. The interlayer swelling was attributed to solvation of interlayer cations which they believe hold the clay platelets apart. Relatively good correlation with the experimental results were obtained.

The French scientist Alfred Delville also performed Monte Carlo simulations independently to study the clay-water interface and published his results in the same year as Skipper's group (Delville, 1991). He, however used the water-water potential parameters from TIP4P[1] model of Jorgensen and co-workers (Jorgensen et al., 1983) instead of the MCY used by Skipper's group. He used a MINDO (Modified

[1] In this model, the water molecule is rigid and has four intermolecular interaction sites.

Intermediate Neglect of Differential Overlap) quantum mechanical calculation to determine the parameters for clay-water and clay-cation energies. The phenomenon of clay swelling was again attributed to the solvation of the interlamellar cations. The mean water organization of sodium montmorillonite and the description of the immersion enthalpy were reported to be in a good correlation with the experimental results. Since then, Delville and co-workers have performed series of MC computations to study the clay system. Modeling the organization of water molecules and the interlayer sodium counter ions as a function of the pore width was attempted (Delville, 1992; Delville, 1993). The wettability of the clay minerals is also related to their surface charge and chemical composition (Delville et al., 1993; Delville, 1995).

Skipper and co-workers continued to develop the model for the clay hydration system (Skipper et al., 1995a). Both the effects of simulation cell size and shape and the effects of potential function model were thoroughly studied to prepare a solid methodology of modeling the clay swelling system using Monte Carlo simulations. They then performed MC with their clay system in the form of monolayer hydrate model with the previously developed methodology (Skipper et al., 1995b). They found that water molecules are induced to interact with the siloxane surface oxygen atoms through hydrogen bonding as the percentage of tetrahedral layer charge increases. They also found that sodium counter-ions are induced to form inner-sphere surface complexes. From their simulation, they suggested the need for new careful diffraction study on a series of monolayer hydrates of montmorillonite where the charge of the

interlayer region and isomorphic substitution at the tetrahedral portion of the clay can be systematically varied.

A study of adsorption/desorption hysteresis loops in the swelling process previously observed experimentally by Fu and co-workers (Fu et al., 1990) was also tackled by Monte Carlo simulation (Boek et al., 1995). They conducted a series of simulations in which the interlayer water content is increased systematically from 0 to 300 mg/g of clay. Then the calculated clay layer spacing values as a function of water content were compared with experimental data. They claimed that their simulation established, for the first time, the true equilibrium clay layer spacings of the system.

The role of potassium as a clay swelling inhibitor was studied using MC simulation modeling by Boek and co-workers (Boek et al., 1995). The driving force of their attention on this matter is due to the previously mentioned property of clay to fall apart during oil well drilling through shales.[1] They performed series of MC on different type of montmorillonites which contain sodium, lithium, or potassium cation in the interlayer dimension. Their simulations showed that a water content increase in the interlayer region resulted in the induced hydration of Na^+ and Li^+ which in turn increased the interlayer spacing. However, K^+-montmorillonite didn't show the increased in the interlayer spacing. This experimentally observed behavior was confirmed and attributed to K^+ ion migration and tight binding with the clay surface

[1] In the petroleum engineering, the borehole instability associated with the uptake of water by smectites from the drilling fluid. See Environments and Clay section of Clay, Clay Minerals for further explanation and reference.

instead of solvation.

Sato and co-workers in Japan also studied the same montmorillonite clay system using MC (Sato et al., 1992a; Sato et al., 1992b). They attempted the modeling of the clay system in order to find the theoretical support for their group's earlier finding, 'chirality effects of the clay' (Yamagishi, 1983; Yamagishi et al., 1981; Yamagishi, 1982; Yamagishi, 1985). The free energy of binding, the roles of the upper and lower clay sheets in determining the orientation of a adsorbates, and the effects of water on the binding were studied. They claimed that their simulations of cationic metal complexes as binding guest of the interlayer surface of montmorillonite clay showed a more detailed picture about the bound structure of the chelate than the experimental results. They also performed MC on intercalation of the same metal complexes on a different clay substrate, saponite (Sato et al., 1996).

4. Molecular Mechanics/Molecular Dynamics on Clay Modeling

While numerous works of Monte Carlo simulations were carried out for the study of the clay system, especially in terms of clay swelling and interlayer cation solvation, molecular dynamics (MD) (which has about the same length of history as MC) has only recently been used.[1] While MC has an advantage in conformation searching in the entire system in equilibrium by its stochastic method, MD is more suited for the pre-equilibrium or diffusion properties of the chemical system. Here,

[1] More complete definition of Monte Carlo (MC) and molecular dynamics (MD) will be discussed in Chapter III.

several examples of using MD techniques on clay material are reviewed for understanding of the current activities in this field.

Keldsen and co-workers used the MD technique to calculate the enthalpies of adsorption of series of hydrocarbons on a smectite clay (Keldsen et al., 1994). The rigid model of clay structure was used while the hydrocarbons were allowed to move freely during the course of simulations. Then, two different forcefields, MM2 by Allinger (Burkert et al., 1982) and Hopfinger's forcefield (Hopfinger, 1973) were used to calculate the enthalpy of adsorption both from energy minimization and molecular dynamics. The average error less than 2.0 kcal/mol between the theoretical and experimental data was reported from the molecular dynamics using Hopfinger's forcefield and parameters.

The chiral recognition previously studied by Yamagishi and co-workers (Yamagishi, 1983; Yamagishi et al., 1981; Yamagishi, 1982; Yamagishi, 1985) was chosen for the forcefield study in the form of molecular mechanics by Breu and Catlow (Breu et al., 1995). They performed lattice minimization technique on the 2 dimensional molecular organization of a monolayer of tris(2,2´-bipyridine)cobalt(2+) complexes. They proposed that the chiral recognition of clay is the result of the lateral interactions between the guest complexes as modified by the corrugation of the silicate layer of the clay. Different two dimensional arrangements of ruthenium cation complexes were obtained for enantiomeric and racemic forms. They also reported smaller interlayer spacing from their simulation and claimed that this result is due to a 0 K temperature treatment.

Recently, both molecular dynamics and Monte Carlo simulations were used to study the mechanism of swelling of sodium-montmorillonite clay by Karaborni and co-workers (Karaborni et al., 1996). In their simulation, the distance between the clay layers was fixed after each incremental increase in the interlayer distance, and the system was allowed to take or reject water molecules until equilibrium was reached. Their simulation showed that there are four stable states at basal spacings of 9.7, 12.0, 15.5, and 18.3 angstroms. They claimed that the amount of swelling in terms of basal spacing showed good agreement with the experimental data.

Chapter II.

Clay-Modified Electrode (CME)

A. Introduction

Clay-modified electrode (CME) is an electrode with its electrode surface modified with clay minerals. The modification of electrode and its electrochemistry is also found for other immobilized material at the electrode surface such as zeolites, and many other polymers (Murray, 1992).

The first clay-modified electrode was prepared from mixtures of sodium Wyoming montmorillonite (Na^+ SWy-1) and small amounts of poly (vinyl alcohol) (PVA) by Ghosh and Bard (Ghosh et al., 1983). They prepared the electrodes of about 3-μm thick clay films on tin oxide on glass, Pt, and glassy carbon (GC) substrates. Then the diffusion of some chemicals such as ruthenium (II) trisbipyridium ($Ru(bpy)_3^{2+}$), ferrous trisbipyridium ($Fe(bpy)_3^{2+}$), and methyl viologen (MV^{2+}) were studied by soaking the CME in solutions of these species for cyclic voltammetric (CV) measurements.

Cyclic voltammetric measurements of diffusive chemicals at the clay-modified electrode supply the information about the interaction between clay and the probe molecule. The interaction can be measured by comparing the peak potential of clay-modified electrode to that of bare electrode system. This electropotential shift has been

measured for several metal complexes to find its interaction strength with clay (Liu et al., 1985; Ege, et al., 1985; Fitch et al., 1988). The shift in peak potential was also found to be dependent on the concentration of supporting electrolyte (Fitch et al., 1988; Carter et al., 1987). The electroactive species held within the clay interlayer region in these experiments were also found to show bigger peak currents than those in the bulk. These current enhancements were measured and related to the effective electroactive concentrations within the clay (Liu et al., 1985; Ege et al., 1985). Since pillaring of the clay layer is already found to give weak CV (Cyclic Voltammetric) response (Rudzinski et al., 1986; Itaya et al., 1985), these findings also indicate that there is diffusion of the species through the interlayer region instead of immobile attachment to the clay. Electrochemistry and photochemistry of pillared clay-modified electrodes were studied and a mechanism of electrochemical and photo-electrochemical charge transfer was proposed (Rong et al., 1990). The surface of montmorillonite films are found to be capable of assembling electroactive cationic and anionic pairs through ion-exchange and intercalation mechanism (Petridis et al., 1991).

Rong and co-workers demonstrated that axial ligation of a metalloporphyrin, and consequent modulation of its electrochemical properties, can act to gate electron transfer in bilayer devices composed of a cationic silane polymer and an anionic pillared clay. They observed a pH-sensitive gate for electron transfer to and from the cations adsorbed to the montmorillonite clay. They claimed that their results suggest new possibilities for the preparation of micro-electrochemical devices that are sensitive to specific ligands (other than H^+ used in pH sensors) that bind metalloporphyrins.

In our group, the clay-modified electrode has been used extensively to study many aspects of clay chemistry. The conductivity of a clay-modified electrode was examined and correlation of hydration effects with the electrolyte cation concentration was studied (Lee et al., 1990). The association of face-to-face montmorillonite clay with a metal complex was studied (Fitch et al., 1988). Effect of clay charge on swelling for various clay minerals was studied (Fitch et al., 1995). Effect of clay type on the diffusion property of a clay was also studied (Stein et al., 1996). A dual-electrode for multisweep cyclic voltammetry was used both with the computerized system and without it (Fitch et al., 1993; Stein et al., 1994; Stein et al., 1995). Molecular structure effects on diffusion of cations in clays were studied (Fitch et al., 1996). Diffusional properties of various chemical compounds were measured with CME (Edens et al., 1991; Subramanian et al., 1992; Fitch et al., 1993; Joo et al., 1996; Fitch et al., 1996).

Clay-modified electrodes have attracted the attention of many electrochemists because of the ion exchange properties of the clay and because of the unique structure of the material. The clay-modified electrode is a useful tool to study and model the naturally occurring pollutant transport in our environment (shown in Figure 2). More detailed reviews of the clay-modified electrodes are available (Fitch, 1990; Macha et al., 1997).

B. Immobilization of Clay on Electrodes

The net negative charge of the clay due to the isomorphic substitution in the crystal lattice imparts polarity to the clay. The polar nature of clay allows it to be easily attached to metal surfaces or metal oxide surfaces (polar) which are usually used for

Figure 2. Pollutant Transport

The properties of transport of pollutants (solutes) in clay films are used for clay liners and clay barriers.

(a) Clay is used for the liner in waste disposal site; containment technology shown is above- and below-ground landfill

(b) Clay can also be used for a barrier to protect the water source (river) from possible pollutants from the ground.

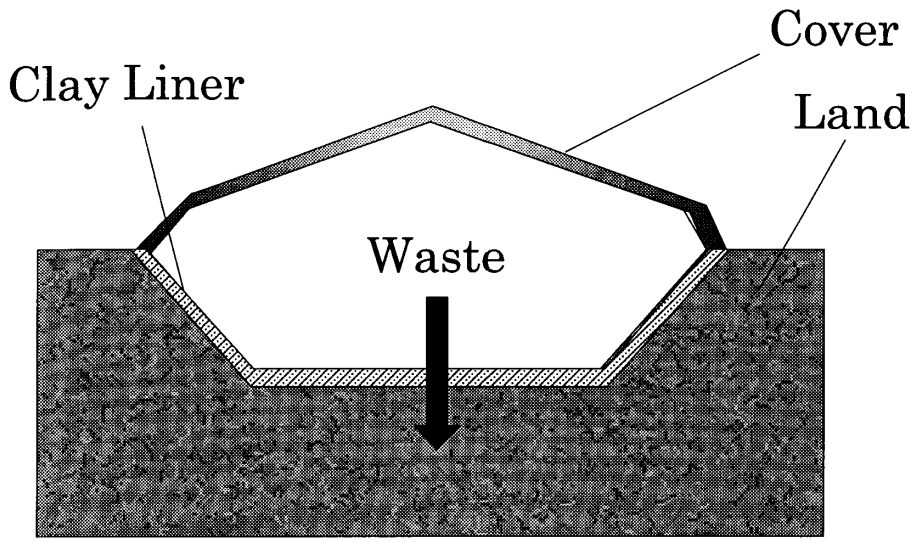
Cover
Clay Liner
Land
Waste

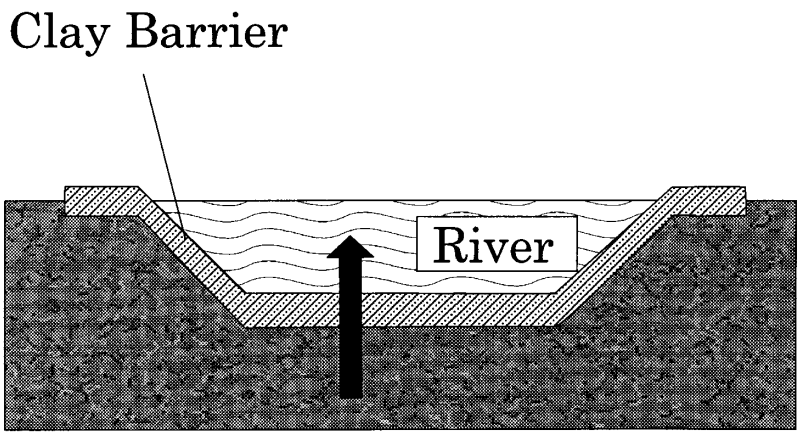
Clay Barrier
River

the electrode surfaces. Therefore, the electrode (e.g., Pt, pyrolytic graphite, etc.) which is encased in a non-conducting material (inert shield) such as glass, Teflon, or Torr Seal is doped with clay mineral. The modification of the entire electrode surface and inert shield must be made. The usual techniques of clay immobilization on electrode used in our lab involves two different methods 1) oven-drying and 2) spin coating. While oven-drying results in the edge-to-face or house of card structure of clay platelets, the spin coated electrode ensures the unique uniform 'well ordered' face-to face clay structure shown in Figure 3. Scanning electron microscopy (SEM) of the clay films generally shows a rough, "waffle-like" structure in which no major cracks or holes found (Bard et al., 1992). The detailed method of spin-coating preparation of CME is given in Method section (Chapter VI).

C. Diffusional Transport Study with CME and This Study

1. Introduction

As mentioned previously, the study of diffusional transport of various chemical compounds through clay-modified electrode is well established laboratory technique in our group. The results from our lab showed that the diffusional property of chemicals through clay is influenced by the size of the interlayer spacing due to salt concentration, clay type, molecular structural effect, and so on. The anion of the host inorganic salt in the clay may also influence the properties of diffusion and this can be studied with CME.

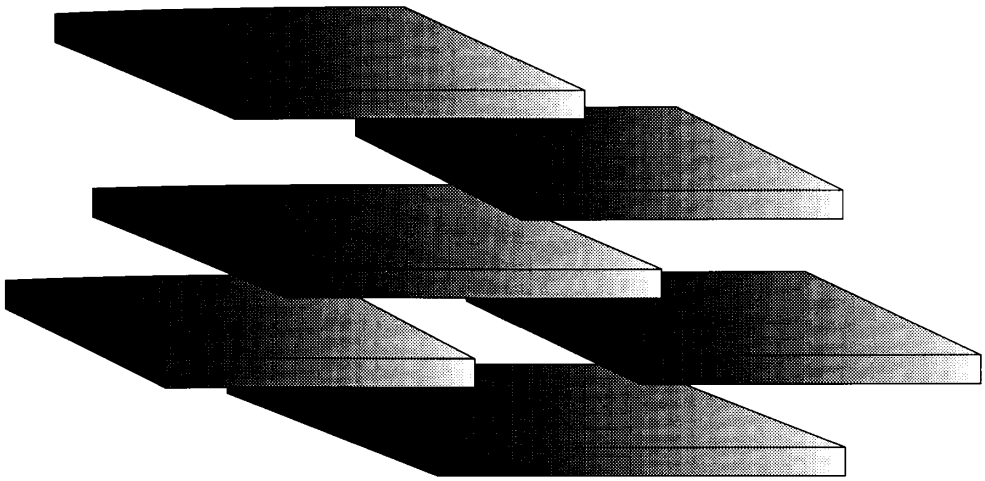

(a)

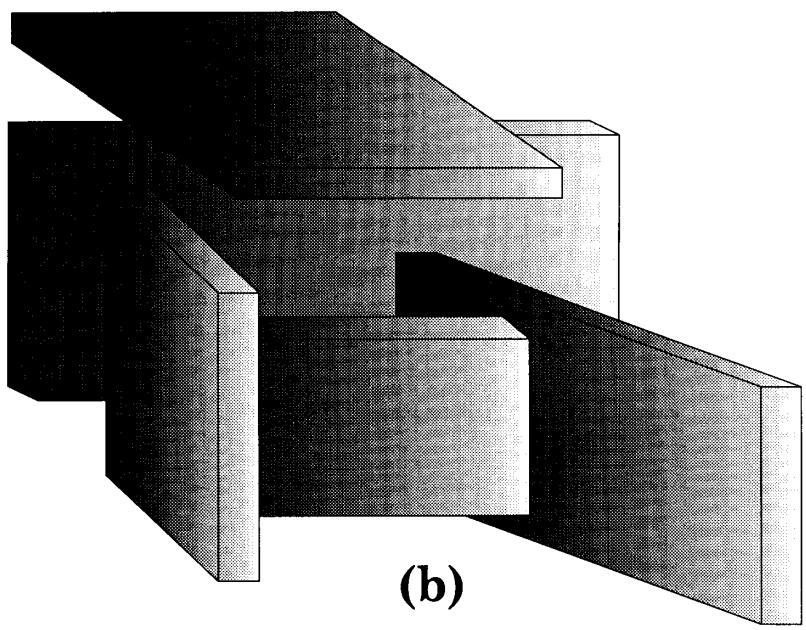

(b)

Figure 3. Face-to-Face and Edge-to-Face Clay Structure
(a) face-to-face (well ordered) clay platelet structure
(b) edge-to-face (house of card) clay platelet structure

Many studies of contaminant transport in clay without using CME have also been done at macroscopic level. Those macroscopic measurements often require high pressure (50~100 MPa) instrumentation and relatively large size (1.0 cm thick by 4.2 cm diameter) of clay sample (Hoh, 1992). HPLC columns packed with the dark sand have been used to study the transport of dissolved organic macromolecules and their effect on the transport of phenanthrene (Magee et al., 1991). The apparatus specially designed by altering of a 50-mL gas/liquid syringe was also used to study the diffusion of an organic compound in soil (Overcash et al., 1991). The effect of compaction on gas diffusion coefficients in soils was studied by Xu and co-workers (Xu et al., 1992). They also used high pressure diffusion chamber. They measured the concentration of N_2 diffusing through metal cores where they applied the pressure to the soil sample. The diffusion coefficient was calculated by fitting an analytical solution of the transient diffusion equation to the measured N_2 concentration in the diffusion chamber as a function of time.

2. Cyclic Voltammetry

Cyclic Voltammetry (CV) is one of the most common and useful techniques in electrochemical analysis. In CV, a triangular potential waveform as shown in Figure 4 is applied to an electrochemical cell. The current measurement of working electrode as a function of the applied potential during this potential scan yields both qualitative and quantitative information about the system used. Because the applied potential varies linearly with time, the horizontal axis of a resulting cyclic voltammogram can be

Figure 4. Triangular Potential Wave and CV for $Fe(CN)_6^{3-}$
(a) Typical excitation signal for cyclic voltammetry: this specific CV scans from E_i (0.8V) to E_s (-0.15V); voltage values are vs. SCE.
(b) Cyclic voltammogram of 6 mM $K_3Fe(CN)_6$ in 1 M KNO_3. The excitation signal for this voltammogram is given above (a) (Sawyer et al., 1984).

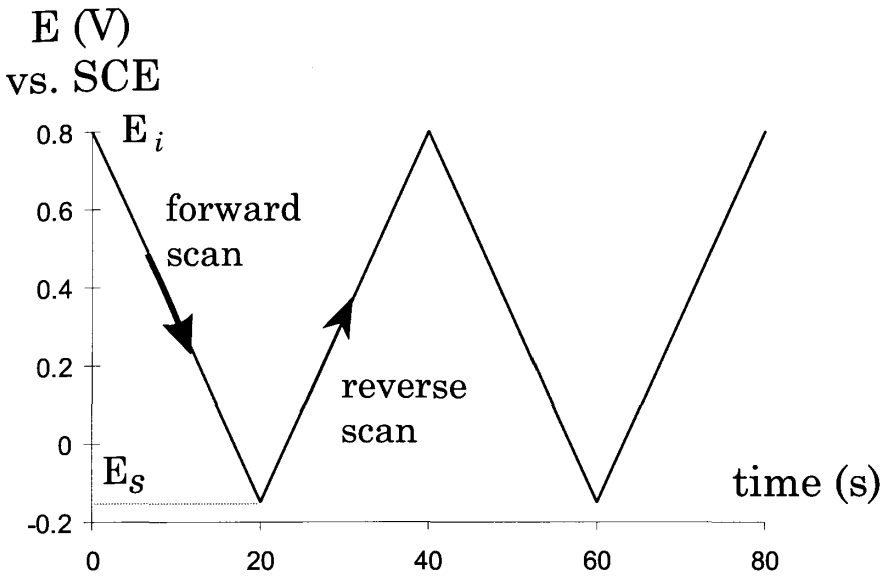
E (V)
vs. SCE
0.8
0.6
0.4
0.2
0
-0.2
E_i
forward
scan
reverse
scan
E_s
time (s)
0
20
40
60
80

(a)

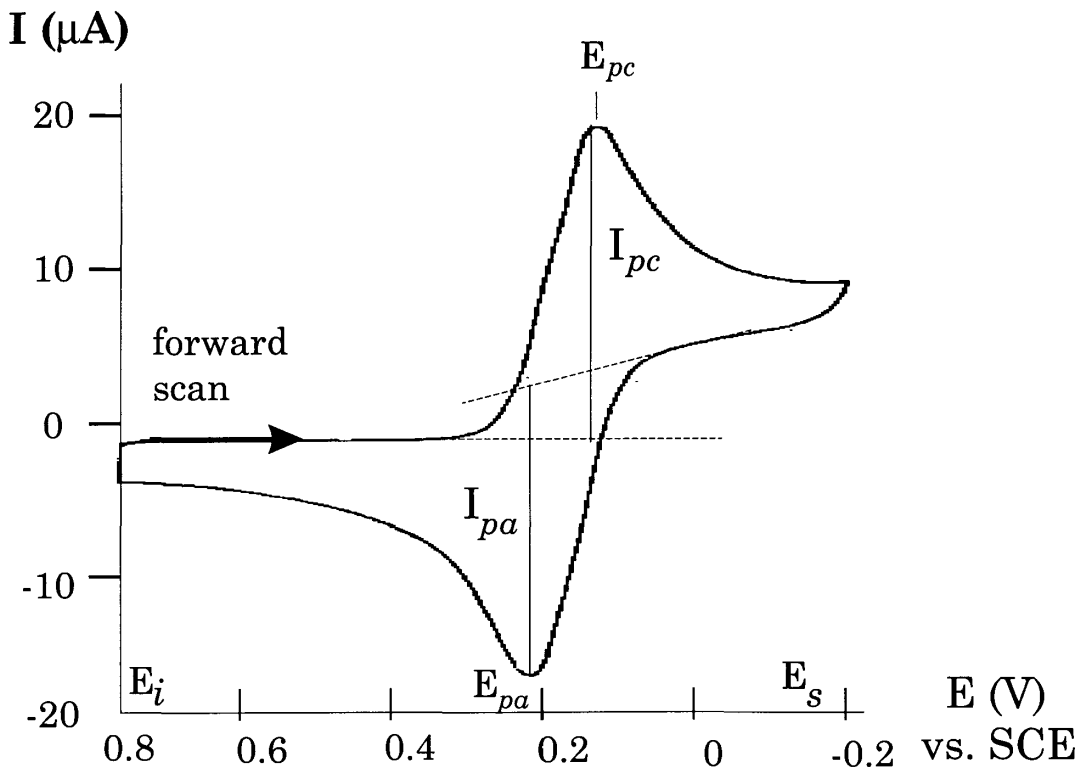
I (μA)
20
10
0
-10
-20
E_{pc}
I_{pc}
forward
scan
I_{pa}
E_i
E_{pa}
E_s
0.8
0.6
0.4
0.2
0
-0.2
E (V)
vs. SCE

(b)

considered as a time axis. One can obtain multiple cycles from same potential scan range to obtain the change of the current with the time change.

A typical cyclic voltammogram is shown in Figure 4. The potential excitation signal used for this voltammogram is shown in Figure 4. The potential is applied from the initial potential, E_i to the switching potential, E_s where the scan direction changes and scanning goes back again to the E_i. The ordinary cyclic voltammogram uses the negative scan direction where E_s is more negative to E_i. The reduction peak is observed from the forward potential sweep (as indicated by the arrow; from E_i to E_s) and the oxidation peak is observed from the backward potential sweep (from E_s to E_i). The formal potential $E^{o\prime}$ for the reduction for a reversible redox[1] couple is then obtained from the midpoint between the two current peaks.

$$[1] \qquad E^{o\prime} = \frac{E_{pa} + E_{pc}}{2}$$

where E_{pa} is the anodic peak potential from the oxidation peak and E_{pc} is the cathodic peak potential from the reduction peak.

When the reduction process is reversible, the peak current at room temperature is given by the Randles-Sevcik equation:

$$[2] \qquad i_p = 2.69 \times 10^5 n^{3/2} A D^{1/2} C^b v^{1/2}$$

where i_p is the peak current observed in amperes (A), n is the number of electrons involved in the reduction process, A is the area of the electrode in cm^2, D is the

[1]reduction-oxidation

diffusion coefficient for the oxidized species in cm^2/s, C^b is the bulk concentration of the oxidized species before the electrochemical perturbation is applied, in $mole/cm^3$, and v is the applied potential scan rate in V/s.

3. Diffusion Information from Clay-modified Electrode

The peak current at a clay-modified electrode (see Figure 5) is described by the equation (Fitch et al., 1995):

$$[3] \qquad I_p = 2.69\times10^5 n^{3/2}\left(d\sum_i^m b_i\right)\left(\tau D_{clay}\right)^{1/2}\kappa C^b$$

where n is the number of electrons in redox system, m is the total number of clay platelets, ($d\,\Sigma b$) is the interlayer dimension available for charge transport composed of interlayer spacing of the clay (d) and the length of the clay platelet edge (b_i), τ is the tortuosity factor accounting for the lateral drag along the surface due to clay's plate-like structure, D_{clay} is the clay diffusion coefficient assumed to apply within the clay-modified film of CME, κ is the partition coefficient between the clay domain and the bulk solution, and C^b is the concentration of the electroactive species in the bulk solution (see Figure 5).

Often current at the clay-modified electrode (i_p(CME)) is normalized by the current at the bare electrode (i_p(bare)):

$$[4] \qquad R = \frac{i_p(CME)}{i_p(bare)} = \left(\tau^{1/2} d\sum b/A\right)\left(D_{clay}/D_{sol}\right)^{1/2}\kappa$$

Figure 5. Clay-modified Electrode and Clay Interlayer Dimensions

(a) A typical clay-modified electrode; Pt wire is sheathed in glass and modified with 5 to 10 μm of clay which swells in contact with solution. An electroactive probe (A) diffuses through the clay to the Pt surface where a potential perturbation causes the reduction of the probe (A^-). A depletion or diffusion region near the surface (~0.15 μm) as a result of the potential perturbation at the time of reduction is also shown.

(b) A schematic diagram showing well ordered thin (5μm) clay film; d is the gallery dimension or interlayer spacing for well swollen clay in NaCl solution and b is the length of the clay platelet edge. The direction of the diffusional transport through the clay interlayer spacing is also shown.

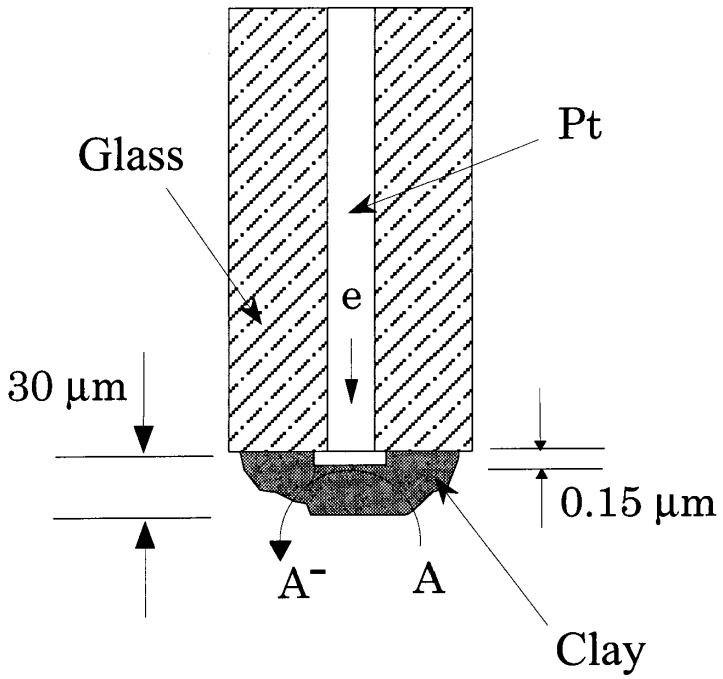

(a)

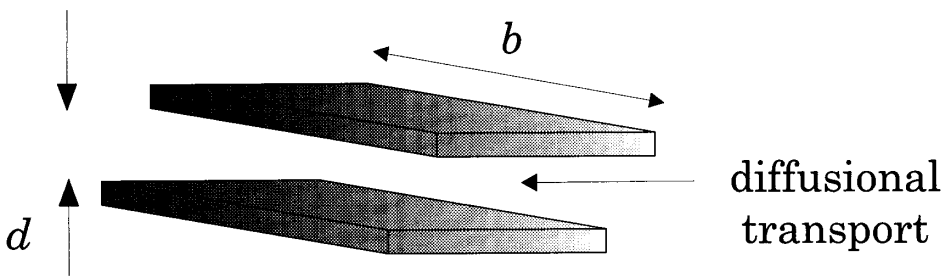

(b)

where D_{soln} is solution diffusion coefficient (cm/s^2) and A is the area of underlying electrode. Here, b *and* τ are constants for a given clay. The interlayer spacing d due to swelling is also constant for the same concentration of electrolyte. By using the same electrode throughout the experiments for the different probes, A is also constant. The constant value of $\tau^{1/2}d\Sigma b/A$ was observed from the transport of an un-retained complex where κ is 1 (Fitch et al., 1988).

If we assume D_{soln} and κ are similar for the metal complex probes of our interest, R is proportional $D_{clay}^{1/2}$. Therefore the ratio of the cathodic peak height of clay-modified electrode to the cathodic peak height of bare electrode for a given probe supply the information about the diffusion constant in clay as described above. In addition, by comparing R vs. time plot for different probes obtained from multisweep cyclic voltammetry, we can compare the diffusional properties of the probe molecules through the clay interlayer region with respect to time.

4. Intermolecular Differences in Diffusive Probes

The accumulation of the diffusional transport data in our clay system has been our focus on the study with CME. We found that there are structural or some internal differences among the diffusive molecules which make their diffusional characteristics unique in terms of cyclic voltammetry. Questions regarding these intermolecular differences in diffusive probes lead to this study. Our goal is to find out how molecular differences produce the different diffusional properties. The internal differences in terms of electrostatic charge which is attributed to the major long range interaction between

clay and host diffusive molecule was tackled by the quantum mechanical study at the atomic level. The "how it makes the diffusion different" part has been studied through Molecular Dynamics Simulation which combined the atomistic electrostatic charge data as one of input parameter.

Chapter III.

Computational Chemistry

A. History

The first great use of the computer in the name of computational chemistry was found in 1953. The first type of computer simulation of a liquid using 'Monte Carlo' method (this statistical stochastic method will be discussed later in this chapter). This first time big scale computational chemistry activity was performed by Metropolis and co-workers (Metropolis et al., 1953) with the computer called MANIAC at the Los Alamos National Laboratories in the United States. The MANIAC (Mathematical Analyzer, Numerical Integrator And Computer) was one of the most powerful computer at that time. MANIAC was the copy of the previous computer developed called EDVAC (operational as of 1951) which came just after ENIAC, the world's first ever stored program computer built by J. Presper Eckert and John Mauchly of the Moore School of Electrical Engineering at the University of Pennsylvania. MANIAC was originally funded by military and first sent to Los Alamos National Lab in 1952 for the hydrogen bomb design. It has been there for 10 years and the dimension was 3 feet x 8 feet x 100 feet with a 20 ten-digit number memory capability and with the speed of 800 operations per second. The 10 years of MANIAC's service recorded more calculations than those

of 800 operations per second. The 10 years of MANIAC's service recorded more calculations than those by entire human race until that time. One can visualize the size and the complex shape of the computer by comparing it to the telephone network. One can also realize the rapid development of computer technology when comparing MANIAC with its descendent 'Paragon' built in 1994 by Intel Corporation with the size of 6 feet x 4 feet x 18 feet, 2000 processors, 120 Gigaflops, 64 Gigabytes of memory, and 20 million dollar price. (See Figure 6).

One can imagine how the computational chemistry researchers were system availability dependent when he or she finds how often Bernard Ransil, one of the most prominent scientists in the field of quantum mechanical computation at the time, had to fly from Chicago, Illinois to Dayton, Ohio to use the UNIVAC computer, one of the rare computers at the time belong to Wright Field Air Force Base. Since the famous physical chemist ROBERT S. MULLIKEN[1] at the University of Chicago attracted the attention to his quantum mechanical study, Ransil at the same institution developed a program for computing open shell LCAO-MO-SCF wavefunctions (Mulliken, 1989).

The introduction of computers in chemistry was relatively fast (see Figure 7 for the milestones in computer hardware development). The mathematical stochastic Monte Carlo approach (Metropolis et al from Los Alamos National Laboratories in 1953), the first extensive molecular orbital calculation (Ransil et al from the University of Chicago in 1955), and the first Molecular Dynamics calculation (Alder et al, 1957; Alder et al.,

[1] 1966 Nobel Prize Laureate for his fundamental work concerning chemical bonds and the electronic structure of molecules by the molecular orbital method

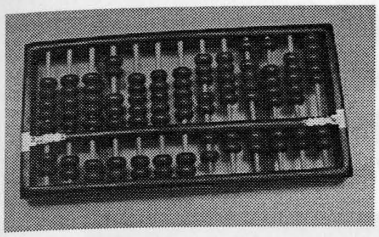

Abacus

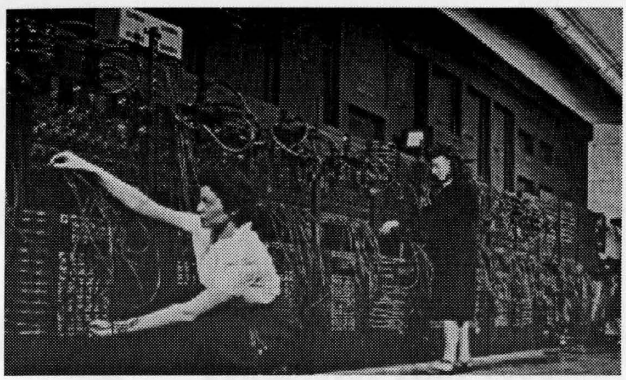

ENIAC

PARAGON

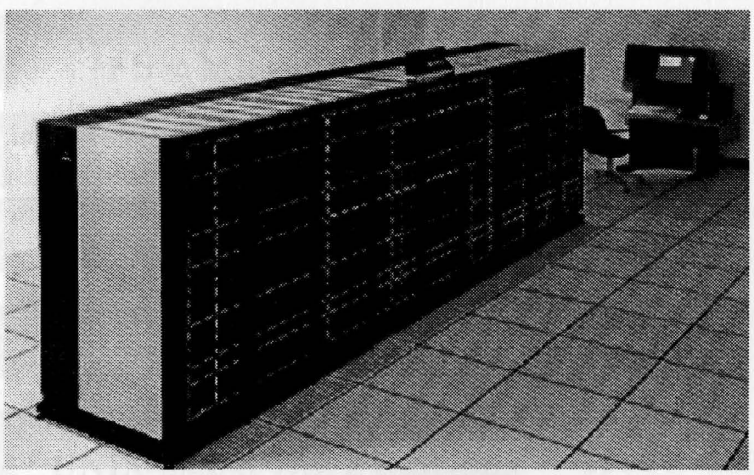

Figure 6. Computer Hardware Development (Speed and Power).
(a) Chinese abacus (2000 B.C.)
(b) ENIAC; the first stored program computer (1951)
(c) Paragon; 120 gigaflop supercomputer (1994)

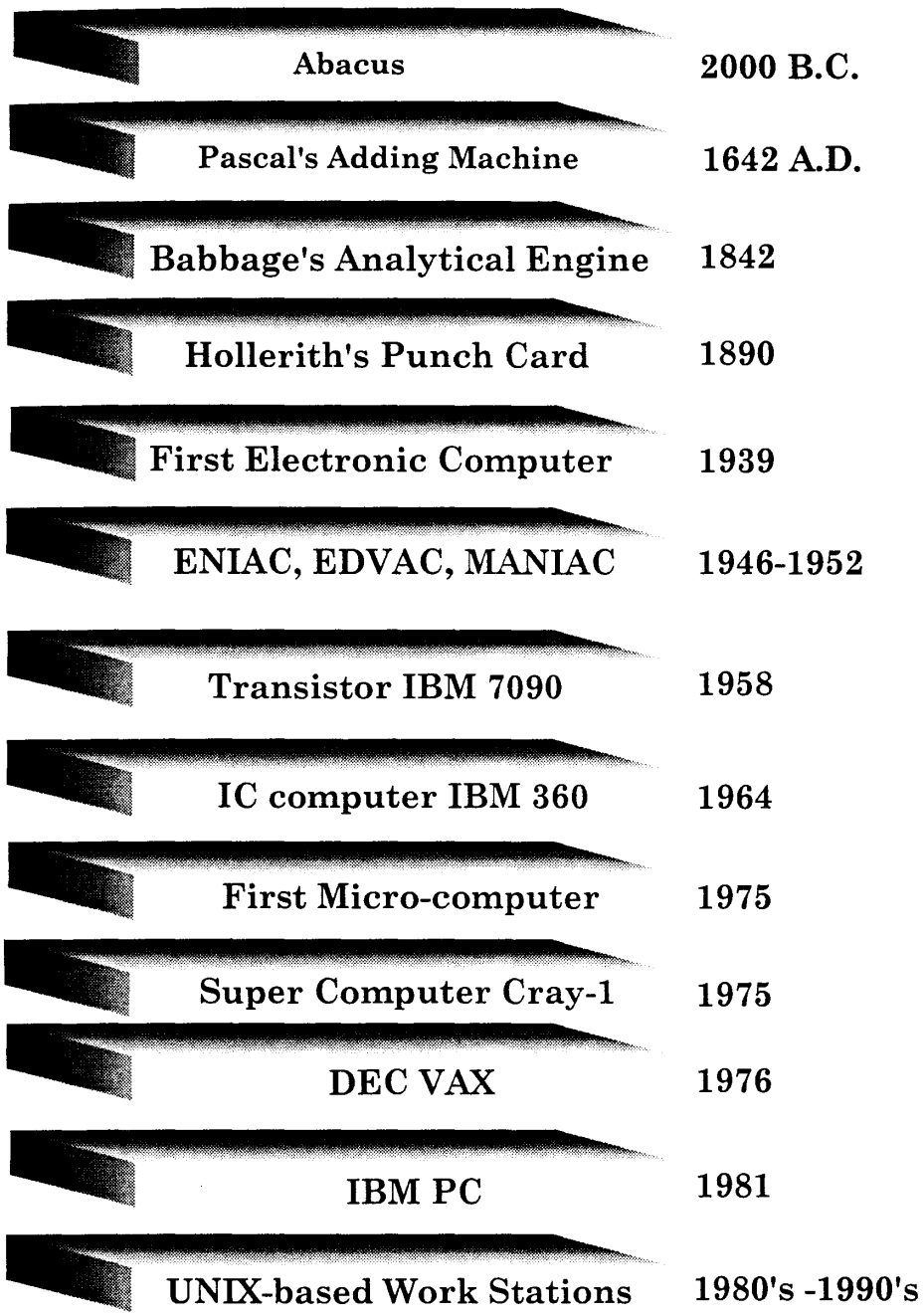

Figure 7. Computer Hardware Development (Chronology).

1959) are the prominent leaders in the computational chemistry. The smart use of computers with in-depth physical chemical background, with findings from experimental organic chemistry, or with the good understanding of more complex biological system made many chemists move forward in this relatively new field of chemistry. John A. Pople and W. Kohn developed quantum mechanical calculation methods based on the approximate solution of Schrödinger equation (Pople et al., 1954; Kohn et al., 1965). Organic chemist E. J. Corey at Harvard made the first application of computers to synthetic chemistry, through the use of machine computation to generate the chemical pathways for the synthesis of complicated organic molecules (Corey et al., 1969). Large molecules such as proteins have been studied by Karplus et al with the molecular dynamics simulation technique which has become a model for the computational biochemistry (McCammon et al., 1977, *267*, 585-90).

B. Application of Computer Simulations in Liquids

1. Introduction

For the study of chemical reactions, computer simulations have been used to answer many of the questions arising from the experimental findings. How do chemical reactions take place? The study of equilibrium kinetics, transition state, photo-reaction, and diffusion are some of the examples of such questions arising from everyday experimental chemistry. Most of these phenomena occur in the liquid phase into which neither the perturbation of ideal gas nor the perturbation of the independent harmonic

oscillator model for solids may fit. The liquid system with these inherent difficulties of the theoretical treatment demands a more powerful numerical statistical treatment.

One of the earliest models of liquids without use of the computer goes back to Morrel and co-workers (Morrell et al., 1936) and Rabinowitch and co-workers (Rabinowitch et al., 1936). Both groups used rigid balls to represent the liquid system either by packing or caging large numbers of balls. Although their approach is macroscopic rather than a microscopic system to represent the real liquid phase, they could look at the dynamics of individual atoms and molecules and use that information to understand the solution reaction process. The physical models have inaccuracies arising from unwanted gravity. Current computational methods can alleviate some of these inaccuracies.

As previously stated, 'Monte Carlo' and 'Molecular Dynamics' simulations are the two big monuments of studying the liquid system. Both of these independently developed techniques study particles in liquid phase and they share certain features or methodology, however there are still some significant differences. These will be discussed in the subsequent sections.

2. Monte Carlo Simulation (MC)

The method of Monte Carlo simulation is often called a Metropolis method since it is introduced by Metropolis and co-workers (Metropolis et al., 1953). Monte Carlo techniques in general provide data on equilibrium properties only whereas MD gives pre-equilibrium properties and transport properties as well as equilibrium properties.

As indicated by its name, MC is a stochastic method which uses random numbers to generate a sample population of the system from which one can determine the properties of interest. As stated earlier, the random nature (even if it is much more complex to treat than the gaseous system) of the particles in liquid phase made this MC as a popular tool to study liquid phase chemistry. The Metropolis algorithm allows one to calculate expectation value of property F from a canonical ensemble[1] using the equation:

$$[5] \qquad < F >= \frac{\int F e^{-E/k_B T} dqdp}{\int e^{-E/k_B T} dqdp}$$

where $<F>$ is the expectation value of property F, k_B is the Boltzmann constant, T is the temperature of the system, $dqdp$ is a volume element in phase space[2], and E is the energy of the system. This integral is not trivial to solve analytically. A numerical simulation with a sufficiently large sample is required. The F calculated from the simulation with N_c, the number of total sample configurations considered, is written as:

$$[6] \qquad F = \frac{\sum_{c=1}^{N_c} F_c e^{-E_c/k_B T}}{\sum_{c=1}^{N_c} e^{-E_c/k_B T}}$$

where F_c and E_c are the property and the energy at configuration c, respectively. The complex analytical integration over the phase space is now replaced by the numerical

[1] also called as NVT ensemble because the number of particles, the volume, and the temperature of the system are constant.

[2] phase space in canonical dynamics is composed of q_x, q_y, q_z, p_x, p_y, and p_z considering heat transfer and momentum change over the 3 D space.

summation over a large number configuration set.

A particle selected at random is moved in a random way within the prescribed limits, and it will have new configuration. According to Metropolis algorithm, this configuration is selected depending on the Boltzmann factor e^{-E_c/k_BT} before and after the move. If the new configuration, E_{c+1} is smaller than that of E_c, the new configuration is accepted. Otherwise, the acceptance of the new configuration is controlled by selecting a random number i ($0 < i < 1$), and comparing it in following way:

(1) If $e^{-(E_{c+1}-E_c)k_BT} < i$, accept the new configuration.

(2) If $e^{-(E_{c+1}-E_c)k_BT} \geq i$, keep the original configuration and start new selection of an atom randomly for another displacement in the space and calculate E_{c+i} - E_c. Then step (1) is repeated.

Over the course of perhaps several hundred thousand to several million attempted steps, a large number of energetically accessible configurations of the system are acquired. This collection of energetically accessible configurations, or the states, is called an ensemble. Thermodynamic and other properties of the system can be computed as ensemble average during the simulation. Some properties converge more rapidly than others. For example, average internal energy may converge relatively quickly, but heat capacity may require a much large ensemble sample to compute reliably.

The random nature of Monte Carlo simulation makes it a useful tool for sampling conformational space. Although the efficiency of sampling conformational

space is not as great as MD, the power of MC is in the fact that it can search much more space in a stochastic way which is impossible in the case of MD simulation. For instance, the Dihedral Probability Grid Monte Carlo method can rotate a dihedral angle in a single step without regard to an energy barrier which might prevent the same rotation in molecular dynamics (Mathiowetz, 1993). Monte Carlo simulation is good for coarse-grained sampling of conformational space while MD technique with forcefield minimization is a good tool for the complementary searching for the optimized conformation.

3. Molecular Dynamics Simulation (MD)

The Molecular Dynamics method was introduced in chemistry in 1957 to solve chemical problems in liquids. In MD, the motion of particles in a system is simulated as they react to forces caused by interactions with other particles in the system while MC stochastic treatment neglects these interactions. Therefore, this dynamic feature of MD allows us to study time-dependent processes occurring in chemistry.

Molecular Dynamics calculations evaluate the forces acting on each particle and use these to determine the accelerations these particles undergo. Particle velocities are initially determined by a random distribution calibrated to give a Maxwell-Boltzmann distribution at a given simulation temperature, then the following velocities are updated according to the calculated accelerations. The trajectory of each particle (each atom in the molecule) is then obtained by solving classical Newtonian dynamics over time for the system. If there are N number of atoms in the molecule and each atom is denoted by subscript *i*, the forces acting on atom *i* are:

[7] $$F_i(t) = m_i \frac{\partial^2 r_i(t)}{\partial t^2}, \; i = 1, N \; (N \equiv number\ of\ atoms)$$

where $F_i(t)$ is the force on atom i at time t, $r_i(t)$ is the position of atom i at time t, and m_i is the atomic mass. The force on atom i at time t is also defined as the negative gradient of the potential energy function:

[8] $$F_i = -\frac{\partial}{\partial r_i} V(r_1, r_2, \cdots, r_N)$$

where $V(r)$ is the potential energy at position r. The analytical solution of the integration of this equation of motion is not trivial and many algorithms have been introduced to solve the motion. One of the most welcomed algorithms in the field of MD may be the summed Verlet algorithm (Swope et al., 1982) which is known to be more accurate and less sensitive to numerical error than the previously introduced standard Verlet (Verlet, 1967). The summed Verlet algorithm is often called a 'leapfrog formulation' due to its updating of velocities and coordinates at every half-time step intervals (Berendsen et al., 1984). The velocities at time increment $n + ½$ are obtained from the previous velocities and the new accelerations:

[9] $$v_{n+\frac{1}{2}} = v_{n-\frac{1}{2}} + hF(t_n)$$

where h is the time increment and t_n is the time at nth step.

The new velocities $v_{n+1/2}$ are then used to update the coordinates for time step $n+1$:

[10] $$R_{n+1} = R_n + hv_{n+\frac{1}{2}}$$

where R_n is the nth coordinate, h is the time increment, and $n_{n+1/2}$ is the new velocity at time increment n+1/2. The resulting coordinates are then the inputs in computing of forces at the current conformation. This process is repeated until the desired time period is reached. Therefore, the simulation of a molecule is no longer stochastic but deterministic with respect to the time dependent trajectory through the potential surface. The usual length of dynamics varies from several to a thousands of picoseconds (nanoseconds).

While the integrating classical Newtonian description of equations of motion alone can give us information regarding the constant-energy surface, one may wish to explore the equilibrium thermodynamic properties of a system. If a microscopic dynamic variable A takes on values $A(t_n)$ along the trajectory at the time step t_n, then the following time average:

[11] $$A = \lim_{t\to\infty} \frac{1}{t} \int_0^t A(t_n)dt$$

will give the measured thermodynamic value for the selected variable. This dynamics variable can be any function of the coordinates and momenta of the particles of the system. Through time averaging one can compute properties such as internal energy, kinetic energy, and pressure regardless of the type of ensemble employed. However, properties like specific heats, compressibilities, and elastic constants depend upon the type of ensemble used. Therefore, it is important to choose a correct ensemble to perform the dynamics simulations. Constant NVT (constant number of particles, volume, temperature) dynamics, called canonical dynamics, has been used for this

study. Other types of ensemble such as constant NVE (microcanonical; constant number of particles, volume, energy) and constant NPT (constant number of particles, pressure, temperature) ensembles are also available.

For the canonical dynamics simulation, the temperature (T) is held constant by coupling to a thermal bath. Nosé (Nosé, 1984; Nosé, 1984) and Hoover (Hoover et al., 1985) suggested different methods of thermal coupling for canonical dynamics. Canonical dynamics using Hoover's heat bath gives the trajectory of particles in real time while the molecular dynamics based on Nosé's bath does not give the trajectory of particles in real time due to its time scaling method. Therefore, for a real time evaluation of the system, Hoover's heat bath should be used for the canonical MD.

Constant NPT dynamics should only be used for periodic systems where the size and shape of the unit cell may vary to accommodate the volume change. Microcanonical ensemble (constant energy and volume) dynamics and constant enthalpy (constant NPH) dynamics are also used in the MD simulations and details are explained elsewhere (Allen et al., 1989).

Chapter IV.

Quantum Mechanical Electronic Structure Methods

(Molecular Orbital Calculations)

A. Introduction

The theory of quantum mechanics began in the 1920's with the goal to study chemical interactions. The first reliable calculations were performed by Hartree in the 1930s using a hand held calculator and applying the Self Consistent Field (SCF) method. Due to the rapid development of computer along with efforts to develop the basis sets for more complicated systems, it is now possible to utilize this convenient tool to the molecular systems including all main group elements and many transition metal elements in many cases. The solution of the Schrödinger equation however, is still based on the one-electron representation systems.

The theoretical background shown here is brief. The detailed theory of classical Hartree-Fock type molecular orbital calculation is also found in reviews (Zerner, 1991; Cioslowski, 1993), 1-33), books (Hehre et al., 1986; Pople et al., 1970), and theses including the thesis by the author of this study (Park, 1994).

Quantum mechanical calculations view a molecule as a collection of point-like nuclei and electrons with fixed masses and charges. The energy terms include the kinetic energy of each particle and the coulombic energies between the particles (repulsion between nuclei, attraction between the nucleus and an electron, and repulsion between electrons).

The time-independent Schrödinger equation used in quantum mechanical calculations is:

[12] $H\Psi = E\Psi$

where E is the total energy, Ψ is the molecular wave function from which all chemical properties can be calculated, and H is the molecular Hamiltonian:

[13] $$H = \sum_i \left(\frac{-m_i}{2} \nabla_i^2 + \sum_{j \neq i} \frac{q_i q_j}{r_{ij}} \right)$$

where m_i is the mass, q_i is the coulombic charge of particle i, and r_{ij} is the distance between particle i and particle j. ∇_i^2 is the Laplacian operator applied to particle i:

[14] $$\nabla_i^2 = \frac{\partial^2}{\partial x_i^2} + \frac{\partial^2}{\partial y_i^2} + \frac{\partial^2}{\partial z_i^2}$$

The kinetic energy is shown in the first term and the coulombic interaction is shown in the second term. The subscript i and j denotes the summation is over all electrons and nuclei. Only certain solutions are allowed and hence the equation is an eigenvalue function where E is the eigenvalue and Y is the eigenfunction. The square of the wavefunction is the physically observed property called "electron density".

The Schrödinger equation can not be solved analytically without approximations. Time independency, neglect of relativistic[1] effects, Born-Oppenheimer approximation, and orbital approximation as a combination of mathematical functions (orbitals) are the approximations implemented in quantum mechanical molecular orbital theory (Boyd, 1990). The treatment of the motion of the nucleus as independent from the motions of the electrons make the computation simpler. Under these conditions, the potential energy surface is only a function of the nuclear position. This is called "Born-Oppenheimer Approximation". The potential energy of a diatomic molecule as a function of inter-nuclear distance is shown in Figure 8. **M**olecular **o**rbitals are approximated by a **l**inear **c**ombination of **a**tomic **o**rbitals (LCAO-MO method). Iterative calculations continue until the solution of the total energy is self-consistent (SCF) and the electron density is calculated from the wavefunction. The eigenvalue acquired as a result of self consistency gives the description of energy at each molecular orbital.

The Hartree-Fock-Roothan equation (Hartree, 1957) is the most commonly used approximated Schrödinger equation:

[15] $FC = SCE$

where F is the Fock operator whose matrix elements are constituted by one-electron terms and two electron repulsions, S is the overlap matrix, E is the energy, and C is the matrix of coefficients for the atomic orbitals constituting molecular orbitals. An initial

[1] The Hamiltonian of the Schrödinger equation is non-relativistic. It is therefore not appropriate as the velocities of the particles, particularly electrons, approach the velocity of light.

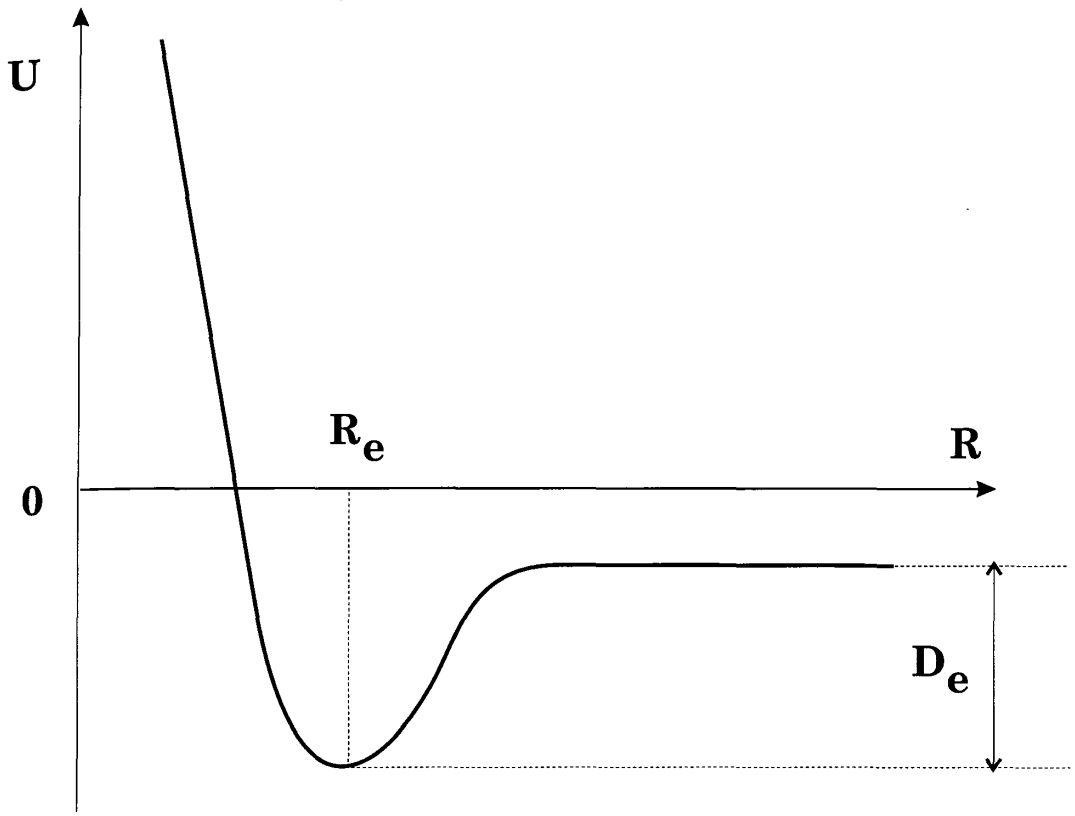

Figure 8. Potential Energy vs. Inter-nuclear Distance
Potential energy of a diatomic molecule at various inter-nuclear distances. This is obtained by solving the Schrödinger equation at every inter-nuclear distance along the vibrational mode of a diatomic molecule; R_e is the equilibrium bond length and D_e is the bond dissociation energy.

guess of these coefficients is used to construct the first Fock matrix and the new coefficients are taken from iterative SCF calculation.

Ab-initio quantum mechanics is the most accurate calculation among many molecular orbital calculations. The accuracy depends on the type of the basis set used. The contracted gaussian type orbital uses the linear combination of gaussian functions to replace the Slater[1] type function. STO-3G is the basis set where three gaussian functions are used. Basis sets are usually described by the number of gaussians per **c**ontracted **g**aussian **t**ype **o**rbital (CGTO), and the number of CGTOs for each atomic orbital in an occupied shell (i.e. 1s, 2s, $2p_x$, $2p_y$, $2p_z$ for all second-row atoms). A "minimal" basis set contains only one basis function per AO (atomic orbital). A double zeta basis set has two CGTO's per AO. The Pople family of basis sets includes the set of STO-*n*G (*n* is the number of gaussian functions) minimal basis sets and a large number of split-valence basis sets which have one basis function for the core orbitals and two or more CGTOs for the valence orbitals. The standard Pople nomenclature is *L-M1M2M3G*, where L is the number of primitive functions in the single core basis function, the number of M_i's indicate how many separate basis functions describe the valence region, and the value of M_i indicates the number of primitive functions in that basis function. For example, in the 6-311G basis set for oxygen, the core 1s orbital is described by the basis function consisting of 6 primitive gaussians. There are three of each of the valence 2s and 2p orbitals, the first containing 3 primitives and the next two consisting of only

[1] Slater-type atomic orbitals (STOs) have exponential radial parts and their convergence is not as good as gaussian functions (Slater, 1930).

one gaussian function each. The polarization of functions on the non-hydrogen atoms is indicated by adding a single "*" to the description, or "**" if the hydrogens have p-type basis functions. Similarly the presence of diffuse functions is indicated by a "+" or "++" before the "G" (e.g. 6-31++G**). Commonly used Pople basis sets and the number of functions for the second row atoms (Li-Ne) are shown in Table 2.

The need for faster calculations for large molecules gave birth to the semi-empirical quantum mechanical methods, where only the outer or valence electrons are taken into account. The decrease of the number of two-electron integrals shows a big improvement in terms of convergence speed. The inner electrons are considered to be less important for chemical phenomena, and are therefore parameterized empirically. The amount of neglect of the diatomic differential overlap integrals is the major discrimination between most semi-empirical methods. The CNDO (Complete Neglect of Differential Overlap) and INDO (Intermediate Neglect of Differential Overlap) methods started an era of development of approximate molecular orbital methods (Pople et al., 1970). The MNDO (Modified Neglect of Diatomic Overlap) method (Dewar et al., 1977), AM1 (Dewar et al., 1985), PM3 (Stewart, 1989; Stewart, 1989), and SAM (Dewar et al., 1993, *23*, 5003) are all semiempirical molecular orbital calculation methods. Detailed theory of these semiempirical methods and the practical use in chemical structure and energy calculation is reviewed by Clark (Clark, 1985).

B. Restricted Hartree-Fock vs. Unrestricted Hartree-Fock

Most molecules have an even number of electrons in their ground (lowest-energy) states and may be represented by closed-shell wavefunctions with orbitals either doubly

Table 2. Commonly Used Pople Basis Sets and the Number of Functions for the Second Row Atoms (Li-Ne).

Basis Set	Number of functions	Basis Set	Number of functions	Basis Set	Number of functions
STO-3G	5	6-31G	9	6-311G	13
3-21G	9	6-31G*	15	6-311G*	18
4-31G	9	6-31+G*	19	6-311+G*	22

The 6-31G* basis set usually include 6d-type polarization functions, others include 5d-functions.

occupied or empty. For open-shell systems, in which electrons are not completely assigned to orbitals in pairs, the Roothaan-Hall equations need modification. This applies to doublet free radicals or triplet states, for which one component will have an excess of α–electrons[1]. For doublets, there will be one extra α-electron, for triplets, two extra α–electrons, and so forth. Simple molecular orbital theory can be extended to open-shell systems in two possible ways. The first is described as spin-restricted Hartree-Fock (RHF) theory. In this approach, a single set of molecular orbitals is used, some being doubly occupied and some being singly occupied with an electron of α spin. This is the case illustrated for a three electron doublet state for lithium (Li) in Figure 9. The spin orbitals used in the single determinant are then $(\psi_1\alpha)$ $(\psi_1\beta)$ $(\psi_2\alpha)$. The molecular orbital expansion coefficients, $c_{\mu i}$ for the **l**inear **c**ombination of the **a**tomic **o**rbitals for the corresponding **m**olecular **o**rbital (LCAO-MO) are still same as those of spin restricted closed shell system:

$$[16] \qquad \psi_i = \sum_{\mu=1}^{N} c_{\mu i}\phi_\mu$$

where ψ_i is an individual molecular orbital and ϕ_μ is a basis function. Their optimum values are still obtained from the variational method:

$$[17] \qquad \frac{\partial E'}{\partial c_{\mu i}} = 0 \quad (\text{all } \mu, i).$$

[1] An electron spin can take only two orientations with respect to a specified axis. An α-electron is one with spin quantum number $m_s = +\frac{1}{2}$ and β-electron is one with $m_s = -\frac{1}{2}$.

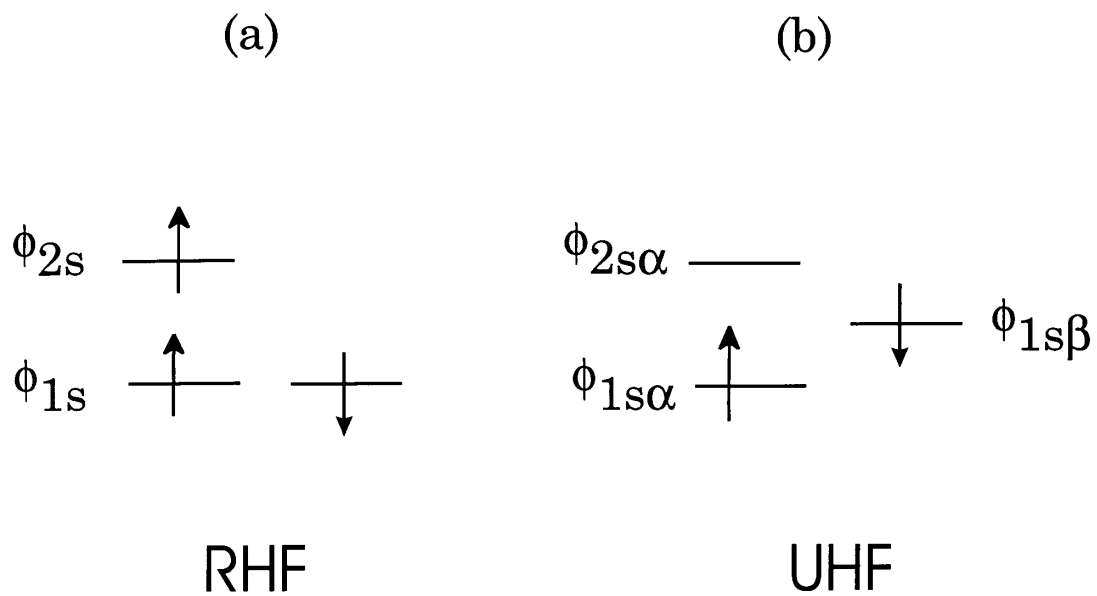

Figure 9. Restricted Hartree-Fock (RHF) vs. Unrestricted Hartree-Fock (UHF). Three electron doublet state for lithium (Li) is used for this example. Notice the different energy levels for the alpha spin (upward arrow) and a beta spin (downward arrow) for the first two electrons in the case of UHF. For the same electrons, alpha and beta spin are treated to be in the same molecular orbital (1s) in RHF calculation.

where E' is the expectation value of the energy and $c_{\mu i}$ is the molecular orbital expansion coefficient. However, details are more complicated since different conditions apply to singly- and doubly-occupied orbitals.

The second type of molecular orbital theory in common use for open-shell systems is spin-unrestricted Hartree-Fock (UHF) theory. In this approach, different spatial orbitals are assigned to α- and β-electrons. Thus, there are two distinct sets of molecular orbitals ψ^{α}_{i} and ψ^{β}_{i} (i=1,..., N). The previously doubly-occupied orbital is now replaced by two distinct orbitals. The wavefunctions for lithium (Li) with both RHF and UHF configuration are given in Figure 9.

C. Atomic Charges

Atomic charge is not a measurable physical property since the electrons are considered a diffuse charge distribution that can arbitrarily be assigned to any atomic center. However, the atomic charge as the net electronic and nuclear charge on each atom is a frequently used term to explain observed chemical behavior.

Mulliken Population Analysis (Mulliken, 1955a; Mulliken, 1955b; Mulliken, 1955c), Natural Population Analysis (NPA), and Molecular Electrostatic Potential (MEP) are among the most frequently used charge partitioning schemes. Mulliken Population Analysis (MPA) assigns the charge to an atomic center on the basis of the total electron density in basis functions located on that center. MPA is known to be basis set dependent and having problems with many modern basis sets (Bachrach, 1994). Natural Population Analysis developed by Reed and co-workers (Reed et al., 1985) divides the electron density matrix into sub-blocks with appropriate symmetry.

The NPA method is much less basis set dependent than the Mulliken Populations method. The Molecular Electrostatic Potential (MEP) method first introduced by Bonaccorsi and co-workers (Bonaccorsi et al., 1972a; Bonaccorsi et al., 1972b) allows chemists to predict reactivity based on atomic charge distribution. (See Chapter V for more detailed explanation of MEP scheme.)

D. Frontier Molecular Orbital Theory

The concept of the Frontier Molecular Orbital Theory is that the overlap between orbitals may favor the reaction between an electron donor and an electron acceptor. In this regard, the Frontier Molecular Orbital Theory is different from electrostatic interactions. In this scheme, a high lying (in energy) occupied orbital (usually the highest occupied molecular orbital; HOMO) in the donor overlaps with a low lying unoccupied orbital (the lowest unoccupied molecular orbital; LUMO) in the acceptor. This feature is shown in schematic diagram in Figure 10. This leads to a net stabilization. Therefore the reactivity of molecules is governed by the energy of these frontier molecular orbitals, HOMO and LUMO. The HOMO is responsible for electrophilic attack and the LUMO is responsible for nucleophilic attack in this way.

The interaction strength is dependent on the energy difference between the two orbitals involved. The smaller energy gap between the orbitals of donor and acceptor, the stronger interaction is expected. The interaction is also governed by the overlap between the orbitals. If the overlap is large between the orbitals of donor and acceptor, there is a larger interaction between them. This explanation scheme can account for the steric effects which diminish the possible overlaps. For the study of the energetics of

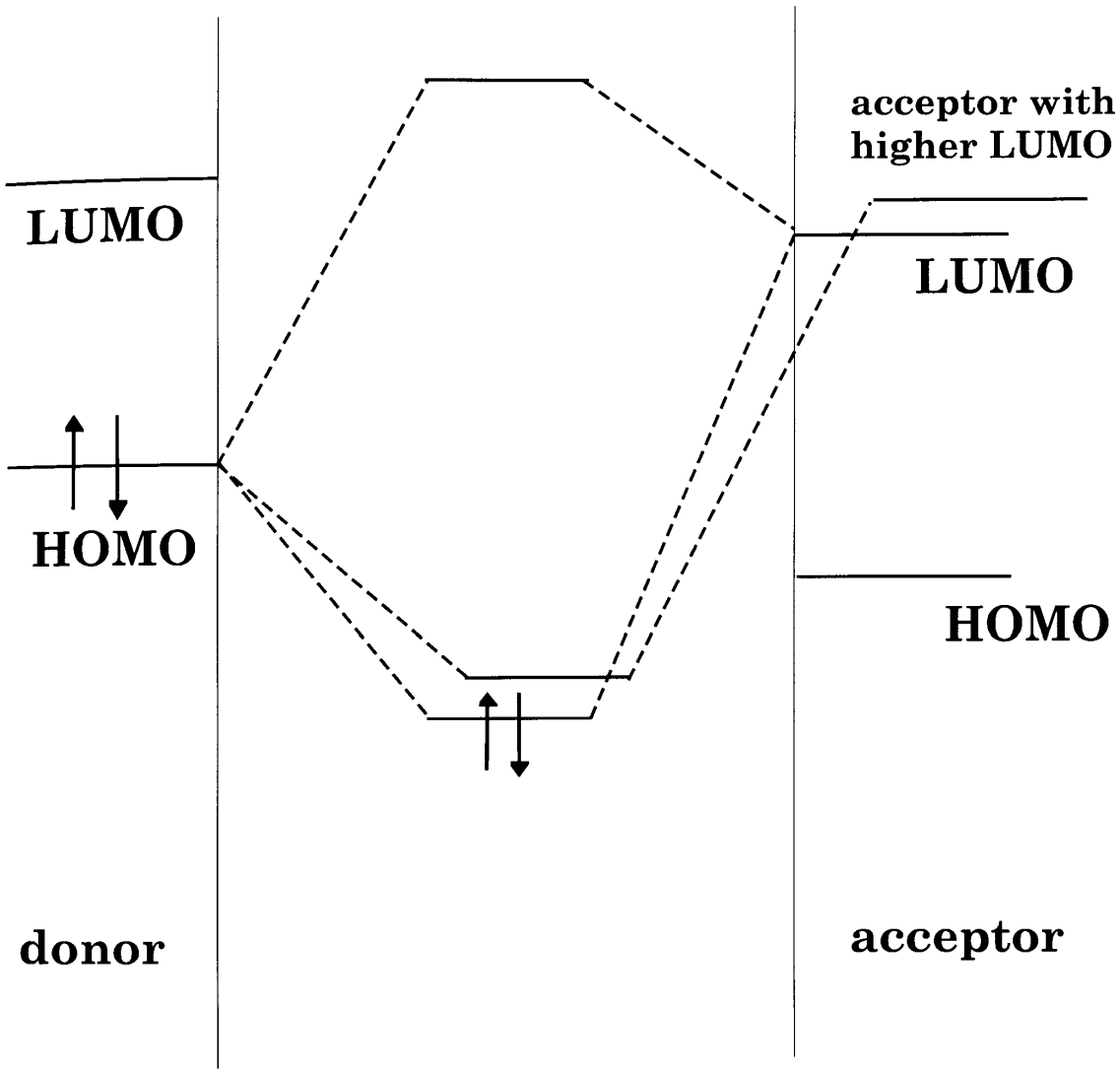

Figure 10. Frontier Molecular Orbital Theory

cytochrome P450 catalysis, the potential for metabolic activation is estimated in terms of the energy difference between the Frontier Molecular Orbitals by Lewis (Lewis, 1992).

Chapter V.

Molecular Mechanics (MM) and Molecular Dynamics (MD)

A. Introduction; Atomic motions in a molecule from one conformation to another

The molecular mechanics approach with its empirical force field can be extended to study in great detail how the atoms of a molecule move as it vibrates and undergoes internal rotation at some thermal energy corresponding to a specified temperature. The idea is as follows. One places the atoms of the molecule in a starting geometry where not all the atoms are in their equilibrium position. Consequently, in the empirical force field, the atoms feel forces and move in response. We ask the program to solve Newton's laws of motion and to move them a tiny distance in the direction they would really go if subject to those forces. This constitutes one small time step. Now the forces are re-calculated and the process repeated. Thus time step by time step we calculate and follow the motion of each atom. For this to work, the time steps must be very small. In practice, each step is often only one femtosecond long. But vibrations take picoseconds, so the simulation must continue for 20 to 100 picoseconds. This type of calculation goes under the general name of Molecular Dynamics.

B. Forcefield, the Basis of the Evaluation of the Interatomic Energy

The results of a molecular mechanics (MM) or molecular dynamics (MD) calculation depend directly on the forcefield. The quality of the forcefield describing the energetics of the system is greatly important. This is because the most important and fundamental part of MM and MD computation is the calculation of the potential energy for a given configuration of atoms. The calculation of this energy, along with its first and second derivatives with respect to the atomic coordinates, yields the information necessary for minimization and dynamics simulations. The forcefield is composed of a functional form of this expression and the parameters needed to fit the potential energy surface (Ermer, 1976; Hagler, 1985).

It is important to understand that the forcefield, both the functional form and the parameters themselves, represents the single largest approximation in molecular modeling. In a MD simulation with no experimental restraints, any results depend critically on the details of the forcefield function and the simulation parameters. If one is refining the forcefield with respect to an extensive NMR data set, then presumably the experimental data are the most important factor determining the final structures.

1. The Energy Expression

Molecular mechanics is based on a classical mechanical picture of a molecule rather than a quantum mechanical one. Neither explicit consideration of electrons nor the quantum mechanic treatment of potential energy is made. (In quantum mechanics the potential energy is represented as a sum of the nuclear repulsion energy and the electronic energy obtained from an approximate solution to the Schrödinger equation).

The potential energy in this classical molecular mechanics (MM) or molecular dynamics (MD) model is written as a superposition of various two-body, three-body, and four body interactions. The potential energy is expressed as a sum of valence or bonded, cross valence, and non-bonded interactions.

[18] $E_{total} = E_{bonded} + E_{cross\text{-}term} + E_{non\text{-}bonded}$

where the valence (bonded) interactions consist of bond stretching (E_R), bond angle bending (E_θ), dihedral angle torsion (E_ϕ), and inversion terms(E_ω). The non-bonded interactions consist of van der Waals (E_{vdw}) terms and electrostatic (E_{el}) terms. The valence cross-term set generally consists of bond-angle and angle-angle terms. Cross terms are used to improve the accuracy of modeling mechanical properties. The pictorial representations of these individual energy terms are shown in Figure 11.

During the last decade, several forcefields have been developed. AMBER, CHARMm, DREIDING, and Universal Force Field (UFF) are some of these. AMBER and CHARMm have been used most widely, especially in the biological or biochemical field. A recent development is Universal Force Field by Rappé and co-workers. This excellent, general purpose force field that has been parameterized for the full periodic table. The form of the expression of the potential energy in UFF is given by following equation:

[19] $E = E_R + E_\theta + E_\phi + E_\omega + E_{vdw} + E_{el}$

where the name of each potential energy term at the right hand side of the equation is already explained above.

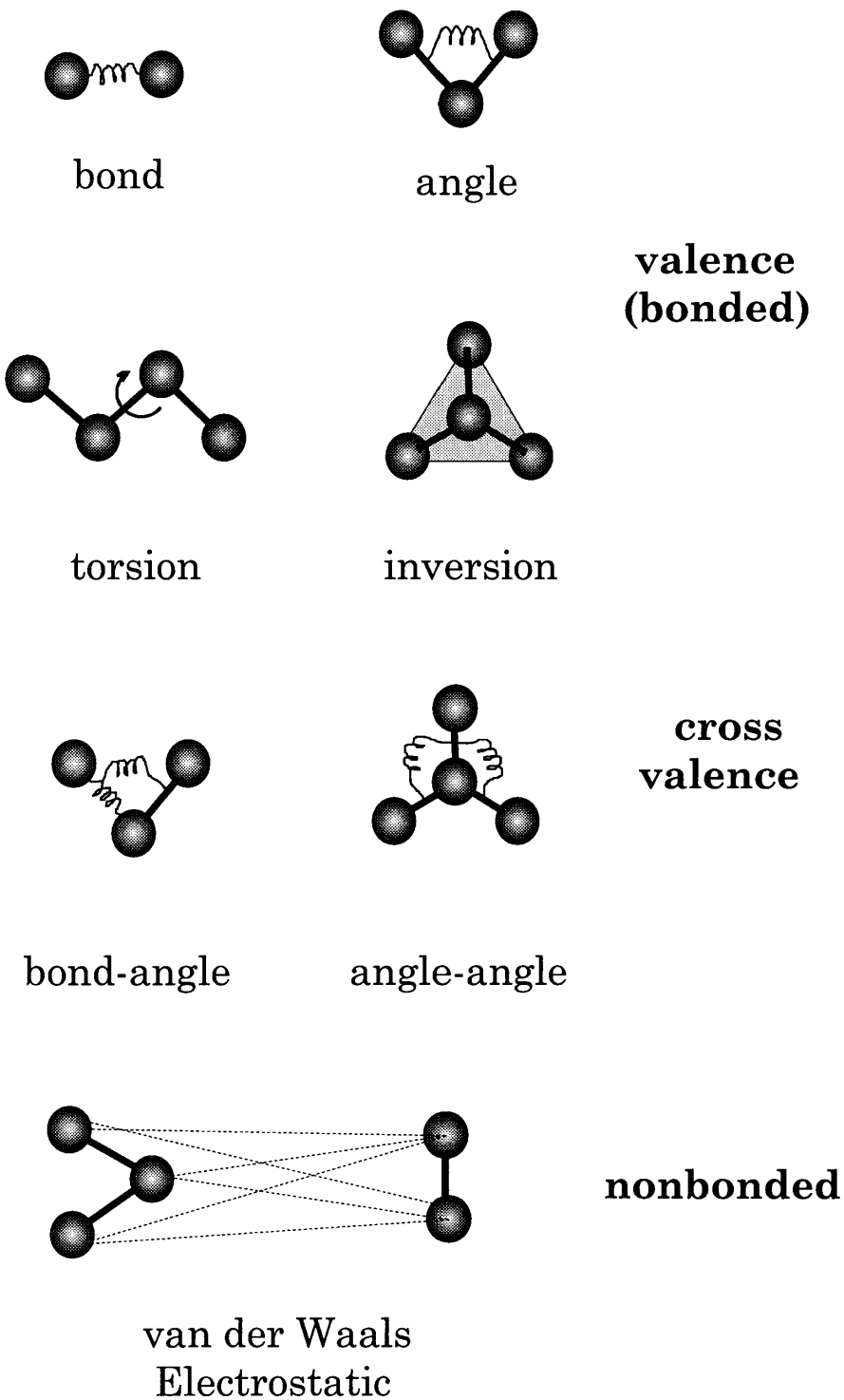

Figure 11. Pictorial Representation of Energy Terms Used in Forcefield Calculations (dotted line denotes the interactions between nonbonded atoms).

2. Bond Stretch

The bond stretch of UFF is described as a harmonic oscillator :

[20] $E_R = \frac{1}{2} k_{IJ} (r-r_{IJ})^2$

or as the Morse function:

[21] $E_R = D_{IJ}\left[e^{-\alpha(r-r_{IJ})}\right]^2$

where k_{IJ} is the force constant in units of (kcal/mole)/Å, r_{IJ} is the standard or natural bond length in Angstroms, D_{IJ} is the bond dissociation energy (kcal/mol), and the exponential factor α is given by:

[22] $\alpha = \left[\frac{k_{IJ}}{2D_{IJ}}\right]^{1/2}$

The Morse function is known to be more accurate due to its implicit inclusion of anharmonic terms near equilibrium (r_{IJ}). The Morse potential goes to a finite energy ($E_b = D_o$) for $R = \infty$ and should be used for systems where a covalent bond is allowed to break. The forces with the Morse term go to 0 as $R \rightarrow \infty$. Consequently, this is not a good form to use when sketching molecules or otherwise starting from a poor geometry. The natural bond length r_{IJ} is assumed to be the sum of single bond radii which is specific to the atom type, bond order correction, and an electronegativity correction:

[23] $r_{IJ} = r_I + r_J + r_{BO} + r_{EN}$

The bond radii, r_I or r_J, were obtained from experimental bond distances which includes X-ray structures obtained from Cambridge Database (see reference for Kennard, O.,

Cambridge Crystallographic Data Centre). The bond order correction, r_{BO}, is a Pauling type (Pauling, 1960) used to modify the single bond radii:

[24] $r_{BO} = -\lambda (r_I + r_J) \ln(n)$

where the proportionality constant $\lambda = 0.1332$ Å was determined for propane, propene, and propyne. The term n is for the bond order, where r_{BO} would be zero for the bond order $n = 1$. Here, the structural-electronic effects such as resonance, metal-ligand π bonding, metal-ligand π back bonding, and the *trans* influence are considered to predict the molecular structure. The electronegativity correction, r_{EN}, is used according to the suggestion by O'Keeffe and Brese (O'Keeffe et al., 1991) in the form of :

[25] $$r_{EN} = \frac{r_I r_J \left(\sqrt{\chi_I} - \sqrt{\chi_J}\right)^2}{\left(\chi_I r_I + \chi_J r_J\right)}$$

where χ_I and χ_J are GMP (**G**eneralized **M**ulliken-**P**auling) electronegativity (Rappé et al., submitted).

3. Angular Bendings

The Universal Force Field uses a three-term Fourier expansion to describe all angular distortions:

[26] $$E_a = K_\theta (C_o + C_1 \cos\theta + C_2 \cos 2\theta)$$

where the coefficients are:

[27] $$C_o = C_2 (2\cos^2 \theta_o + 1)$$

[28] $$C_1 = -4C_2 \cos\theta_o$$

[29] $$C_2 = \frac{1}{4\sin^2\theta_o}$$

where K_θ is the Fourier expansion parameter and θ_o is the bond angle for given any two bonds to a common atom. As shown above, the only inputs are K_θ and θ_o.

4. Dihedral Angle Torsions

The formula expression regarding dihedral angular torsion is rather complicated without definition of torsional angle along with a descriptive picture. The picture showing the dihedral angle is given in Figure 12. If two bonds IJ and KL are attached to a common bond JK, then the dihedral angle ϕ is defined as the angle between the JKL plane and the IJK plane as shown in Figure 12. Looking from J toward K, clockwise orientation as shown is considered to be positive. The *trans* configuration is when dihedral angle ϕ is zero and the *cis* configuration is when ϕ is 180°. The torsional energy is then given by:

[30] $$E = \sum j \frac{1}{2} B_j [1 - d_j \cos(n_j \phi)]$$

where ϕ is the angle between the JKL plane and the IJK plane, n is the periodicity of the potential (n=1,2,3,4,5,6), and d is the phase factor ($d = \pm 1$).

5. Inversions

For UFF, a one or two term cosine Fourier expansion in w is used for atoms I bonded exactly to three other atoms J, K, L:

[31] $$E_\omega = K_{IJKL}(C_o + C_1 \cos\omega_{IJKL} + C_2 \cos 2\omega_{IJKL})$$

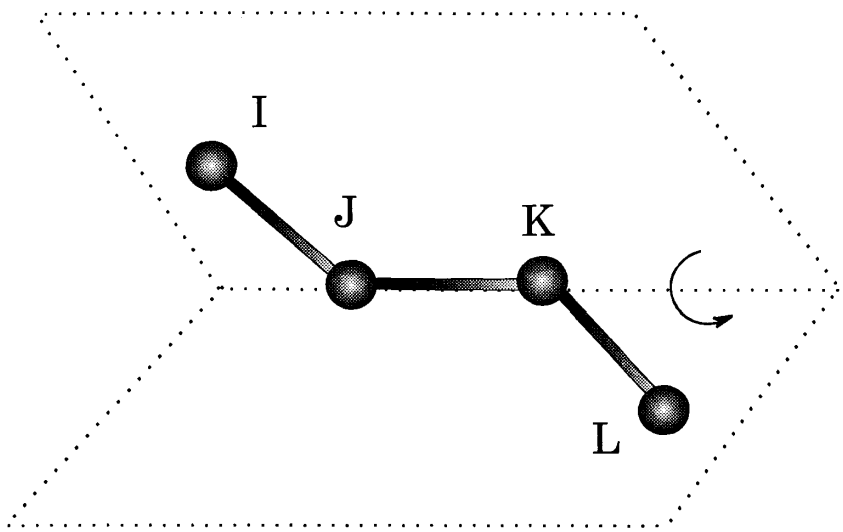

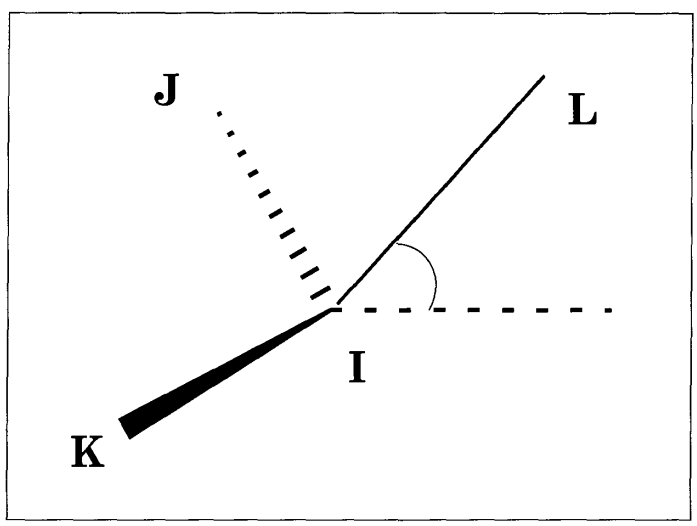

Figure 12. Angles for Torsions and Inversions.
(a) dihedral angle for torsion; the angle that IJ and KL makes when looking down JK bond.
(b) angle between IL and IJK (plane) for inversional term.

where K_{IJKL} is the force constant in (kcal/mole) and ω_{IJKL} is the angle between the IL axis and the IJK plane (See Figure 12).

6. van der Waals

Non-bonded interaction terms in UFF can be one of two different types. A Lennard-Jones 6-12 potential is:

$$[32] \quad E_{vdw}(R) = D_{IJ}\left\{-2\left[\frac{R_{IJ}}{R}\right]^{6} + \left[\frac{R_{IJ}}{R}\right]^{12}\right\}$$

where the input of inter-atomic distance R is given in terms of van der Waals bond length R_{IJ} (in Å) and bond strength D_{IJ} (in kcal/mole). The exponential-6 form is given by the equation,

$$[33] \quad E_{vdw}(R) = Ae^{-CR} - BR^{-6} = D_o\left\{\left[\left(\frac{6}{\gamma-6}\right)\exp^{\gamma\left(1-\frac{R}{R_{IJ}}\right)}\right]\right\} - \left[\left(\frac{\gamma}{\gamma-6}\right)\left(\frac{R_{IJ}}{R}\right)^{6}\right]$$

where A is pre-exponential term, B is dispersive attractive term, C is repulsive exponential, R is interatomic distance, D_o is bond strength (well depth) in kcal/mole, R_{IJ} is bond length in Å, and γ is the scaling factor. The 6-12 Lennard-Jones form is better performing than exponential-6 form in terms of its numerical stability. The exponential-6 form blows up for small internuclear separations.

7. Off-diagonal VDW

UFF assumes standard geometric combination rules for the van der Waals potential between hetero atoms (off-diagonal VDW) using diagonal values (between the same atoms):

[34] $$D_{IJ} = \sqrt{D_{II} \cdot D_{JJ}}$$

[35] $$R_{IJ} = \sqrt{R_{II} \cdot R_{JJ}}$$

where D_{II}, D_{JJ}, R_{II}, and R_{JJ} and are the diagonal VDW term for energy and bond length while D_{IJ} and R_{IJ} are pertaining to off-diagonal VDW.

An alternative way of doing combination rule on these off-diagonal VDW's is the simple arithmetic mean:

[36] $$R_{IJ} = \frac{1}{2}\left(R_{II} + R_{JJ}\right)$$

where R_{IJ} is the Lennard-Jones distance for off-diagonal atoms and R_{II} and R_{JJ} are those for diagonal atoms.

While the CHARMm and Dreiding-I force fields use arithmetic mean as a default, AMBER, Dreiding-II, and UFF uses geometric combination rule by default. In general, the geometric rule for the combination rule describes the summation of van der Waals terms for crystalline system better than arithmetic rule.

8. Electrostatic Interactions (Coulombic Interactions)

Electrostatic interaction plays a very important role in the study of drug-receptor interactions and structure of inorganic systems. The study of interaction energy in our clay-intercalated chemical complex system is also greatly dependent on the electrostatic interactions. The total electrostatic energy is written as:

[37] $$E_{coul} = C_o \sum_i \sum_{j>i} \frac{Q_i Q_j}{\varepsilon R_{ij}}$$

where Q_i, Q_j are the charges in electron units (e), R_{ij} is the distance between off-diagonal (hetero) atoms in Å, ε is the dielectric constant (ε=1 used for a vacuum), and C_o is a conversion factor (=332.0637) which accounts for the unit of E_{coul} in kcal/mol.

For a molecule having N atom components, there are N(N-1)/2 Coulombic interactions. The study of clay lattice in our unit cell in this study (320 atoms) with hexaaminеruthenium(3+) complex (25 atoms) has 59,340 non-bond interactions to evaluate. We should be able to cut down this number of non-bonded interactions to save our computation time. However, a difficulty arising from this approximation approach is that the Coulombic potential is relatively very long range and it is significant even at a distance of 100Å. For non-periodic systems, we use a cutoff distance to include only the most effective charges. For periodic systems, one of the most well known approaches is to use an Ewald summation scheme. Discussion of Ewald summation will be found in the later part of this chapter.

9. Non-bonded VDW and Electrostatic Energy Exclusion (Valence Exclusion)

Most force fields define non-bonded interactions including van der Waals and electrostatic energy terms so as to exclude the components between atoms that are already considered under previous valence (bonded) terms (this is rather expensive step in terms of computation time even though most of computational package performing this step). Commonly excluded non-bonded terms throughout the force fields are those called 1-2 interaction (between atoms that are bonded together) for van der Waals interactions and 1-3 interactions (between atoms that are bonded to a common atom) for electrostatic and VDW interactions. For the 1-4 interaction (between atoms that are

considered as the terminal dihedral torsional opponents), the exclusion fashion is different depending on the type of the force field used. Some force fields also exclude the non-bonded terms between atoms in 1-4 interaction. A force field like AMBER usually uses half scaled values of this 1-4 non-bonded interaction for van der Waals and coulombic interactions while UFF only excludes 1-2, and 1-3 interaction by default. The pictorial representation of these 1-2, 1-3, and 1-4 interactions is found in Figure 13.

C. Energy Minimization

Because the concept of structure is central to chemistry, finding the energy minima of complex, multidimensional surfaces itself has been one of the most extensively studied fields. By simply minimizing energy, stable conformations can be identified. This is known as a classical treatment of the molecular geometry. In the real (quantum mechanical) world, molecules are never at rest and molecular structure is a dynamical concept involving oscillations of the nuclear positions about equilibrium geometries (Bartett et al., 1994).

Minimization of a molecule is done in two steps. First, an equation describing the energy of the system as a function of its coordinates must be defined and evaluated for a given conformation. Target functions may be constructed that include external restraining terms to bias the minimization, in addition to the energy terms. Next, the conformation is adjusted to lower the value of the target function. A minimum may be found after one adjustment or may require many thousands of iterations, depending on the nature of the algorithm, the form of the target function, and the size of the molecule. The efficiency of the minimization is therefore judged by both the time needed to

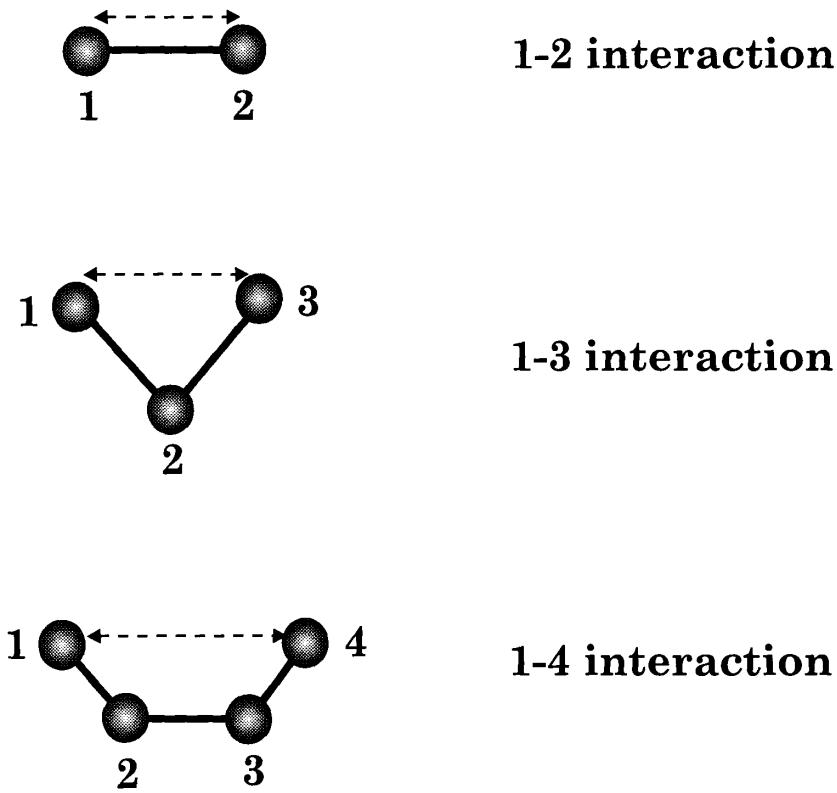

Figure 13. Nonbonded Exclusion Terms

evaluate the target function and the number of structural adjustments (iterations) needed to converge on the minimum.

The potential energy calculated by summing the energies of various interactions is a numerical value for a single conformation. This number can be used to evaluate a particular conformation, but it may not be a useful measure of a conformation because it can be dominated by a few bad interactions. For instance, a large molecule with an excellent conformation for nearly all atoms can have a large overall energy because of a single bad interaction, for instance two atoms too near each other in space and have a huge van der Waals repulsion energy. It is often preferable to carry out energy minimization on a conformation to find the best nearby conformation. Energy minimization is usually performed by gradient optimization: atoms are moved so as to reduce the net forces on them. The minimized structure has small forces on each atom and therefore serves as an excellent starting point for molecular dynamics simulations.

The conjugate gradient algorithm (Fletcher et al., 1964) was used for this study. There are other methods available to find a global minimum conformation (see Figure 14 for the types of minima) of a molecule such as the steepest descent (Levitt, 1969), Newton-Raphson methods (a quadratically-convergent method for finding a root of an equation, and its variants), and quasi Newton-Raphson method. Detailed treatments of Newton methods can be found in the literature (Fletcher, 1987; Gill et al., 1983; Dennis et al., 1983).

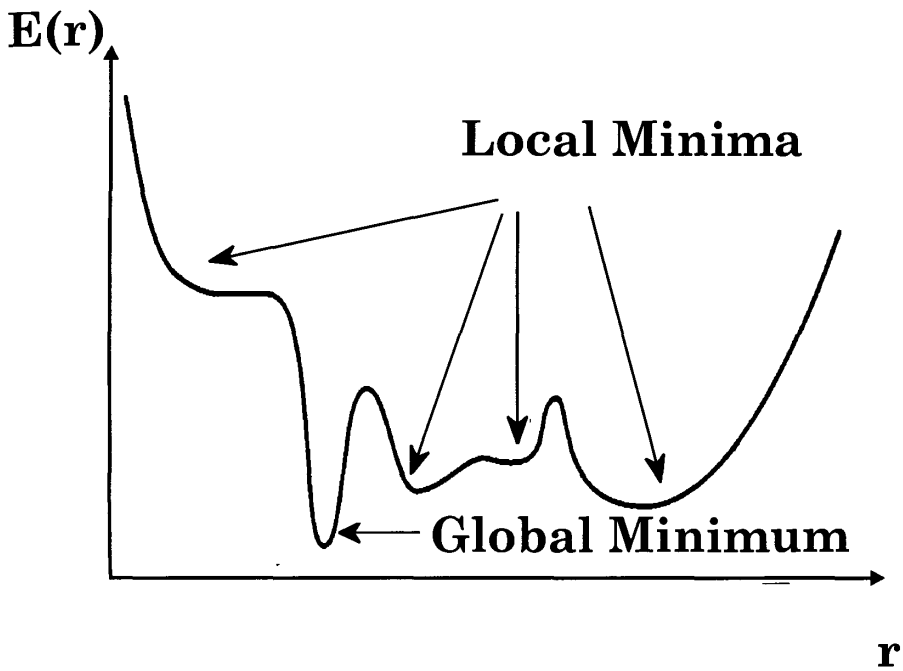

Figure 14. Local and Global Minima

1. Steepest Descent (SD)

Steepest descent is one of the oldest and simplest methods. In general, SD converges rapidly near the initial conformation but slowly near the minimum. This is why it is often used to clear bad contacts in the initial stage of minimization. At each iteration, coordinates are displaced in a direction opposite to the gradient of the potential energy. At each iteration of SD, the search direction is taken as $-g_k$, the negative gradient of the objective function at x_k. The new line search is always perpendicular to the previous gradient. This is especially inefficient where the energy surfaces have narrow valleys. A more detailed discussion of SD is found elsewhere (Dennis Jr. et al., 1983).

2. Conjugated Gradient (CG)

The deficiency of refining the direction of the minimization direction in SD is improved in the conjugated gradient method. CG algorithm makes use of previous minimization steps as well as the current gradient to determine the next step. The convergence rate of this conjugated method is very rapid. Convergence can be quadratic, rather than linear as for SD, and is especially improved near the minimum. In CG, h_{i+1}, the new direction vector leading from point i+1, is computed by adding the gradient at point i+1, g_{i+1}, to the previous direction h_i scaled by a constant γ_i:

[38] $$h_{i+1} = g_{i+1} + \gamma_i h_i$$

where γ_i is a scalar defined by Fletcher and Reeves (Fletcher et al., 1964) as following equation:

[39] $$\gamma_i = \frac{(g_{i+1} - g_i)g_{i+1}}{g_i g_i}$$

CG is the good choice for minimization of large systems. It requires only previous 3N (N is the number of atoms in the system) gradients and directions for storage to determine next iteration while Newton-Raphson scheme needs a relatively big storage for the second-derivative matrix (N(N+1)/2). This efficiency and the ensured mutually conjugate directions are also accomplished by more complete line search minimization.

D. Long Range Corrections of Non-bonded Interactions

The treatment of long range non-bonded interactions is important especially in the case that we have many atoms in a widely spread lattice or 3 dimensional glob such as big protein molecule. The computational cost of calculating every non-bonded (VDW and electrostatic) interaction is very high in terms of time. The system which has 350 atoms inside exceeds 60,000 interaction pairs. I also mentioned that some kind of approximation scheme is necessary to cut down the huge number of non-bonded interaction pairs which both MM and MD algorithm have to go through at every step for their own energy calculation. Therefore the accuracy of the results in MM and MD will greatly depend on the quality of approximation used.

If one uses cutoff distances for the minimization or dynamics for a system, one may acquire undesired border artifacts in which the energy jumps abnormally at the border when an atom moves in and out of this cutoff range. Inclusion and the exclusion

of the non-bonded energy term with respect to the cutoff distance is no longer valid. The direct method with fixed cutoff distance is also very slow for large cutoff distances.

An improvement can be made to reduce the large jump of the direct method with the cutoff distance. In this method, called the spline switching method, the energy is multiplied by a spline function. Instead of fixed single cutoff, two different parameters called spline-on and spline-off distances are used to define the cutoff. Within the spline-on/spline-off range, the non-bonded interaction energy is reduced according to the spline function while it is ignored beyond the spline-off distance. The narrower the spline-on/spline-off range, the faster the interaction energy converges. One may want to extend the spline-on/spline-off range to increase the accuracy of the computation. However the computational time, at the same time, will increase dramatically.

Ewald summation is one of the procedures developed to solve the problems mentioned above. While VDW has rapid potential drop across certain interatomic distances due to its 6-12 exponential function, the electrostatic interaction's convergence over the interatomic distance variation is very slow due to its 1/r dependency. The use of a two step summation (one in real space and one in reciprocal space) for the periodic system will give a more accurate value for the electrostatic interactions (Ewald, 1921). One summation is carried out in reciprocal space while the other is carried out in real space. Based on Ewald's formulation, the simple lattice sum can be reformulated to give absolutely convergent summations which define the principal value of the electrostatic potential, called the intrinsic potential. Given the periodicity present in both crystal calculations and in dynamics simulations using

periodic boundary conditions, the Ewald formulation becomes well suited for the calculation of the electrostatic energy and force. It was originally developed for the study of ionic crystals. In Figure 15, hydrogen $H1_A$ of the cobalt trisbipyridine trivalent cation interacts with hydrogens, $H2_A$, $H2_B$, $H2_C$, $H2_D$, and all other mirror images of hydrogen $H2_A$. These hydrogens are shown in darkened circles. Potential energy can be written as:

$$[40] \qquad E_{el} = \frac{1}{2}\sum_{\mathbf{n}}{}' \left(\sum_{i=1}^{N}\sum_{j=1}^{N} \frac{q_i q_j}{|r_{ij} + n|} \right)$$

where q_i, q_j, are the charges. The conversion factor of $4\pi\varepsilon_o$ is omitted for simplicity and this corresponds to adopting a non-SI unit of charge. The sum over $\boldsymbol{n}$ is the sum over all simple cubic lattice points, $\boldsymbol{n} = (n_xL, n_yL, N_zL; n_x, n_y, n_z$ are integers and L is the length of the unit lattice). This vector represents the shape of the unit cell. The prime after the summation sign indicates that we should omit the potential term when i = j for $\boldsymbol{n} = 0$. This conditionally convergent long range potential sum is then converted into a two term convergence unit of real space and reciprocal space as stated earlier. This two term convergence equation is a result of multiplying a function to the equation just shown, the so-called convergence function. The convergence function for the electrostatic energy and the dispersive energy was used by Karasawa and co-workers (Karasawa et al., 1989).

The Ewald method is significantly more accurate than the atom-based calculation with a large cutoff. Ewald processing time grows as $N^{1.5}$, where N is the

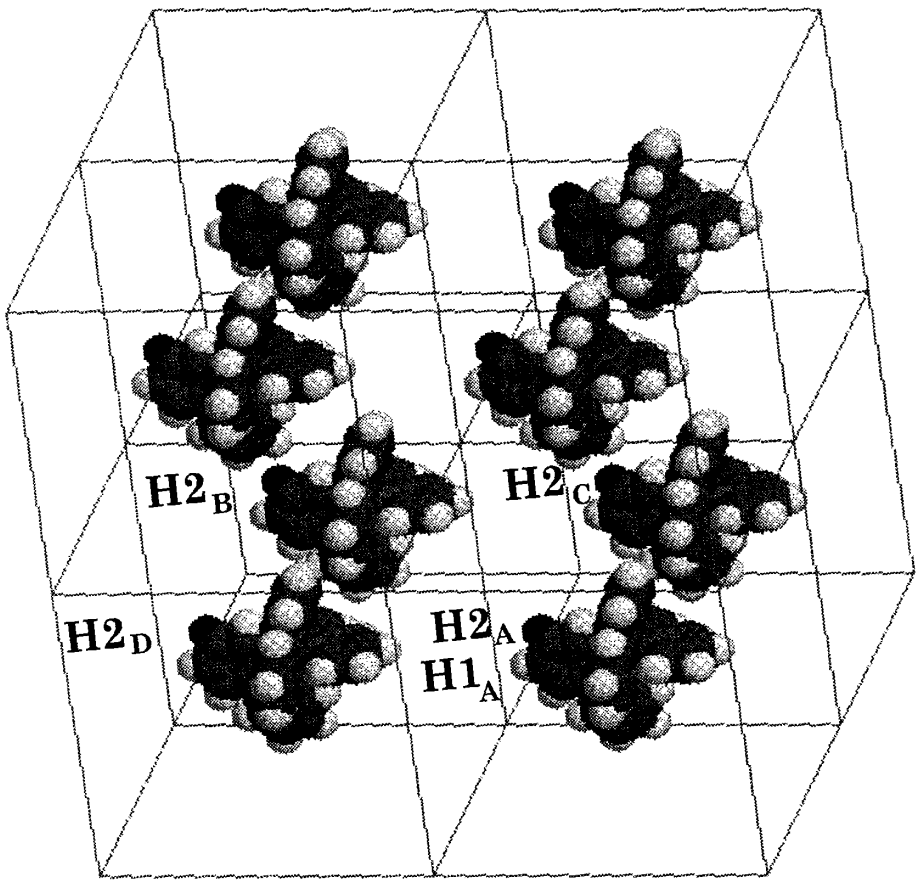

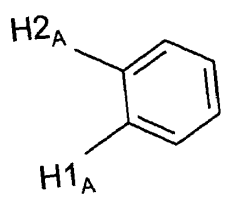

Figure 15. Ewald Summation

number of atoms in the unit cell. The estimation of the cutoff and convergence constants for Ewald method, however, is more difficult. The automation of parameter choice has been used with the inputs of accuracy and a time ratio (Karasawa et al., 1989). The value chosen for the time ratio does not affect the accuracy of the calculation, only the time taken to perform it.

The method called 'minimum image convention' is also used for limiting the non-bonded interactions to those within the unit cell. A two dimensional representation of the minimum image convention is shown in Figure 16. For the atom 1_A in the cell A, only interactions within the volume of the unit cell centered on the atom 1_A are considered. The cutoff (equal to the circle radius) must be less than half the shortest perpendicular distance between the faces of the cell. For a 3-D cubic system the maximum cutoff is half the unit cell length. This method was first used in the famous Monte Carlo simulation by Metropolis and co-workers (Metropolis et al., 1953).

E. Obtaining Atomic Charges

Atomic charge is the parameter which is responsible for the non-bonded electrostatic energy involved in a molecular mechanics and dynamics calculation. Even though atomic charge information is necessary to achieve this interatomic interaction potential calculation, there is no unique way to obtain it from experiment or calculation. From the quantum mechanical point of view, a molecule is composed of nuclei and electrons. Each nucleus bears positive charge equal to its own atomic number while each electron bears a charge of -1e. While the point charge treatment of nuclei is reasonable considering their relative stationary state compared to electrons, the

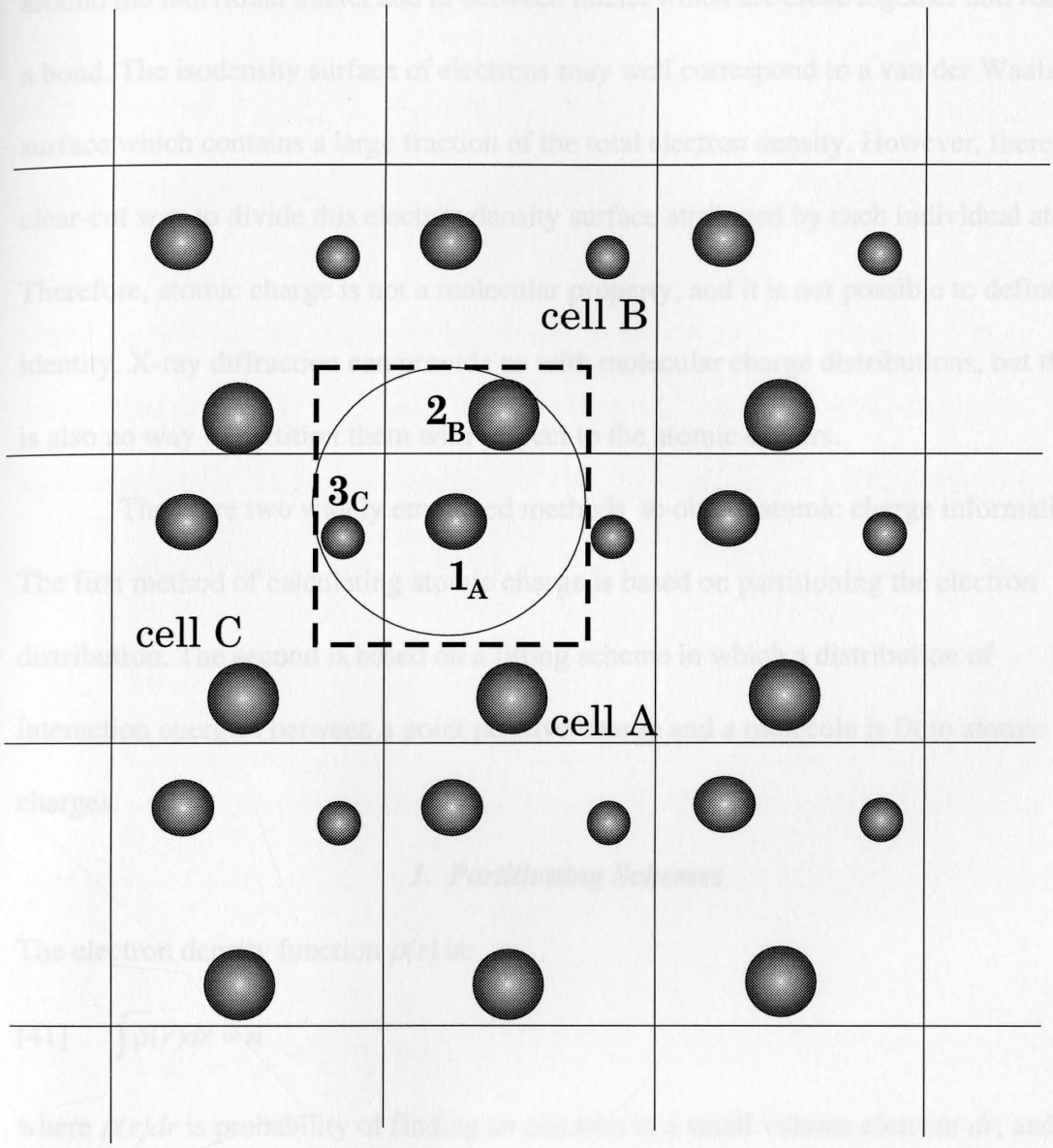

Figure 16. Minimum Image Convention

treatment of electrons should be more detailed. It is probable to find electrons both around the individual nuclei and in between nuclei which are close together and forming a bond. The isodensity surface of electrons may well correspond to a van der Waals surface which contains a large fraction of the total electron density. However, there is no clear-cut way to divide this electron density surface attributed by each individual atom. Therefore, atomic charge is not a molecular property, and it is not possible to define its identity. X-ray diffraction can provide us with molecular charge distributions, but there is also no way to partition them with respect to the atomic centers.

There are two widely employed methods to obtain atomic charge information. The first method of calculating atomic charge is based on partitioning the electron distribution. The second is based on a fitting scheme in which a distribution of interaction energies between a point positive charge and a molecule is fit to atomic charges.

1. Partitioning Schemes

The electron density function $\rho(r)$ is:

[41] $$\int \rho(r)dr = n$$

where $\rho(r)dr$ is probability of finding an electron in a small volume element dr, and n is the total number of electrons when the integration is carried out over all space. In Hartree-Fock theory,

[42] $$\rho(r) = \sum_{\mu}^{N}\sum_{\nu}^{N} P_{\mu\nu}\phi_{\mu}\phi_{\nu}$$

where $P_{\mu\nu}$ is an element of the density matrix (μ by ν), and the summations are carried out over all atom-centered basis functions, ϕ_μ and ϕ_ν. This leads to:

$$[43] \quad \int \rho(r) dr = \sum_{\mu}^{N} \sum_{\nu}^{N} P_{\mu\nu} \int \phi_\mu \phi_\nu d\tau$$

$$= \sum_{\mu}^{N} \sum_{\nu}^{N} P_{\mu\nu} S_{\mu\nu} = n$$

where $S_{\mu\nu}$ are elements of the overlap matrix. Similar types of expressions may be constructed for density functional, correlated models, and other semi-empirical molecular orbital calculations. Notice that overlap matrix, $S_{\mu\nu}$ is a δ function whose value equals 1 if $\mu=\nu$ ($\phi_\mu = \phi_\nu$; $S_{\mu\nu} = \int \phi_\mu \phi_\nu d\tau = 1$) and 0 if $\mu \neq \nu$. It is also important that the total number of electrons in a molecule is now expressed as a sum of products of density matrix and overlap matrix elements.

In the Mulliken procedure (Mulliken, 1955), the above summation over pairs of atomic basis functions is divided into two parts: diagonal ($\mu=\nu$; $S_{\mu\nu}=1$) and off-diagonal ($\mu \neq \nu$).

$$[44] \quad \sum_{\mu}^{N} \sum_{\nu}^{N} P_{\mu\nu} S_{\mu\nu} = \sum_{\mu}^{N} P_{\mu\mu} + 2 \sum \sum_{\mu<\nu}^{N} P_{\mu\nu} S_{\mu\nu} = n$$

The second part of the right hand side of the equation describes the off-diagonal element of density matrix multiplied by overlap matrix. This only describes the case when ϕ_μ and ϕ_ν reside on the same atom. When ϕ_μ and ϕ_ν reside on different atoms, Mulliken's simplistic assumption, giving each of the two centers half of the total overlap, fails.

Within the Mulliken charge scheme, a gross population, q_μ, for basis function ϕ_μ can be defined as:

[45] $$q_\mu = P_{\mu\mu} + \sum_{\mu \neq \nu} P_{\mu\nu} S_{\mu\nu}$$

Atomic populations, q_A, and atomic charges, Q_A, are:

[46] $$q_a = \sum_{\mu}^{onA} q_\mu \quad \text{and} \quad Q_A = Z_A - q_A$$

where Z_A is the atomic number of atom A.

2. Fitting Schemes

The most widely used fitting scheme, the method used for the minimization and dynamics simulation in this study, is that based on the molecular electrostatic potential, ε_p (Chirlian et al., 1987; Breneman et al., 1990). Molecular Electrostatic Potential (MEP) used represents the energy of interaction between a point (positive) charge and the nuclei and electrons of a molecule. For a point positive charge located at p, the molecular electrostatic potential, ε_p is given by the equation:

[47] $$\varepsilon_p = \sum_{A}^{nuclei} \frac{Z_A}{R_{Ap}} + \sum_{\mu}^{N} \sum_{\nu}^{N} P_{\mu\nu} \int \frac{\phi_\mu^*(1)\phi_\nu(1)}{r_{1p}} dx_1 dy_1 dz_1$$

where the first summation is over the nuclei A with charges (atomic numbers) Z_A and separated from p by distances R_{Ap}, and the second (double) summation is over the entire set of N atomic basis functions ϕ; $P_{\mu\nu}$ are elements of the one electron density matrix, which may be derived either from a Hartree-Fock wavefunction, and the integrals involve the operator $1/r_{1p}$, the separation between electron 1 and the test charge p. The

uses of MEP for the charge calculation for the Lattice Minimization and Molecular Dynamics simulation are found elsewhere (Breu et al., 1995, *34*, 4504-4510; Sato et al., 1992).

So far I compared two different methods to compute the atomic charge. The demand to acquire the atomic charge data is due to increased use in empirical molecular mechanics and molecular dynamics calculations. Hartree-Fock models with MEP fitting is widely used and the utilization of density functional (Broclawlk et al., 1996; Holthausen et al., 1996; Li et al., 1995) or MP2 correlated models in place of Hartree-Fock models are also found (Yamanaka et al., 1994).

Chapter VI.

Methods

A. Diffusion of Intercalated Cationic Compounds, $Ru(NH_3)_6^{3+}$, $Co(en)_3^{3+}$, $Co(NH_3)_6^{3+}$, $Co(sep)^{3+}$, and $Co(bpy)_3^{3+}$ in montmorillonite

1. Materials and Methods Used for Experiments

a. Chemicals

Standard Wyoming sodium montmorillonite (SWy-1) was obtained from the Source Clay Repository (University of Missouri, Columbia, MO) and purified (Stein et al., 1995). Cobalt(III) sepulchrate trichloride [Co(sep)Cl_3] (Aldrich), Ruthenium(III) hexamine trichloride [$Ru(NH_3)_6Cl_3$] and Tris(ethylenediamine)cobalt(III) chloride dihydrate [$Co(en)_3Cl_3 \cdot 2H_2O$] (Alfa-Aesar), and Cobalt(III) hexamine trichloride [$Co(NH_3)_6Cl_3$] (Johnson Matthey) were used as received. Tris(2,2′-bipyridine) cobalt(II)perchlorate dihydrate $Co(bpy)_3(ClO_4)_2 \cdot 2H_2O$ previously synthesized in our group as described (Fitch et al., 1993) was used.

b. Electrochemical Measurements

Electrodes were polished using 0.05 mm alumina and copious amounts of water. The electrodes were then rinsed and sonicated to remove any remaining alumina at the surface of the electrode. This procedure was performed prior to the coating of clay for

surface of the electrode. This procedure was performed prior to the coating of clay for the CME (clay-modified electrode) and prior to the beginning of any cyclic voltammetric run for the bare electrode. SPCMEs (spin-coated clay-modified electrodes) were prepared by applying 1μL of a 35 g/L clay solution to the electrode. The electrode was inserted into an inverted Pine MSR electrode rotator and spun at 800 rpm for 20 minutes. Electrodes were visually inspected for cracks under the microscope. Those with cracks were discarded and a new clay film was coated. Acceptable films were allowed to pre-swell for five minutes in the N_2-purged electrolyte and then switched to the same electrolyte containing the electroactive probe molecule. An SCE (Saturated Calomel Electrode) and a Pt wire were used as reference and counter electrodes, respectively.

Cyclic Voltammetric (CV) measurements for $Co(sep)^{3+}$, $Ru(NH_3)_6^{3+}$, $Co(en)_3^{3+}$, $Co(NH_3)_6^{3+}$, and $Co(bpy)_3^{3+}$ were carried out in a standard three electrode configuration with an AgCl/Ag used as a reference electrode. The original measurements, except $Co(bpy)_3^{3+}$ were accomplished previously in our group (Fitch et al., 1996) and the same experiments have been repeated for confirmation. A PAR 175 universal programmer and PAR 173 potentiostat (E.G.&G) were used with data collected to a Gateway 486 using Cio-DAS 08 A/D converter (Computer Boards, Inc., MA) and Snap-Master Data acquisition software (HEM Data Corp, MI) for data collection. Multiple sweep cyclic voltammograms were obtained at a concentration of 1mM probe and 0.1 M NaCl and a sweep rate of 50 mV/s between the potentials of 0.4V and -0.8V for $Co(en)_3^{3+}$.

2. *Computational Methods*

a. The Clay Model.

The clay montmorillonite that we have studied is based on natural Wyoming montmorillonites. The ideal formula for this type of dioctahedral smectite clay when there is no metal atom substitution is $Al_4\ Si_8O_{20}(OH)_4$. We used a well known ideal isomorphic substituted formula for the clay montmorillonite (Sposito, 1989):

[48] $[Si_{7.75}Al_{0.25}][Al_{3.5}Mg_{0.5}]O_{20}(OH)_4$

Our simulation unit cell contains 8 (4x2x1, xyz) unit cells for montmorillonite clay, obtained from X-ray data (Maegdefrau et al., 1937). A slab size of 21.12Å by 18.28Å by 6.56Å of clay was used (Figure 17). Our 4x2 model bears a negative charge of 6 electrons (2 electrons from substituted Al in the tetrahedral position of Si and 4 electrons from substituted Mg in the octahedral position). This corresponds to the negative charge of 0.375 electrons per formula unit of $Al_2Si_4O_{10}(OH)_2$ and it also satisfies the requirement of natural Wyoming montmorillonite bearing negative charge of 0.25 to 0.6 electrons for the same formula (Bohn et al., 1979; Moore et al., 1989). A complete 2:1 layer containing an octahedral aluminum oxide layer sandwiched by two SiO_4 tetrahedral layers was used. The charge to each of the atoms in the structure was assigned based on previous works (Skipper et al., 1995a; Skipper et al., 1995b) and given in Table 3. The H atoms in structural OH groups are assigned to have the positive charge found in the water molecule for MCY model (see Chapter I). For the atomic charge for the oxygen, -0.8e from the earlier semi-empirical calculation was used

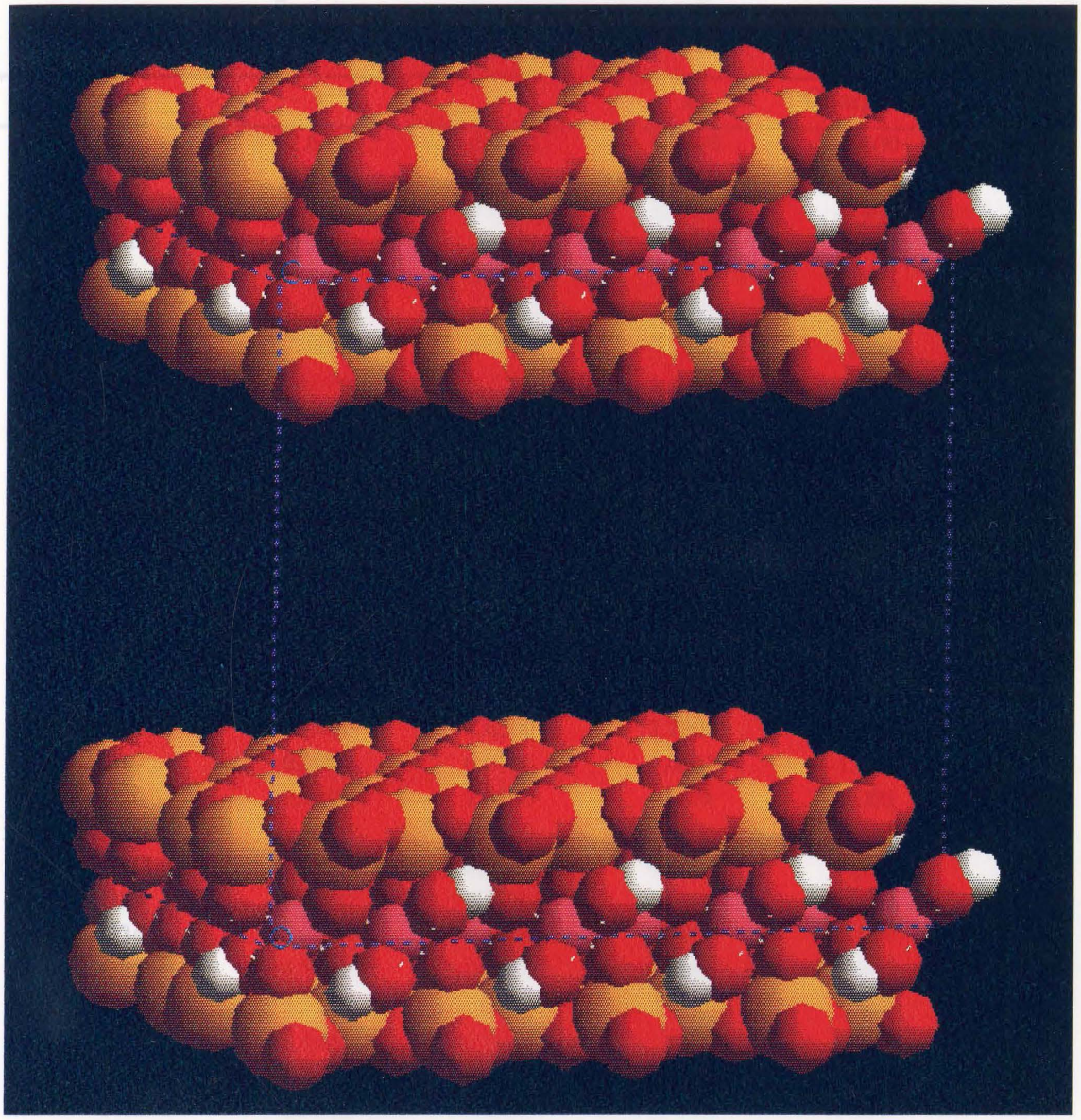

Figure 17. Unit Lattice.
Clay montmorillonite unit lattice; contains 4x2x1 unit cells from X-ray crystallography. A slab size of 21.12 Å by 18.28 Å by 6.56 Å of clay is used. The space between two clay layers is called interlayer spacing.

Table 3. Atomic Charge (e) of the Clay Atoms in the Fragment and Their Cartesian Coordinates (Å). See ref. (Skipper et al., 1995b).

Atom	x	y	z	Charge (e)
O1	2.6400	0.0000	3.2800	-0.800
O2	1.3200	2.2800	3.2800	-0.800
O3	3.9600	2.2800	3.2800	-0.800
O4	5.2800	0.0000	1.0601	-1.717
H5	6.1615	0.0000	1.4341	0.717
Si6	2.6400	1.5200	2.7300	1.200
Si7	0.0000	3.0500	2.7300	1.200
O8	2.6400	1.5200	1.0601	-1.000
O9	0.0000	3.0500	1.0601	-1.000
Al10	4.4000	1.5200	0.0000	3.000
Al11	4.4000	7.6200	0.0000	3.000
O12	0.0000	4.5700	3.2800	-0.800
O13	3.9600	6.8500	3.2800	-0.800
O14	1.3200	6.8500	3.2800	-0.800
O15	2.6400	4.5700	1.0601	-1.717
H16	3.5215	4.5700	1.4341	0.717
Si17	0.0000	6.0900	2.7300	1.200
Si18	2.6400	7.6200	2.7300	1.200
O19	0.0000	6.0900	1.0601	-1.000
O20	2.6400	7.6200	1.0601	-1.000
Al21	1.7600	6.0900	0.0000	3.000
Al22	1.7600	3.0500	0.0000	3.000
O23	0.8800	0.0000	-3.2800	-0.800
O24	2.2000	6.8600	-3.2800	-0.800
O25	4.8400	6.8600	-3.2800	-0.800
O26	3.5200	0.0000	-1.0601	-1.717
H27	2.6385	0.0000	-1.4341	0.717
Si28	0.8800	7.6200	-2.7300	1.200
Si29	3.5200	6.0900	-2.7300	1.200
O30	0.8800	7.6200	-1.0601	-1.000
O31	3.5200	6.0900	-1.0601	-1.000
O32	3.5200	4.5700	-3.2800	-0.800
O33	4.8400	2.2900	-3.2800	-0.800
O34	2.2000	2.2900	-3.2800	-0.800
O35	0.8800	4.5700	-1.0601	-1.717
H36	0.0015	4.5700	-1.4341	0.717
Si37	3.5200	3.0500	-2.7300	1.200
Si38	0.8800	1.5200	-2.7300	1.200
O39	3.5200	3.0500	-1.0601	-1.000
O40	0.8800	1.5200	-1.0601	-1.000

(Delville, 1992). Al and substituted Mg in the octahedral sheet are assigned to have unscreened ionic charge of +2e and +3e. The substitutional disorder for the constructed 4x2x1 clay model was carried out within Cerius2 molecular simulation software package to consider the negative charge of clay due to its isomorphic substitutions in the octahedral Al^{3+} by Mg^{2+} and in the tetrahedral Si^{4+} by Al^{3+}. These assigned ionic formal charges of octahedral metals are balanced by placing -1e on each of the coordinating O atoms (apical O of the SiO_4 tetrahedra).

In summary, the assignment of atomic charges we used and previously used by Skipper and co-workers is with respect to oxygens in the tetrahedral silicate layer. Other atoms are adjusted or assigned to give the clay neutrality or to consider the formal charge of the octahedral metal atoms. This approach is valid because the previous *ab*-initio studies suggest that the valence electrons in small fragments of clay are centered on the oxygen atoms. The rough treatment of formal charge assignment can be justified when we consider that the net negative charge of montmorillonite clay comes mostly from the tetrahedral layer not from the octahedral layer due to its remote (> 3 Å) location from the basal plane surface of the clay mineral.

The inter-atomic potentials for clay to metal complex were obtained from the parameterized Universal Force Field (UFF) without attempting any separate quantum energy parameterization due to the large numbers of the atoms in the metal complex of interest with respect to the clay fragment.

The total energy of the system, in which a metal complex is interacting with the clay surface, is expressed as a sum of bonded interactions and non-bonded interactions:

[49] $E_{total} = E_{bonded} + E_{non-bonded}$

The bonded interactions consist of bond stretching, bond angle bending, dihedral angle torsion, and inversion terms.

[50] $E_{bonded} = E_{bond} + E_{angle} + E_{torsion} + E_{inversion}$

The non-bonded interactions consist of electrostatic (coulombic) and van der Waals terms.

[51] $E_{non-bonded} = E_{coul} + E_{vdw}$

The electrostatic energy is given by

[52] $E_{coul} = C_o \sum_i \sum_{j>i} \left({Q_i Q_j}/{R_{ij}} \right) \varepsilon$

where Q_i and Q_j are atomic charges in electron units; R_{ij} is the distance between atoms in Å; ε is dielectric constant ($\varepsilon = 1$ for vacuum); and C_o is a conversion factor (332.0637); resulting E_{coul} in kcal/mol (Skipper et al., 1995).

Lennard-Jones 12-6 potentials are used for van der Waals interaction:

[53] $E_{vdw}(r) = D_o \left[\left({R_o}/{R} \right)^{12} - 2\left({R_o}/{R} \right)^{6} \right]$

where D_o is bond strength (well depth) in kcal/mol; R_o is the equilibrium bond length in Å; and R is bond length in Å. The values of the van der Waals parameters shown in this equation for the atoms in the clay are given in Table 4.

For the long range corrections of non-bonded interactions, we first attempted the spline switching method. Within the spline-on/spline-off range (8.0 Å ~ 8.5 Å), the non-bonded interaction energy is attenuated by the gradual function instead of the abrupt

change. Beyond the spline-off distance, nonbonded interactions were ignored (> 8.5 Å). This relatively narrow on/off range method gave quick results. However, this treatment does not account for the possible longer range (> 8.5 Å) non-bonded interactions which may be of importance in periodic models like ours.

The Ewald summation technique was then attempted and the results obtained were far different from the earlier values using spline method. Therefore, the spline method may have substantial error which is associated with the cutoff distance. The border artifacts due to our periodic infinite system seemed to be solved by this two sum technique developed by Karasawa and co-workers (Karasawa et al., 1989). Ewald summation converts the coulomb and dispersion terms into two different summations (one in real space and one in reciprocal space). Estimation of the Ewald cutoff and convergence parameter is known to be difficult and the automated estimation of these parameters developed by Karasawa and co-workers (Karasawa et al., 1989) was used within Cerius^2.

b. Metal Complex Models

Ab-initio molecular orbital calculations with STO-3G basis set were performed on $Co(sep)^{3+}$, $Ru(NH_3)_6^{3+}$, $Co(en)_3^{3+}$, $Co(NH_3)_6^{3+}$, and $Co(bpy)_3^{3+}$ using the Spartan quantum mechanics software package (Spartan 3.0, 1993). *Ab*-initio calculations on same complexes with divalent charges, $Co(sep)^{2+}$, $Ru(NH_3)_6^{2+}$, $Co(en)_3^{2+}$, $Co(NH_3)_6^{2+}$, and $Co(bpy)_3^{2+}$, were also carried out. The van der Waals parameters (UFF) for these metal complexes are listed in Table 4.

Table 4. van der Waals Parameters Used for Metal Complexes and Clay Atoms (in eq. 53).

Atom	***D_o (kcal/mol)***	***R_o (Å)***
Co	0.0140	2.8720
Ru	0.0560	2.9630
N	0.0690	3.6600
C	0.1050	3.8510
H	0.0440	2.8860
Al	0.5050	4.4990
Si	0.4020	4.2950
O	0.0600	3.5000

The basis functions used for the metal complexes were STO-3G basis set. The Gaussian exponents α and linear expansion coefficients d have been chosen as least-squares fits to Slater orbitals with exponent ζ=1. The standard valence-shell scale factor ζ_{3d} for cobalt complexes was set to be 4.10 and ζ_{4d} for ruthenium complexes was set to be 3.20. The detailed method of these STO-3G minimal basis sets for first and second-row transition metals is found in a previous work by Pietro and co-workers (Pietro et al., 1983). The use of the STO-3G basis functions for transition metal complexes such as $Ru(bpy)_3^{2+}$ and $Co(en)_3^{3+}$ were also found in the earlier work by Sato and co-workers (Sato et al., 1992). They also used the effective charge data from this STO-3G ab-initio calculation to study some experimental results of clay-metal complex adsorption.

The atomic charges of the metal complexes from this *ab-initio* molecular orbital calculation are determined by the Molecular Electrostatic Potential (MEP) fitting scheme (Chirlian et al., 1987). MEP is a quantum mechanical property which we can calculate from the density matrix by solving Schrödinger's equation. The atomic charges with MEP are obtained when we fit the electrostatic potential to a series of point charges (often called grid of points) around the molecule centered on the atomic nuclei. In our computation, the electrostatic energy may be the most important parameter for both minimization and dynamics. MEP has been the standard tool for analyzing and predicting molecular reactivity. Detailed theory and the equation are found in Section E-2 of Chapter V (eq 47).

c. Simulation Methods

The montmorillonite clay surface was set to be rigid throughout both lattice minimization and molecular dynamics calculations. A previous molecular dynamics study of water near silicate surface also used rigid parallel planes of oxygen atoms to describe silicate surface (Low et al., 1984). Recent computer simulations of clays have started to use the non-rigid clay system in which the deformation of the clay layer structure due to the interaction either with the interlayer water content or with the guest molecules bound to clay are taken into account (Skipper et al., 1991; Breu et al., 1995). However, a large number of simulations still use a rigid structure of the clay for the clay-water or clay-compound interaction (Karaborni et al., 1996; Boek et al., 1995a; Keldsen et al., 1994; Delville, 1992; Sato et al., 1992a; Sato et al., 1992b). Because our goal is to obtain **relative** trends between cationic complexes we felt justified in fixing the lattice as an "inert" matrix. We can then focus on the difference in the movement of cationic complex within the region. Our rigid clay simulation is also justified by the fact that we are only taking part of the clay structure in the unit cell and the fact that the number of the component atoms in the metal complex is exceeded by that of the clay model. Full atomic motion was allowed for the corresponding freely moving metal complex. Lattice minimization was followed by the molecular dynamics simulation in each metal complex-clay system.

1) Minimization.

Lattice minimization of the metal complex within the system was performed with basal spacing of 20 Å (the vertical distance between octahedral aluminum layers of bottom clay surface to another octahedral aluminum layers in upper clay surface). The 20 Å basal spacing was chosen to match the swelling of the clay platelets in the electrolyte concentration used (~ 0.01M NaCl). This 20 Å basal spacing corresponds to 14.56 Å of interlayer spacing which defines the space for the diffusional motion of the cationic complexes. Each single metal complex was located in the center of the unit cell for the simulation. A conjugated gradient 200 algorithm was employed for 3000 steps (Fletcher et al., 1964).

The vacuum permitivity (ε) of 1.0 was used for the in-vacuo circumstances throughout the computation. Here we used the dielectric continuum model without applying the distance dependent dielectric which maybe useful for isolated biological system. A more complete treatment will be possible by including water molecules instead of treating the system in-vacuo. However, our focus, again, is to see the ***relative*** difference in the interaction of a single cationic complex with clay. Our unit cell only include single cationic complex and clay bilayer. Other effects such as probe-probe, anion effect, salt effect, and water molecules were not considered. Assuming these parameters within the unit cell for each probe molecule are of no great importance, we compared the general trends of clay-complex interaction among different probes.

The convergence of the minimization was obtained when root mean square force (RMS force) is less than 0.1 (kcal/mol)/Å.

2) Molecular Dynamics Calculation (MD)

We have used the same procedure for all metal complexes. An isothermal equilibrium dynamics ensemble was chosen. The constant volume and constant temperature condition was used for all metal complex systems throughout the dynamics time span. The number of resulting pair interactions was 37,755 for cobalt sepulchrate complexes, 27,916 for cobalt ethylenediamine complexes, 18,734 for ruthenium hexaamine complexes and 45,300 for cobalt bipyridine complexes. The pair list was updated every 50 steps. The time step used in the dynamics was 1fs (0.001 ps) because the system always includes the hydrogen atoms where the fastest motions (hydrogen stretches) have periods of 0.01 ps (ref. Cerius2, 1992). The time step must be significantly smaller (about factor of 10) than the fastest local motion for the numerical integration of Newton's equations of motion to be stable; that is, to generate a reliable molecular dynamics trajectory. The temperature of the system was maintained constant at 300K by coupling it with the Hoover thermal bath (Hoover, 1985), MD calculations were performed for 70 ps on the whole system. In the first 14 ps, the system was gradually heated by performing MD runs of 2.0 ps at the following temperatures: 10, 50, 100, 150, 200, 250, and 300 K. In all simulations a constant energy value was obtained within the 2.0 ps run. Another 56 ps of constant volume and constant temperature dynamics was performed at 300 K and used for data analysis.

B. Diffusion of Cobalt (II) Complexes Containing 2,2´-Bipyridine, 2,2´-Bipyrazine, and 2,2´-Bipyrimidine Ligands in Montmorillonite.

1. Materials and Methods Used for Experiments

a. Chemicals

$[Co(bpy)_3](ClO_4)_2 \cdot 2H_2O$, $[Co(bpm)_3](ClO_4)_2 \cdot 2H_2O$ and $[Co(bpz)_3](ClO_4)_2 \cdot 2H_2O$ were prepared in the laboratory procedure (Wang, 1997). Elemental analysis of $[Co(bpy)_3](ClO_4)_2$ ($CoC_{30}H_{24}O_8N_6Cl_2$, calculated (%) C, 49.60; H, 3.34 and N, 11.57, found C, 49.60; H, 3.31 and N, 11.61), $[Co(bpm)_3](ClO_4)_2 \cdot H_2O$[1] ($CoC_{24}H_{20}O_9N_{12}Cl_2$, calculated (%) C, 38.42; H, 2.69 and N, 22.41, found C, 38.49; H, 2.45 and N, 22.38) and $[Co(bpz)_3](ClO_4)_2 \cdot H_2O$ ($CoC_{24}H_{20}O_9N_{12}Cl_2$, calculated (%) C, 38.42; H, 2.69 and N, 22.41, found C, 38.43; H, 2.55 and N, 22.17). These compounds will be referred to as $Co(bpy)_3^{2+}$, $Co(bpm)_3^{2+}$, and $Co(bpz)_3^{2+}$ for the rest of the study.

The clay sample used in this study was SWy-1 sodium montmorillonite which was purified as previously described (Stein et al., 1995; Lee et al., 1990; Fitch et al., 1988). The clay has a cation exchange capacity of 0.76 mmole equivalent charge per gram (mmeq/g) of clay.

b. Spectroscopic Measurements.

Clay/Complex equilibrium adsorption was studied by UV-VIS spectroscopy. In a 1 mL plastic centrifuge tube, mixture of a clay suspension containing 350 μg of SWy-1 and a aqueous solution containing cobalt complex was shaken with vortex mixer for

[1] The ligand abbreviation "bpm" is often used for 4,4´-bipyrimidine and "bpym" is used for 2,2´-bipyrimidine. Here, we consider "bpm" as 2,2´-bipyrimidine for simplicity.

30 seconds and sat to equilibrium for 50 minutes. The supernatant was separated by high speed centrifugation and the amount of unbound cobalt complex in the supernatant was measured by UV-VIS absorption with Hewlett Packard 8452A Diode Array Spectrophotometer.

c. Electrochemical Measurements.

Transient interactions with the clay were studied by multi-sweep cyclic voltammetry (MSCV). Clay-modified electrodes (CME) were prepared by spin-coating the glassy carbon working electrode with 5 mL of clay suspension containing 17.5 g/L of the SWy-1 montmorillonite. As discussed in Chapter II, clay films coated in this method have a well ordered structure of overlapping clay layers on the electrode surface (Fitch et al., 1993; Fitch et al., 1993). The clay-modified electrode was then placed in a electrochemical cell containing 6 mL of N_2-purged solution for CV measurement. In subsequent experiments, the clay-modified electrode was first soaked and the potential scanned in 0.01 or 0.1 M of NaCl solution for 5 minutes prior to sample measurement to allow to swelling and for impurities in the film be removed. The clay-modified electrode was quickly transferred to the sampling solution containing 1.5 cobalt(II) complex as a probe molecule and 0.01 M or 0.1 M NaCl as supporting electrolyte. Cyclic voltammograms were obtained on a PAR 273 potentiostat with a Houston 2000 XY recorder using a 5.5 mm-diameter glassy carbon as working electrode and Ag/AgCl as reference electrode.

2. *Methods in Computer Simulations*

a. Modeling of the system.

For the clay model, the same single clay model with same charge information as used in earlier work (See this method section *A.2.a.*) was used. For the metal complexes in this study, *ab-initio* molecular orbital calculations with STO-3G basis set were performed on $Co(bpy)_3^{2+}$, $Co(bpm)_3^{2+}$, and $Co(bpz)_3^{2+}$ using the Spartan quantum mechanics software package. *Ab*-initio calculations on same complexes with trivalent charges, $Co(bpy)_3^{3+}$, $Co(bpm)_3^{3+}$, and $Co(bpz)_3^{3+}$, were also carried out. The structure of these relatively symmetric metal complexes have been obtained by minimization with Universal forcefield and used for *ab-initio* calculation. The van der Waals parameters (UFF) for cobalt complexes are listed in Table 4. The atomic charges have been obtained by Molecular Electrostatic Potential (MEP) fitting scheme.

b. Simulation Methods.

The montmorillonite clay surface was set to be rigid throughout both energy minimization and molecular dynamics calculations. For the corresponding cobalt complex, full atomic motion was allowed to describe its diffusive motion in the interlayer region. Lattice minimization was followed by the molecular dynamics simulation in each metal complex-clay system.

1) Minimization.

Lattice minimization of the metal complex within the system was performed with basal spacing of 20 Å. Each single cobalt complex was located in the center of the

unit cell for the minimization. A conjugated-gradient 200 algorithm was employed for 3000 steps. The vacuum permitivity of $\varepsilon=1.0$ was used for the in-vacuo system. The convergence of the minimization was obtained when root mean square force (RMS force) is less than 0.1 (kcal/mol)/Å.

2) Molecular Dynamics Calculation (MD)

We have used the same procedure for all cobalt complexes. An isothermal equilibrium dynamics ensemble was chosen. The constant volume and constant temperature condition was used for all metal complex systems throughout the dynamics time span. The number of resulting non-bond interactions was 45,300 for $Co(bpy)_3^{2+}$, 41,159 for $Co(bpm)_3^{2+}$, and 41,091 for $Co(bpz)_3^{2+}$. The pair list was being updated every 50 steps. The time step used in the dynamics was 1fs (0.001 ps). The temperature of the system was maintained constant at 300K by coupling it with the Hoover thermal bath (Hoover,1695). MD calculations were performed for 70 ps on the whole system. In the first 14ps, the system was gradually heated by performing MD runs of 2.0 ps at the following temperatures: 10, 50, 100, 150, 200, 250, and 300K. In all simulations a constant energy value was obtained within the 2.0 ps run. Another 56 ps of constant volume and constant temperature dynamics was performed at 300 K and used for data analysis. Another series of MD calculations were performed for 10ps at 300K without temperature increasing steps other than coupling with the Hoover heat bath in the beginning.

Chapter VII.

Results and Discussion

A. Diffusion of Intercalated Cationic Compounds, $Ru(NH_3)_6^{3+}$, $Co(en)_3^{3+}$, $Co(NH_3)_6^{3+}$, and $Co(sep)^{3+}$ in Montmorillonite

1. Cyclic Voltammetric Results

The multisweep cyclic voltammograms for the clay-modified electrode (CME) containing species of $Ru(NH_3)_6^{3+}$, $Co(en)_3^{3+}$, and $Co(sep)^{3+}$ are shown in Figure 18. The electrochemical study of $Co(NH_3)_6^{3+}$ has been substituted by that of $Ru(NH_3)_6^{3+}$ due to the extreme lability of the cobalt complex upon reduction (Fitch et al., 1996). First, notice that there is a peak shift between the bare electrode and the last peak of the CME. The peak shifts for $Ru(NH_3)_6^{3+}$, $Co(en)_3^{3+}$, and $Co(sep)^{3+}$, $Co(bpy)_3^{3+}$ were, -25 mV, -10 mV, -35 mV, and +10 mV respectively for the given experiment. Then, notice that all of the species showed significant peak development over time indicating that the flux of these electroactive species have been enhanced in the presence of the clay. Molecular mechanics (or minimization) between clay and these series of metal complexes may supply the information regarding the interaction between these electroactive metal complexes and clay.

molecule in terms of σ bonding and π back bonding, one should use Mulliken charge instead of MEP charge.

Also notice the atomic charges of multiple nitrogens in $Co(sep)^{2+}$ and $Co(sep)^{3+}$ are different. This may be due to the lack of symmetry for the complexes and consequent fitting procedure between total electrostatics of the grid point potential sum and the atomic charges lead to explicit charge value at the specific atomic location. The atomic charge of $Co(sep)^{3+}$ is less positive than that of $Co(sep)^{2+}$. This seems to be also strange but the topological MEP charge for complex $Co(sep)^{3+}$ is considered to have net charge of +3 instead of formal charge on cobalt. Then the grid point summation of electrostatics can account for the atomic charges to be more positive at the outer-sphere region of the molecule where the test point positive charge grid points are found. This may explain the discrepancy between the formal charge and MEP derived atomic charge for the well buried cobalt atoms in $Co(sep)^{2+}$ and $Co(sep)^{3+}$.

We do not claim that the cationic metal complex used for the MEP charge calculation is at the global minima. The structure of each complex was first constructed and minimized with UFF (Universal Forcefield parameter) without any atomic charge data. Then, the formal potential was redistributed to this minimized structure using Charge Equilibration (QEq) method developed by Rappé and co-workers that predict the charges given the geometry and electronegativities of the various atoms (Rappé et al., 1991). This QEq charge distributed complex is then minimized again to consider all possible coulombic interaction within the molecule. This structural information, after

Table 5. Atomic charges of cationic metal complexes.

(a) $Co(NH_3)_6^{3+}$ and $Ru(NH_3)_6^{3+}$.

Atom	$Co(NH_3)_6^{3+}$	$Ru(NH_3)_6^{3+}$
M (M = Co or Ru)	1.574	1.136
N	-0.740	-0.682
H	0.328	0.336
H	0.323	0.333
H	0.329	0.334

- Here atomic charges are shown for one ligand only.
- For $Co(NH_3)_6^{3+}$, atomic charge for N is between -0.729 and -0.755; and atomic charge for H is between 0.321 and 0.331.
- For $Ru(NH_3)_6^{3+}$, atomic charge for N is between -0.682 and -0.698; and atomic charge for H is between 0.325 and 0.340.

Table 5 Atomic charges of cationic metal complexes.
(b) Atomic charge of $Co(en)_3^{3+}$ (c) Atomic charge of $Co(bpy)_3^{3+}$.

Atom	Charge (e)
Co	1.063
N1	-0.315
H2	0.220
H3	0.251
N4	-0.290
H5	0.215
H6	0.251
C7	-0.025
H8	0.115
H9	0.080
C10	-0.061
H11	0.120
H12	0.087

Atom	Charge (e)*	Mulliken Charge(e)
Co	-1.177	1.326
N	0.265	-0.358
C1	0.135	0.123
C2	-0.162	-0.042
C3	0.107	0.005
C4	-0.098	-0.039
C5	-0.031	0.077
H6	0.138	0.125
H7	0.107	0.144
H8	0.124	0.132
H9	0.128	0.109

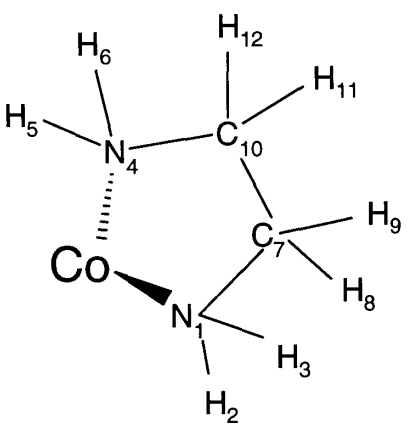

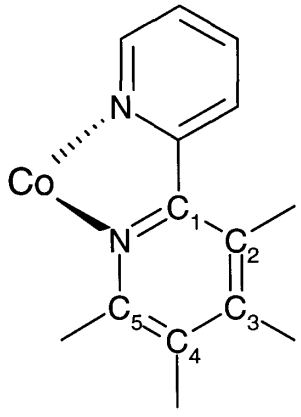

- * MEP (molecular electrostatic potential) charge
- Atomic charges are shown for one ligand only (figures also show the corresponding ligands). The difference in atomic charge between ligands are negligible (~0.01e).
- Atomic charges for $Co(bpy)_3^{3+}$ are different throughout the molecule. For complete information of atomic charges of $Co(bpy)_3^{3+}$, see Table 6.

Table 5 Atomic charge of cationic metal complexes.

Atomic charges; (d) $Co(sep)^{2+}$ (e) $Co(sep)^{3+}$.

Atom	Position	$Co(sep)^{2+}$	$Co(sep)^{3+}$
N	1	0.021	-0.011
Co	2	0.139	0.605
N	3	-0.105	-0.136
N	4	0.055	0.021
N	5	-0.076	-0.109
N	6	0.062	0.025
N	7	0.075	0.044
N	8	-0.357	-0.326
N	9	-0.320	-0.291
C	10	-0.008	-0.037
C	11	-0.016	-0.044
C	12	-0.087	-0.109
C	13	-0.252	-0.260
C	14	-0.039	-0.058
C	15	-0.161	-0.172
C	16	-0.050	-0.066
C	17	-0.056	-0.077
C	18	-0.219	-0.227
C	19	-0.105	-0.126
C	20	-0.054	-0.078
C	21	-0.063	-0.087
H	22	0.113	0.137
H	23	0.087	0.122
H	24	0.100	0.126
H	25	0.108	0.141
H	26	0.120	0.144
H	27	0.120	0.151
H	28	0.102	0.123
H	29	0.121	0.154
H	30	0.102	0.128
H	31	0.078	0.112
H	32	0.104	0.120
H	33	0.092	0.127
H	34	0.111	0.134
H	35	0.082	0.115
H	36	0.079	0.099
H	37	0.066	0.104
H	38	0.108	0.143
H	39	0.089	0.112
H	40	0.118	0.144
H	41	0.114	0.146
H	42	0.107	0.132
H	43	0.113	0.145
H	44	0.120	0.143
H	45	0.097	0.131

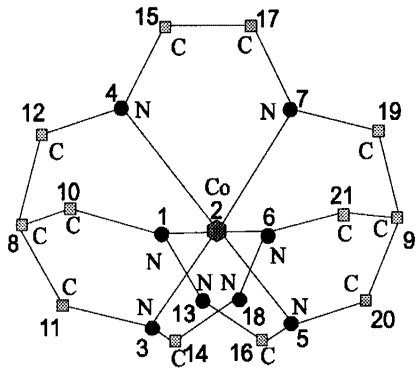

discarding the QEq charge data (which was only used to obtain chemical structure), is then further used for the quantum mechanical calculation to obtain the MEP charge for each atom in the complex by *ab*-initio method. No geometry optimization was carried out for the ab-initio calculation (i.e. single point energy calculation) due to both the large number of atoms and the complexity of the basis set (which include metal d orbitals). Therefore, we do not claim that the structure of each cationic complex used for our lattice minimization and molecular dynamics for the clay-complex system is at the global minimum. Also notice that the lattice minimization and the minimization for each complex was at 0 K.

The problem involved in the use of cationic complex possibly located at a local minimum instead of global one may be further improved by the molecular dynamics at room temperature. The use of statistical average value instead of single minimized value for the clay-complex interaction should give a more realistic picture of the molecular interaction. We used the molecular dynamics to describe the diffusional motion of the cationic complex within the clay.

The atomic charge of $Co(bpy)_3^{2+}$, $Co(bpy)_3^{3+}$, $Co(bpm)_3^{2+}$, $Co(bpm)_3^{3+}$, $Co(bpz)_3^{2+}$ and $Co(bpz)_3^{3+}$ are shown in Table 6. The differences in the atomic charges for the same element are due to the use of the structure minimized QEq charge and the MEP calculation based on this non-optimized structure as explained above. The difference in the atomic charges of the equivalent atoms are attributed to the non-global minima of the structures. The discrepancy between the formal charge and the MEP derived atomic charge for cobalt in each divalent and trivalent complex can be

Table 6. Atomic Charge of Cobalt Complexes
(a) Atomic Charges of $Co(bpy)_3^{2+}$

Atom	Charge	Atom	Charge
H 1	0.0924	C 32	0.0034
C 2	-0.1084	C 33	0.0785
C 3	-0.0859	N 34	0.2313
N 4	0.2570	C 35	-0.0932
Co 5	-0.9108	C 36	-0.1251
N 6	0.2458	C 37	0.0492
C 7	0.1287	C 38	-0.1754
C 8	0.1161	H 39	0.1209
N 9	0.2726	H 40	0.0853
C 10	0.0073	H 41	0.0974
C 11	-0.1011	H 42	0.1201
C 12	0.1157	H 43	0.1161
C 13	-0.1584	H 44	0.0918
H 14	0.1360	H 45	0.1136
H 15	0.1004	N 46	0.2855
H 16	0.1212	C 47	-0.1017
H 17	0.1433	C 48	-0.1327
C 18	-0.1572	C 49	0.0358
C 19	0.1212	C 50	-0.1652
C 20	-0.1210	C 51	0.0262
C 21	0.0189	C 52	0.0163
H 22	0.1406	C 53	-0.1624
H 23	0.1293	C 54	0.0295
H 24	0.1009	H 55	0.0836
H 25	0.1327	H 56	0.1171
N 26	0.2227	H 57	0.1185
C 27	-0.0655	H 58	0.0840
C 28	-0.1194	H 59	0.0995
C 29	0.0294	H 60	0.1110
H 30	0.0807	H 61	0.1255
C 31	-0.1696		

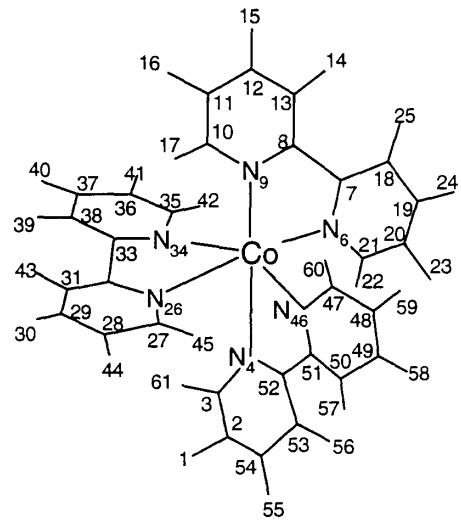

Table 6. Atomic Charge of Cobalt Complexes
(b) Atomic Charges of $Co(bpy)_3^{3+}$

Atom	Charge	Atom	Charge
H 1	0.1201	C 32	0.0767
C 2	-0.0830	C 33	0.1350
C 3	-0.0245	N 34	0.2653
N 4	0.2762	C 35	-0.0306
Co 5	-1.1778	C 36	-0.0982
N 6	0.2648	C 37	0.1071
C 7	0.1035	C 38	-0.1624
C 8	0.0946	H 39	0.1377
N 9	0.2847	H 40	0.1071
C 10	-0.0314	H 41	0.1240
C 11	-0.0917	H 42	0.1281
C 12	0.1029	H 43	0.1358
C 13	-0.1465	H 44	0.1228
H 14	0.1371	H 45	0.1095
H 15	0.1064	N 46	0.3033
H 16	0.1202	C 47	-0.0325
H 17	0.1283	C 48	-0.1021
C 18	-0.1448	C 49	0.1003
C 19	0.1080	C 50	-0.1447
C 20	-0.1126	C 51	0.1057
C 21	-0.0195	C 52	0.0707
H 22	0.1272	C 53	-0.1345
H 23	0.1283	C 54	0.0931
H 24	0.1070	H 55	0.1079
H 25	0.1333	H 56	0.1335
N 26	0.2518	H 57	0.1351
C 27	-0.0021	H 58	0.1075
C 28	-0.0914	H 59	0.1269
C 29	0.0983	H 60	0.1205
H 30	0.1070	H 61	0.1205
C 31	-0.1430		

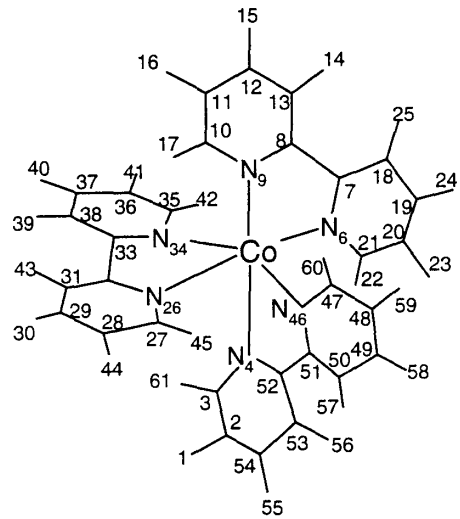

Table 6. Atomic Charge of Cobalt Complexes
(c) Atomic Charges of $Co(bpm)_3^{2+}$

Atom	Charge	Atom	Charge
H 1	0.4606	C 29	0.5267
C 2	-0.6275	C 30	0.4316
C 3	0.5377	C 31	0.3588
N 4	0.0242	C 32	0.1558
Co 5	-0.3922	C 33	0.1014
N 6	0.1683	N 34	-0.3626
C 7	0.1845	C 35	0.1521
C 8	0.0919	C 36	0.5215
N 9	0.4352	C 37	0.0243
C 10	-3.2183	C 38	-0.6386
C 11	0.5435	H 39	-0.6336
C 12	-0.6538	H 40	0.5492
C 13	0.5705	H 41	0.0224
H 14	0.0231	H 42	-0.3726
H 15	-0.4147	H 43	0.1610
H 16	0.1697	H 44	0.1582
H 17	0.2295	H 45	0.0978
C 18	0.0904	N 46	0.4428
C 19	0.3476	C 47	0.4867
C 20	0.4012	C 48	0.4656
C 21	0.4549	C 49	-0.6318
H 22	0.1345	C 50	0.0972
H 23	0.0946	C 51	0.5531
H 24	-0.3798	C 52	0.0140
H 25	0.1637	C 53	-0.3927
N 26	0.5330	C 54	0.1665
C 27	0.0127	H 55	0.1675
C 28	-0.6076		

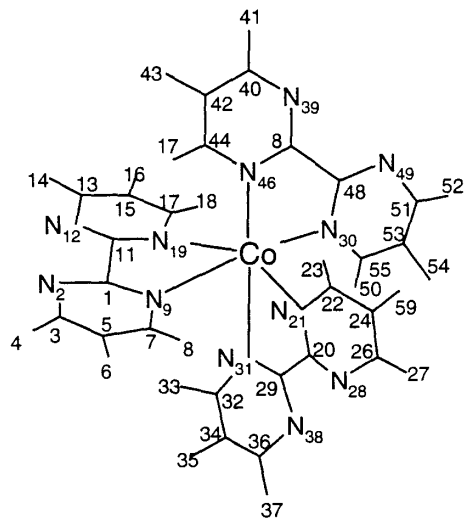

Table 6. Atomic Charge of Cobalt Complexes

(d) Atomic Charges of $Co(bpm)_3^{3+}$

Atom	Charge	Atom	Charge
H 1	0.5061	C 29	0.5713
C 2	-0.6268	C 30	0.3975
C 3	0.5996	C 31	0.3251
N 4	0.0400	C 32	0.2180
Co 5	-0.4058	C 33	0.1073
N 6	0.1877	N 34	-0.3683
C 7	0.2331	C 35	0.1746
C 8	0.0956	C 36	0.5866
N 9	0.3943	C 37	0.0428
C 10	-3.1104	C 38	-0.6344
C 11	0.5553	H 39	-0.6219
C 12	-0.6419	H 40	0.5900
C 13	0.6113	H 41	0.0374
H 14	0.0374	H 42	-0.3667
H 15	-0.4098	H 43	0.1785
H 16	0.1863	H 44	0.1870
H 17	0.2522	H 45	0.1023
C 18	0.0963	N 46	0.4137
C 19	0.3246	C 47	0.5038
C 20	0.4565	C 48	0.5129
C 21	0.4146	C 49	-0.6327
H 22	0.2013	C 50	0.1031
H 23	0.1006	C 51	0.6205
H 24	-0.3896	C 52	0.0309
H 25	0.1869	C 53	-0.4089
N 26	0.6011	C 54	0.1877
C 27	0.0318	H 55	0.2194
C 28	-0.6062		

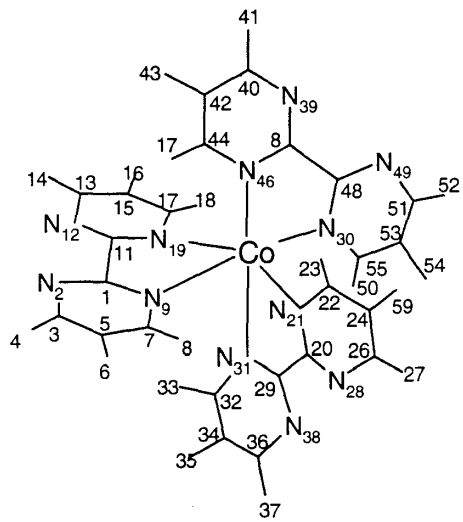

Table 6. Atomic Charge of Cobalt Complexes

(e) Atomic Charges of $Co(bpz)_3^{2+}$

Atom	Charge	Atom	Charge
C 1	-0.2945	H 29	0.0528
C 2	0.3762	C 30	-0.2006
H 3	0.0614	N 31	0.9221
N 4	-0.5558	Co 32	-2.6188
C 5	0.4513	C 33	-0.4356
H 6	0.0368	H 34	0.1948
C 7	-0.5443	C 35	0.4635
H 8	0.1847	H 36	0.0456
N 9	0.9870	N 37	-0.4979
C 10	0.3434	C 38	0.3547
C 11	-0.2768	C 39	-0.3528
C 12	0.3809	H 40	0.0649
H 13	0.0566	N 41	0.8796
N 14	-0.5234	C 42	-0.4843
C 15	0.4305	H 43	0.1792
H 16	0.0378	C 44	0.4514
C 17	-0.4892	H 45	0.0368
H 18	0.1782	N 46	-0.5658
N 19	0.9162	C 47	0.4401
C 20	-0.2557	H 48	0.0386
H 21	0.0739	C 49	-0.1513
N 22	0.9433	N 50	0.8461
C 23	-0.4289	C 51	-0.4590
H 24	0.1816	H 52	0.1742
C 25	0.4424	C 53	0.4266
H 26	0.0572	H 54	0.0402
N 27	-0.5120	N 55	-0.5152
C 28	0.4113		

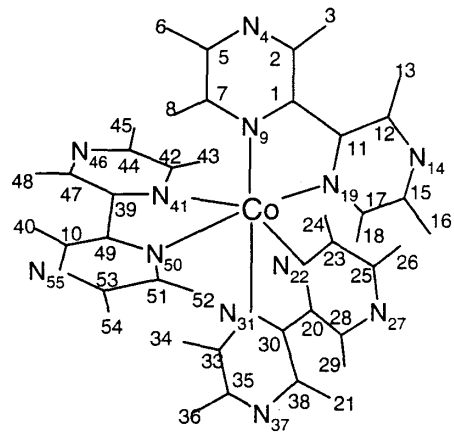

Table 6. Atomic Charge of Cobalt Complexes
(f) Atomic Charges of $Co(bpz)_3^{3+}$

Atom	Charge	Atom	Charge
C 1	-0.2253	H 29	0.0629
C 2	0.3717	C 30	-0.2126
H 3	0.0855	N 31	0.9323
N 4	-0.4808	Co 32	-2.6681
C 5	0.4566	C 33	-0.4563
H 6	0.0650	H 34	0.1968
C 7	-0.4759	C 35	0.4782
H 8	0.1976	H 36	0.0561
N 9	0.9940	N 37	-0.4850
C 10	0.3645	C 38	0.3711
C 11	-0.2630	C 39	-0.2860
C 12	0.3980	H 40	0.0822
H 13	0.0755	N 41	0.8777
N 14	-0.4854	C 42	-0.4156
C 15	0.4634	H 43	0.1902
H 16	0.0618	C 44	0.4531
C 17	-0.4512	H 45	0.0639
H 18	0.1918	N 46	-0.4933
N 19	0.9342	C 47	0.4377
C 20	-0.2695	H 48	0.0610
H 21	0.0844	C 49	-0.1456
N 22	0.9513	N 50	0.8665
C 23	-0.4456	C 51	-0.4327
H 24	0.1828	H 52	0.1881
C 25	0.4545	C 53	0.4614
H 26	0.0682	H 54	0.0628
N 27	-0.4962	N 55	-0.4842
C 28	0.4294		

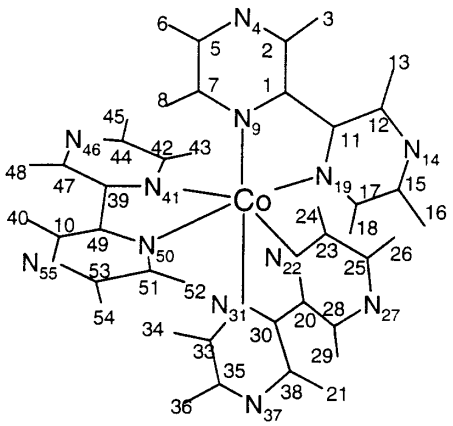

explained by the MEP grid point charge fitting scheme and the shielded effect of the well buried cobalt atom. The more positive atomic charges for cobalt atoms in Co(2+) complexes (less negative) than those for cobalt atoms in Co(3+) complexes are consistent with the previous results for the $Co(sep)^{2+}$ and $Co(sep)^{3+}$.

B. Motion of Intercalated Cationic Compounds, $Ru(NH_3)_6^{3+}$, $Co(en)_3^{3+}$, $Co(NH_3)_6^{3+}$, and $Co(sep)^{3+}$ in Montmorillonite

1. Cyclic Voltammetric Results

The multisweep cyclic voltammograms for the clay-modified electrode (CME) containing species of $Ru(NH_3)_6^{3+}$, $Co(en)_3^{3+}$, and $Co(sep)^{3+}$ are shown in Figure 18. The electrochemical study of $Co(NH_3)_6^{3+}$ has been substituted by that of $Ru(NH_3)_6^{3+}$ due to the extreme lability of the cobalt complex upon reduction (Fitch et al., 1996). First, notice that there is a peak shift between the bare electrode and the last peak of the CME. The peak shifts for $Ru(NH_3)_6^{3+}$, $Co(en)_3^{3+}$, and $Co(sep)^{3+}$, $Co(bpy)_3^{3+}$ were, -25 mV, -10 mV, -35 mV, and +10 mV respectively for the given experiment. Then, notice that all of the species showed significant peak development over time indicating that the flux of these electroactive species have been enhanced in the presence of the clay. Molecular mechanics (or minimization) between clay and these series of metal complexes may supply the information regarding the interaction between these electroactive metal complexes and clay.

The capability of montmorillonite clay to adsorb electroactive probes is shown

Figure 18. Multisweep Cyclic Voltammograms (MSCV) for the Clay-modified Electrode (CME) Containing $Ru(NH_3)_6^{3+}$, $Co(en)_3^{3+}$, and $Co(sep)^{3+}$.
MSCV obtained at 50 mV/s;
(a) 0.01 mM $Ru(NH_3)_6Cl_3$, 0.01 M Na_2SO_4, potential swept between 0 and -0.7 V vs. SCE. Scale is 500 nA.
(b) 0.5 mM $Co(sep)Cl_3$ in 0.1 M NaCl, potential swept between 0.1 and -0.85 V vs. SCE. Scale is 500 nA.
(c) 0.5 mM $Co(en)_3Cl_3$ in 0.1 M NaCl, potential swept between 0.3 and -0.85 V vs. SCE. Scale is 500 nA.
The single sweep, time invariant, signal for the bare electrode is also indicated for each metal complex (Fitch et al., 1996).

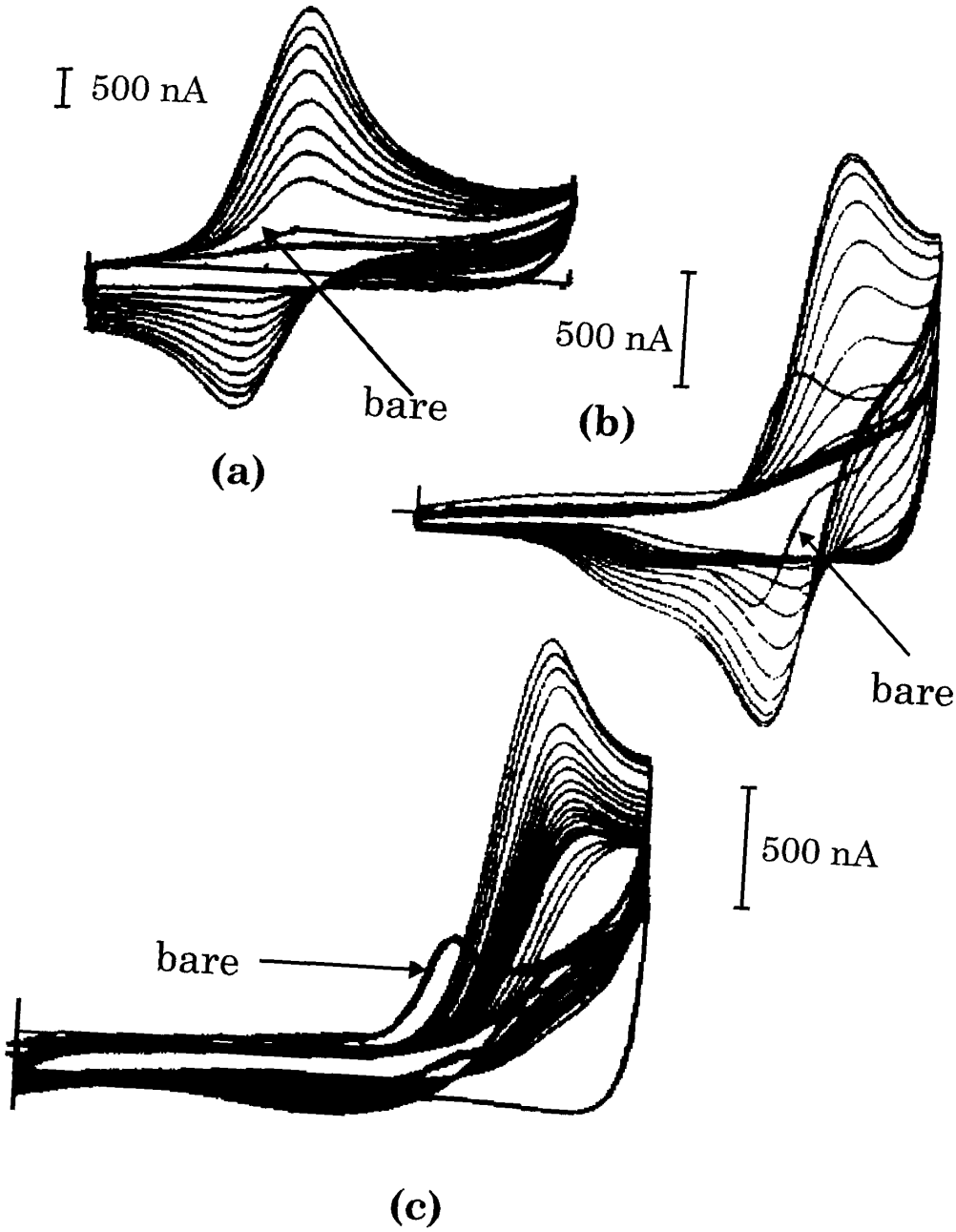
500 nA
bare
(a)
500 nA
(b)
bare
500 nA
bare
(c)

as the increased peak height (current) after each scan as shown in Figure 18. The cathodic peak development over the series of potential sweeps shown as contour-like lines also reflects the differential amount of electroactive species available for reduction at the electrode over time. This can be monitored more readily if one plots the peak height (current in A) against the time change. Instead of the direct plot between current and time taken, the ratio of peak current of CME to that of bare has been plotted against time (see Figure 19). This normalizes for changes in electrode area. Our greatest interest, the diffusional behavior of each metal complex, is represented as its increased current over time.

2. Lattice Energy Minimization to Account for Potential Shifts in CME

The total energy of the minimized structure of each compound is obtained from lattice minimization with the parameters both from preceding *ab*-initio molecular electrostatic potential (MEP) charge calculation (Table 5) and the UFF forcefield sets. The total energy (given by eq 49), van der Waals energy (eq 53), and the electrostatic energy (eq 52) obtained from minimization are listed in Table 7.

We do not claim that this structure is at the global minimum as explained above. However, the energy of the minimized structure may be able to tell the relative trends in the interaction energy between the clay and the each cationic complex.

The radius, in Å, was determined for each cationic complex after the lattice minimization by taking the greatest length between central metal atom to the farthest atom (hydrogen) from it. Therefore this radius roughly measures the compactness or bulkiness of the complex. The difference between the divalent and trivalent complex

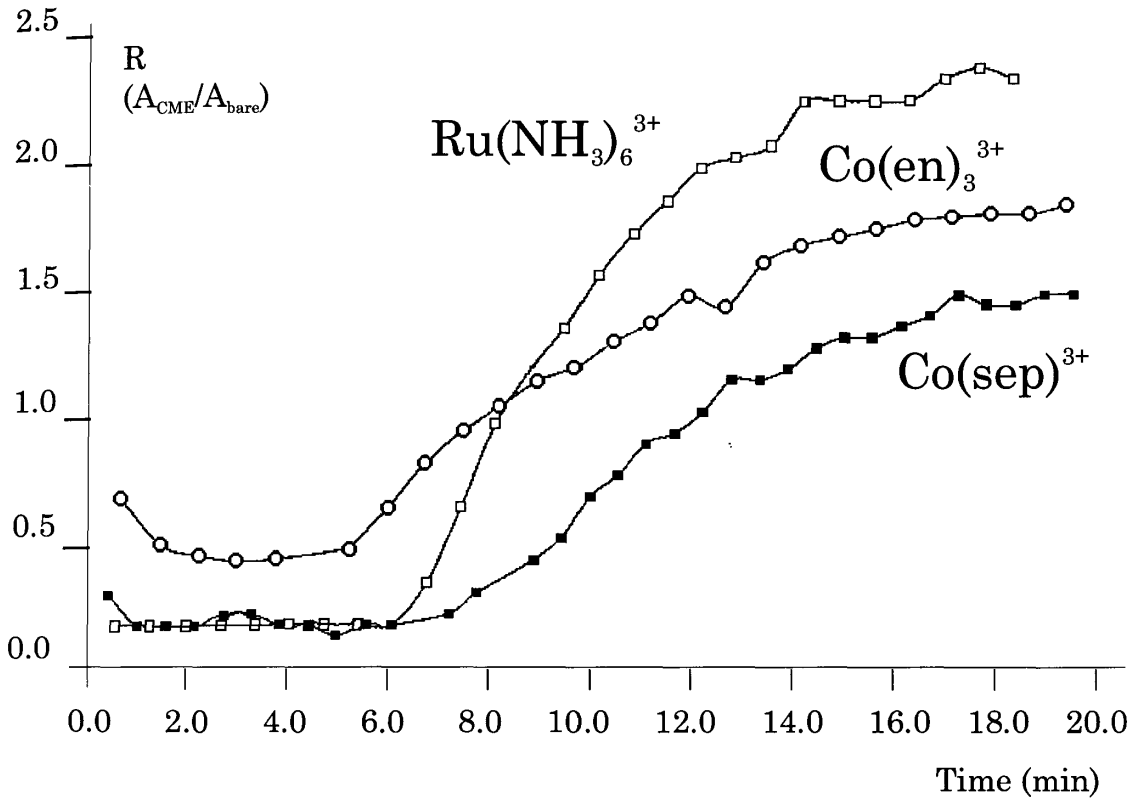

Figure 19. Reduction currents vs. time for $Ru(NH_3)_6^{3+}$, $Co(sep)^{3+}$, and $Co(en)_3^{3+}$ Plot of R vs time is obtained at the clay-modified electrode normalized by the currents at the bare electrode as a function of time.

Table 7. Lattice Minimization vs. Experimental Results.

Complex	r (Å)	total E (kcal/mol)	vdW[a] (kcal/mol)	electrostatic E (kcal/mol)	E3-E2[b]	CEC[c] (meq/g)	ΔE^o (mV)[d]
Mg^{2+}						0.74	
$Co(NH_3)_6^{3+}$	2.5	112.5	-4.58	117.1		0.703	
$Ru(NH_3)_6^{3+}$	2.68	-496.3	-4.7	-491.6	-210	0.840	-25
$Ru(NH_3)_6^{2+}$	2.67	-290	-8.7	-281.3			
$Co(en)_3^{3+}$	3.81	-491.5	-11.7	-479.8	-206	0.304	-10
$Co(en)_3^{2+}$	3.77	-289.0	-15.1	-273.9			
$Co(sep)^{3+}$	3.77	-488.7	-21.7	-467.0	-281	0.078	-35
$Co(sep)^{2+}$	3.77	-201.8	-15.5	-186.3			
$Co(bpy)_3^{3+}$	5.79	-381.7	-30.5	-351.2	-161	0.069	10
$Co(bpy)_3^{2+}$	5.77	-170.9	19.6	-190.5			

a. vdW = van der Waals
b. Differences in calculated electrostatic energy (column 5) between divalent and trivalent complex.
c. CEC = cation exchange capacity (Fitch et al., 1996).
d. ΔE^o is the difference in measured formal potentials (Fitch et al., 1996) for the complex in an aqueous solution and in the clay ($E^o_{soln} - E^o_{clay}$).

with the same metal and ligand is of no importance because we didn't use the quantum mechanically optimized structure for the two different formal charge state of the complex for the lattice minimization. The difference may be the result of the different electrostatic interaction which is mostly affected by the outer-sphere region of the molecule. However, the radius data is still valid when we compare different complexes having either different central metal or different ligands. In general, the larger the computed radius of the compound, the smaller the total energy and the smaller the electrostatic component.

The total energy and electrostatic energy of $Co(NH_3)_6^{3+}$ is inconsistent with other complexes considering its similarity with $Ru(NH_3)_6^{3+}$. It is not even similar to any other cobalt complex. The positive energy value may indicate that $Co(NH_3)_6^{3+}$ is trapped at the local minima which has relatively high repulsive interaction (~112 kcal/mol).

Figure 20 provides a graphical display of these observations. The minimized energy configurations of the compounds are displayed. $Co(sep)^{2+}$ and $Co(sep)^{3+}$ show a significant difference in spatial orientation and the relative distance from the clay surface. The distances between metal atom center and the clay surface are also shown in the caption of Figure 20. The distance does not follow the trend in size of the probe molecule directly. This is not surprising when we consider that the location of the energetically favored minimized probes within the clay interlayer region is not a result of the effect due to their size but a result of the interaction between the probe molecules and the clay due to their structural differences and charge distribution. Also note that

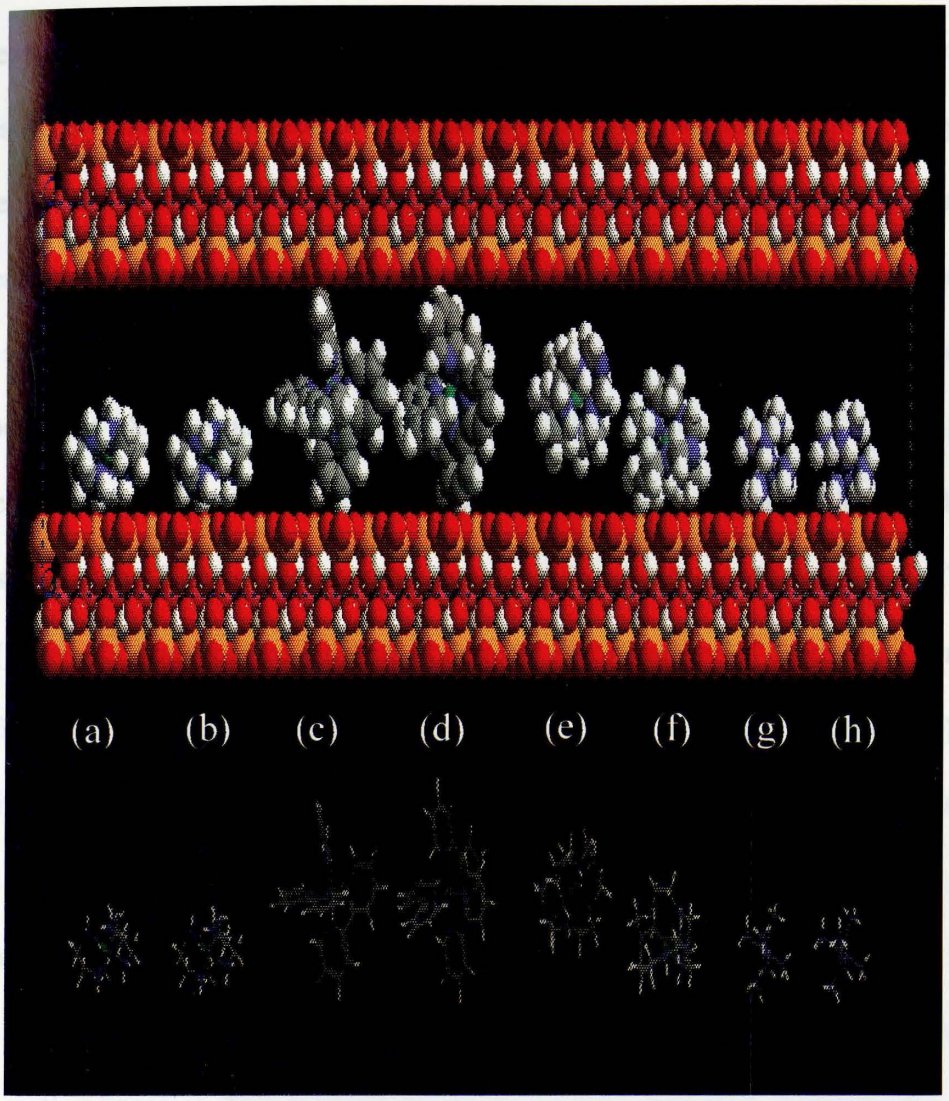

Figure 20. Minimized energy configurations of cationic metal complexes. The minimized structure of each metal complex is shown in clay interlayer region for the graphical display; (a) $Co(en)_3^{2+}$; (b) $Co(en)_3^{3+}$; (c) $Co(bpy)_3^{2+}$; (d) $Co(bpy)_3^{3+}$; (e) $Co(sep)^{2+}$; (f) $Co(sep)^{3+}$; (g) $Ru(NH_3)_6^{2+}$; (h) $Ru(NH_3)_6^{3+}$. The minimized distances between the metal center of the complex and the clay surface are 3.88, 3.80, 6.88, 6.70, 6.71, 4.10, 3.72, 3.61 Å respectively from (a) to (h).

$Co(bpy)_3^{2+}$ and $Co(bpy)_3^{3+}$ do not have as much space as other complexes in the direction perpendicular to the clay surface. Therefore minimization of these complexes most likely involves rotation of molecule instead of translational steps. The specific orientations of the metal complexes such as $Ru(bpy)_3^{2+}$ and $Ru(phen)_3^{2+}$ (phen=1,10-phenanthroline) in terms of the angle between the C_3 symmetry axis of the complex and the z axis (axis perpendicular to the clay surface) were reported from a previous experiment (Abdo et al., 1981) and from a simulation (Sato et al., 1992b), respectively. The minimized structure we obtained for $Co(bpy)_3^{2+}$ showed the angle, ~20° between C_2 axis and z axis. This is a comparable angle previously obtained for $Ru(bpy)_3^{2+}$ and $Ru(phen)_3^{2+}$. Abdo and co-workers obtained 15° for $Ru(bpy)_3^{2+}$ from their X-ray diffraction experiment and Sato and co-workers obtained 25-30° for $Ru(phen)_3^{2+}$ from their simulation. Since we started the lattice minimization where the angle between C_2 and z axis almost 0°, the rotation of the molecule was the major readjustment during the minimization process.

The computed total energies are 100s of kcal/mol, values which exceed realistic interaction energies. This is likely due to the use of a dielectric model for the water in the interlayer. There have been many models which neglect the solvent and treated it as a continuum (Sullivan, et al., 1978; Snook et al., 1979; Sullivan, et al., 1980; Torrie et al., 1988; Aloisi et al., 1989). The electrostatic contributions to enzyme-substrate recognition was studied and showed that the dielectric model had a much greater effect on the absolute magnitude of electrostatic energy than the directionality or relative magnitude of the externally felt electric field (Getzoff et al., 1983).

At large interlayer distances (> 20 Å), the interaction with the clay is well described by the DLVO theory (Derjaguin and Landau, 1941; Verwey and Overbeek, 1948) treating clay structures as suspensions. However, this continuum theory fails at smaller interlayer distances, where we should treat the system at the molecular level.

In general, the properties of a solvent at liquid-solid interface are different from those of the bulk liquid. An earlier experiment showed that this structural difference of the confined liquid leads to layering near the solid surface due to the interaction between two different phases (Israelachvili, 1985). Many computer simulations also confirmed this layering effect of liquid near the clay surface (Karaborni et al., 1996; Boek et al., 1995; Delville et al., 1993; Delville, 1992). Therefore we should treat solvent (water) explicitly at the molecular level to model the clay-water-cationic complex interactions within the interlayer region.

The non-continuum effect of water medium was also modeled for the clay simulation by using a distance dependent dielectric constant (Sato et al., 1992) according to the preceding literature concerning with the binding of a protein and DNA (Jayaran and Beveridge, 1990). However, this shielded dielectric treatment still does not describe the clay-solvent-complex interactions at the molecular level.

Similar high energy value of the clay -cation-hydrated complexes was obtained and the trends of the energy value were used in the earlier computation for the adsorption of nucleotides on bentonite clays (Liebmann et al., 1982). Some realistic bonding energies (~10s of kcal) were found from the earlier simulations. They either used the Lennard-Jones potential alone without considering the coulombic interaction or

used the distance dependent dielectric constant to consider the water layers as shielded barriers (Sato et al., 1992a; Sato et al., 1992b). By doing this, the electrostatic interaction was significantly decreased and the total energy was mostly described in terms of the van der Waals interaction.

We chose the continuum model as there has been some debate over the nature of the dielectric constant near the clay charged surface. Consequently, in all subsequent discussions focus will be on ***trends*** in energies across the class of compounds as opposed to comparisons of individual energies with measured values.

The equilibrium measured interaction of these compounds with the clay contains other energetic components such as ion-ion pairing, probe-probe pairing, probe-clay hydrogen bonding, and hydrophobic driving forces. Consequently, it is not surprising that the computed trends in energy do not follow the trends in the measured adsorption of these complexes. The measured values (Fitch et al., 1996) for equilibrium adsorption are also given in Table 7 in the column labeled cation exchange capacity, CEC (meq/g). This number represents the displaceable amount of the complex. CEC includes adsorbate-adsorbate interaction which is not considered for our simulation where the single cationic complex is located at the clay interlayer region. For Mg^{2+}, saturation of the clay with the ion and subsequent removal results in a displaceable Mg^{2+} ion content of 0.74 meq/g, the reference cation exchange capacity of the clay. The ions $Ru(NH_3)_6^{3+}$ and $Co(NH_3)_6^{3+}$ are completely exchangeable, indicating that the mechanism of retention of these ions at equilibrium is similar to that of the simple monatomic cations. While the remaining three cations would be predicted, based on an electrostatic

computational model, to have equivalent or higher exchangeability with lower interaction energies, the equilibrium experimental data shows that the extent of retention increases with ion size. This indicates that the equilibrium mode of retention is not electrostatic in nature, but is driven by the other factors mentioned: ion-ion pairing, probe-probe pairing, probe-clay hydrogen bonding, and hydrophobic driving forces (see Figure 21).

This might suggest that computations based on a single molecule approaching the clay surface in a dielectric continuum model shed little light on real world processes. This is true if we confine our attention to equilibrium processes. If we look at non-equilibrium data one finds that the computational model accurately predicts the behavior of these probes. Consider a probe molecule that has been trapped in the electric field of the clay. It can continue to travel within the electric field in response to a diffusion gradient across the clay, or it can come to equilibrium with the clay surface. In Figure 21, this would be a transfer from the channel to a pocket. The rate of equilibration will be determined in part by the microscopic details of it's molecular structure. Thus, if the clay film is small enough, and the rate of equilibration is slow enough, the measured flux of the probe across the film will depend upon the electrostatic component of the interaction of the probe molecule with the clay surface.

Under such non-equilibrium conditions, the reduction/oxidation potentials will be perturbed by the variable interaction of the trivalent and divalent species with the electric field of the clay. The difference between the potential measured under solution conditions (E^{o}_{soln}) and that obtained under non-equilibrium conditions in the clay (E^{o}_{clay})

Figure 21. Energy well to illustrate the delocalized electric field driven energy channel and adsorbate-adsorbate driven energy well at a clay surface.
The transport within in clay films depends strongly on the degree of loading of the clay. These points are illustrated in this Figure. The clay surface can have specific adsorption sites, the energetics of which depend upon co-adsorbates. At further distances from the surface a delocalized electric field weakly retains cationic solutes. The equilibrium state for an intercalated cation may be in such an adsorbate-adsorbate well. Consequently, transport occurring under non-equilibrium conditions will be significantly different than transport occurring under equilibrium conditions.

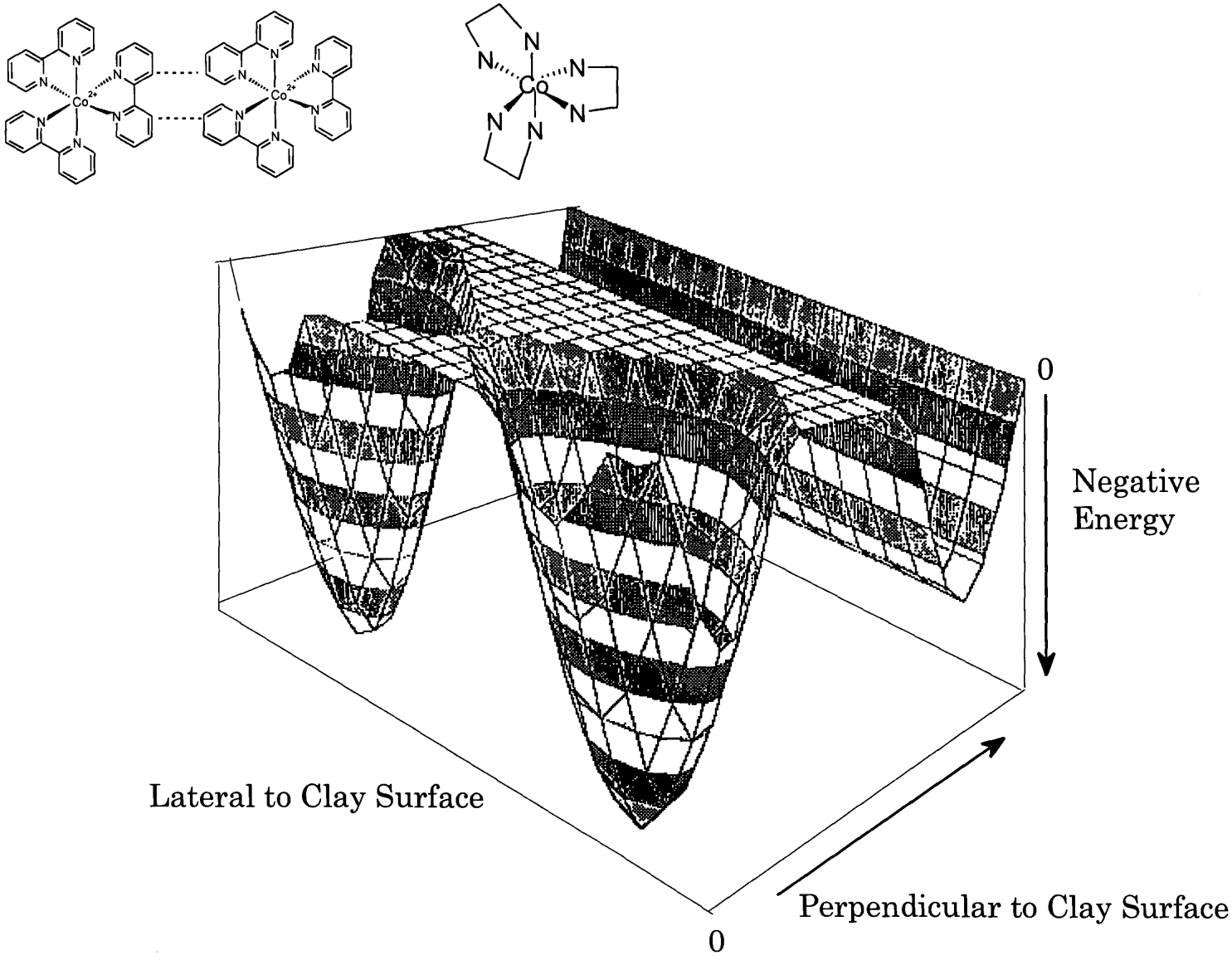
0
Negative
Energy
Lateral to Clay Surface
Perpendicular to Clay Surface
0

is shown in Table 7 (page 123; shown as ΔE^o value in mV). For the electrochemical signal associated with the reduction of the complexes, overall reaction is:

[54] $$OxX_3 + e^- + Na^+ \rightarrow RedX_2 + NaX$$

We can write out the equations for the reduced species and oxidized species:

[55] $$Red + 2NaX \xrightarrow{K_{II}} RedX_2 + 2Na^+ \qquad K_{II} = \frac{[RedX_2][Na^+]^2}{[Red][NaX]^2}$$

[56] $$Ox + 3NaX \xrightarrow{K_{III}} OxX_3 + 3Na^+ \qquad K_{III} = \frac{[OxX_3][Na^+]^3}{[Ox][NaX]^3}$$

where $RedX_2$ is the clay (X) associated reduced (Red) species, OxX_3 is the clay associated oxidized (Ox) species, NaX is the sodium filled clay sites, K_{III} is the equilibrium constant associated with the exchange of the trivalent species with sodium saturated clay, and K_{II} is the equilibrium constant associated with the exchange of the divalent species with the sodium saturated clay. The following relation is obtained from the equilibrium constants (eq 55 and 56) for the reduced species and oxidized species:

[57] $$\frac{[Red]}{[Ox]} = \frac{K_{III}[RedX_2][NaX]}{K_{II}[OxX_3][Na^+]}$$

The general form of the Nernst equation is:

[58] $$E = E^o_{so\ln} - \frac{RT}{nF}\ln\frac{[Red]}{[Ox]}$$

where R is the natural gas constant, T is the temperature, n is the number of electrons involved in the oxidation reduction process, F is the Faraday's constant. Eq 58 can be rewritten by substituting the concentration ratio between reduced species and oxidized species obtained in eq 57(Fitch, 1990; Naegeli et al., 1986).

[59] $$E = E^{o}_{so\ln} - \frac{RT}{nF}\ln\frac{K_{III}}{K_{II}} - \frac{RT}{nF}\ln\frac{[NaX]}{[Na^{+}]} - \frac{RT}{nF}\ln\frac{[RedX_2]}{[OxX_3]}$$

When we consider a half-reaction for the reduction of the oxidized species within the clay,

[60] $$OxX_3 + e^{-} \longrightarrow RedX_2$$

the Nernst equation for this reduction (eq 60) is written as:

[61] $$E = E^{o}_{CME} - \frac{RT}{nF}\ln\frac{[RedX_2]}{[OxX_3]}$$

By comparing eq 59 and eq 61, the formal potential for the exchange process in the clay is given by the first three terms in the right hand side of eq 59:

[62] $$E^{o}_{CME} = E^{o}_{so\ln} - \frac{RT}{nF}\ln\frac{K_{III}}{K_{II}} - \frac{RT}{nF}\ln\frac{[NaX]}{[Na^{+}]}$$

If the number of exchange sites occupied by sodium are constant, as might be expected to occur just as the clay is filling or as the clay has reached nearly full saturation, and if the concentration of sodium in the bathing solution is constant, then:

[63] $$\Delta E^{o}_{complex} = E^{o}_{so\ln} - E^{o}_{CME} = \frac{RT}{nF}\ln\frac{K_{III}}{K_{II}} + const.$$

or:

[64] $$nF\Delta E^{o}_{complex} = RT\ln K_{III} - RT\ln K_{II} + const.$$

Eq 64 can be rewritten in terms of Gibbs free energy (G) using following relationships:

[65] $$\Delta G^{rxn} = -RT\ln K^{rxn} = \Sigma G_{reactants} - \Sigma G_{products}$$

[66] $$\Delta G = -nFE$$

[67] $$\Delta\Delta G = \Delta G_{III}^{rxn} - \Delta G_{II}^{rxn} = -RT\ln K_{III}^{rxn} - (-RT\ln K_{II}^{rxn})$$

$$= \{G_{III} - (G_{clay} + G_{3+})\} - \{G_{II} - (G_{clay} + G_{2+})\}$$

$$= (G_{III} - G_{3+}) - (G_{II} - G_{2+})$$

where G values are the free energy of the trivalent species and divalent species, and the subscripts II and III denote the total energy values for the divalent and trivalent complex with the clay. Subscripts 2+ and 3+ denote the total energy values of divalent and trivalent complex alone without the clay. The larger the association of the trivalent species with the clay surface as compared to the divalent species, the larger the shift negative in potential. We can use the difference in the minimized energies $\{(E_{III}-E_{3+}) - (E_{II} - E_{2+})\}$ as a measure of ΔG. As a result, eq 67 predicts that reduction potential shift should be proportional to the difference in minimized energies.

Table 7 and Figure 22 show the experimental potential shifts and the differences in minimized energy values. A very nice agreement in the general trend is found. An increase in the difference in relative electrostatic energies is followed by an increase in the relative difference in measured potential shifts. This data shows a very nice predictive pattern between computational studies of cationic probe molecules in an electric field and the electrochemical measurements associated with the reduction/oxidation of those probes.

There is no trend in E^{o} with radii or with change in radii (Table 7). This may be due to the fact that we did not use a quantum mechanically optimized. There is also no trend with respect to radii across molecular species. This suggests that non-equilibrium

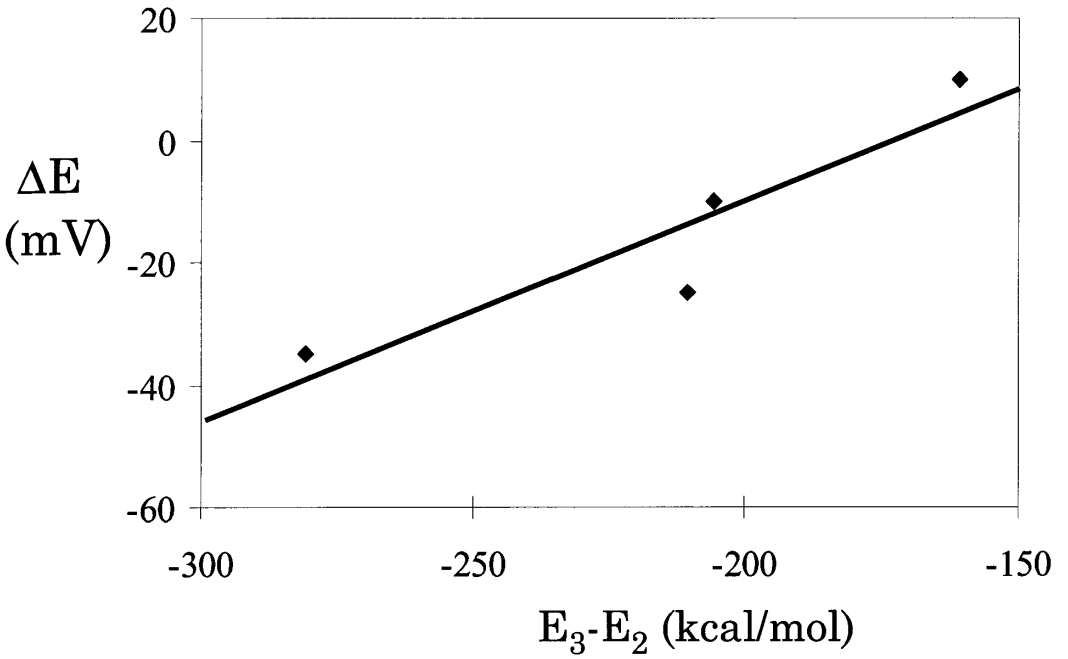

Figure 22. Measured ΔE vs. calculated ΔΔG

effects between the probe and the planar charged surface is affected not just by overall valence and size but by the distribution of partial charge throughout the molecule. This point is well illustrated by noting the variable distribution of charge in $Co(sep)^{2+}$ and $Co(sep)^{3+}$ in the trivalent and divalent states (Table 5). In the trivalent state the metal ion has a less positive charge density relative to the metal atom in the divalent complex. Furthermore, 12 carbon atoms (Table 5) are differently charged based on the overall valency of the compound. Charge is distributed back to four of the 8 nitrogen atoms in both complexes. However nitrogens 8 and 9, the exposed nitrogens, are more heavily negatively charged in the divalent complex than in the trivalent. It may be this different distribution of charge that affects the relative charge stability of this compound in the clay (E_3-E_2) instead of volume changes (there are none as the radius is constant) or overall charge changes.

3. Molecular Dynamics to Account for the Observed Transport in CME

a. Statistical Analysis

The statistical analysis of the trajectory of each dynamics simulation is shown in Figure 23. All of the energy plots shown here are the time dependent running average. The corresponding energy values were accumulated over time and the calculated averages were plotted against time. The absolute value of these energies or the relative magnitude of the energy differences between diffusing chemical probes will not give the information of the diffusional transport characteristics. However, the energetics of diffusing probes within the simulation cell over the dynamics run time were shown and this can be used to understand the interaction energy between particles, bonds, angles,

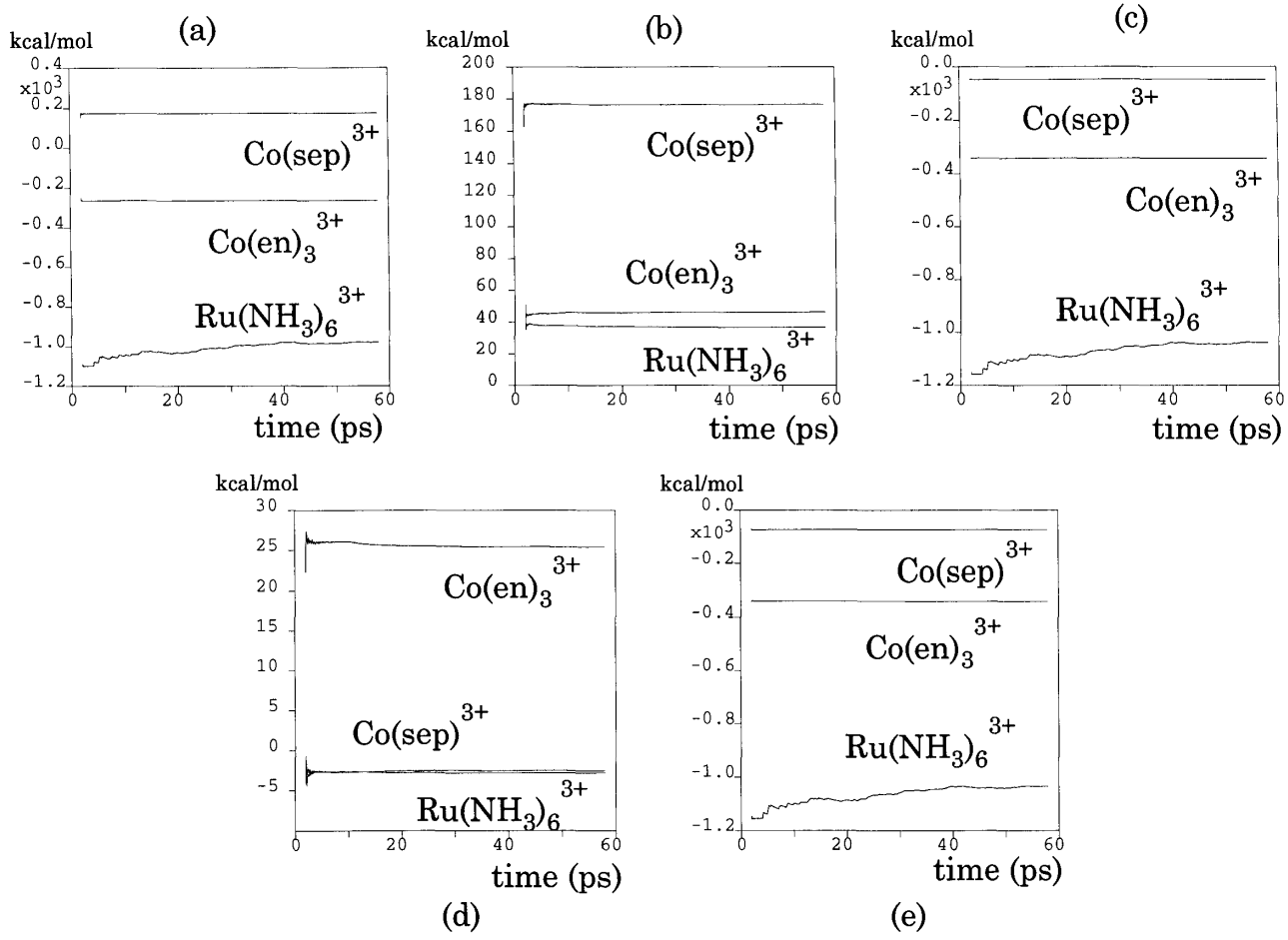

Figure 23. Statistical Analysis for Molecular Dynamics Simulations for Metal Complexes.
(a) Total Energy; (b)Valence Energy; (c) Non-bond Energy; (d) vdW Energy; (e) Electrostatistic Energy

and so on under the influence of valence forcefield, van der Waals, and electrostatics. For example, one general trend is that $Ru(NH_3)_6^{3+}$ is the lowest in energy throughout the dynamics run in all of five energy properties shown. The attractive coulombic electrostatic interaction of $Ru(NH_3)_6^{3+}$ is particularly strong compared to $Co(sep)^{3+}$ or $Co(en)_3^{3+}$. Also notice that the change of the calculated nonbonding energy, as well as electrostatic energy, of $Ru(NH_3)_6^{3+}$ over time is noticeable. That of $Co(sep)^{3+}$ and $Co(en)_3^{3+}$ are not. Further investigation of this behavior should be done because it can give the information of the diffusional behavior of the molecule. The differential of the energy with respect to time can give the displacement, velocity, and acceleration which is directly related to diffusion.

b. Displacement Analysis

As mentioned earlier, the energy profile of the system with time itself doesn't supply the explanation of the diffusional behavior. One useful value of molecular dynamics to study the diffusional behavior is the mean square displacement (MSD):

[68] $$MSD = \frac{1}{n}\sum_{i=1}^{n}\frac{1}{s}\sum_{j=1}^{s}\left|r_i(t_j) - \langle r_i \rangle\right|^2$$

where r_i is the position of *i*th atom, t_j the *j*th time step, *s* the total time of dynamics simulations for analysis, and *n* the total number of atoms in the molecule.

The solution to the diffusion equation indicates that the displacement along an x, y or z axis from the origin follows a Gaussian distribution. The second moment of this Gaussian, is the mean square displacement (MSD or variance) and is related to the self diffusion equation via the Einstein relationship (Haile, 1992; Müller-Plathe et al., 1993).

[69] $MSD = 2dDt$

where d is the number of spatial dimensions (i.e. 3 for 3 dimensional space). This relationship has been found to depend upon the density of the system explored. When the density of the system investigated is low, quadratic dependencies on time can develop in the initial phase of simulation. Although the initial quadratic dependency is not very well shown in Figure 24 (maybe found at very early stage of the MD; 1ps or so), the appropriate correlation of MSD with D has been considered at sufficiently longer times (>4 ps) to exclude any possible quadratic dependency at the very early stage of the simulation. In addition, it is necessary to have non-periodic boundary conditions within the simulation (Dünweg et al., 1993; Magda et al., 1983).

Mean square displacements (MSD) of the probe molecules are shown in Figure 24. The isotropic mean square displacement (MSD) is denoted by $<D^2>$. The anisotropic components of MSD are shown as $<x^2>$, $<y^2>$, and $<z^2>$. Among these $<z^2>$ is the displacement which is perpendicular to the clay surface and the other two are for the motion parallel to the clay surface. For all compounds shown in Figure 24, there is a steep initial slope (< 4ps; quadratic dependencies) for all directions of motion. Most displacement is made in x and y direction which is parallel to the clay surface. The graphical data following this steep initial slope (4 ~ 15 ps) also shows that the diffusional motion mostly occurs parallel to the clay surface.

In the case of $Ru(NH_3)_6^{3+}$, MSD plot shows leveling off after 20 ps of dynamics simulation time. This may indicate the trajectory taken over this time period was at the

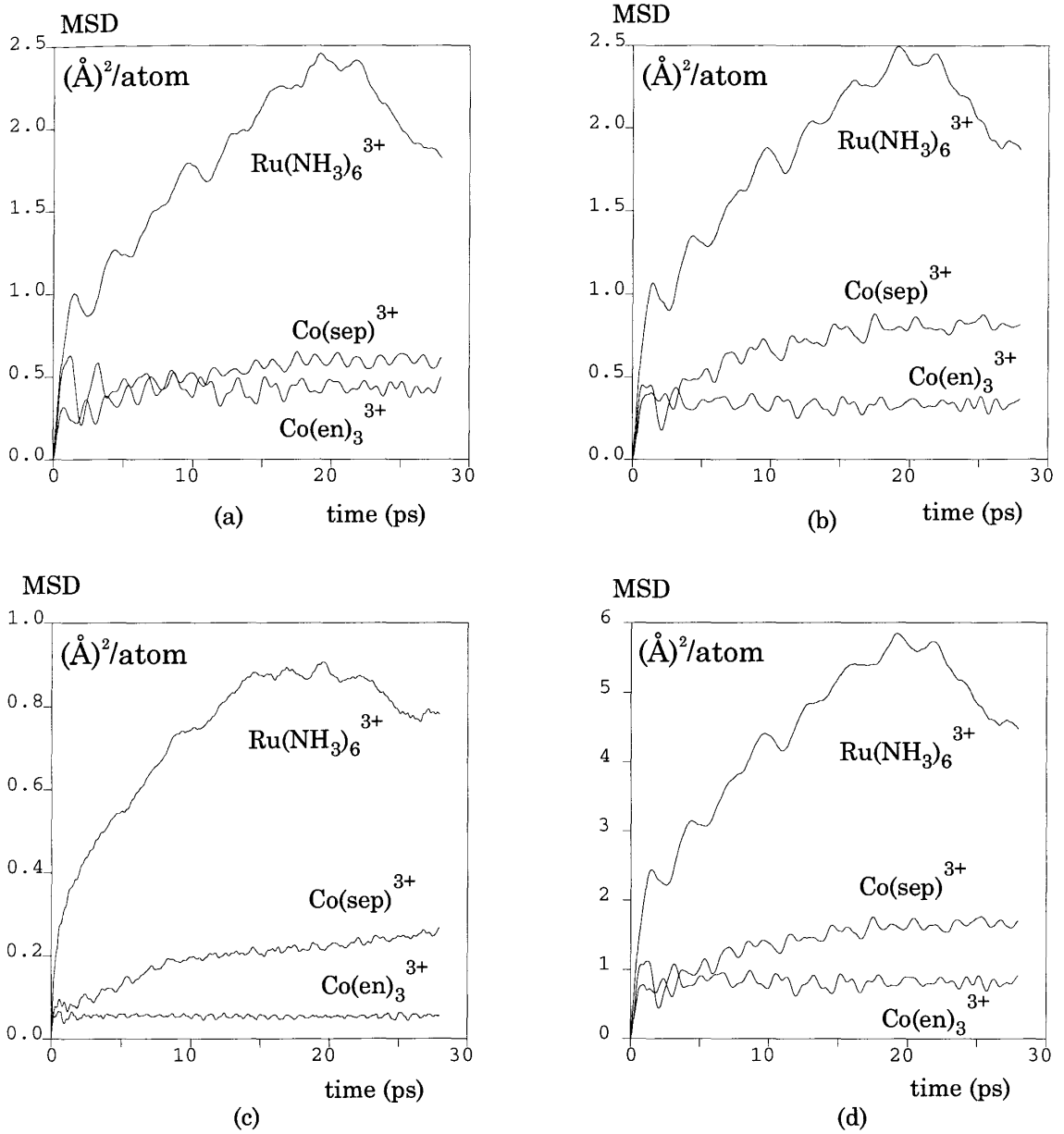

Figure 24. Mean Square Displacement (MSD) Analysis.
(a) MSD in x direction; $\langle x^2 \rangle$; (b) MSD in y direction; $\langle y^2 \rangle$
(c) MSD in z direction; $\langle z^2 \rangle$; (d) MSD total; $\langle D^2 \rangle$.

local minimum or trapped. However, complete statistical treatment to relate MSD to the motion within the clay domain is still valid assuming the leveling off does not go to an extreme. Molecular dynamics simulation for a longer period of time for this purpose may solve this problem.

MSD plots have been previously related to measurements of diffusion by macroscopic experiments (Catlow et al., 1995). It is interesting to note that the diffusional motion represented by relative magnitude of $<x^2>$ and $<y^2>$ is in the order $Ru(NH_3)_6^{3+}>Co(sep)^{3+}\sim Co(en)_3^{3+}$. This order is observed experimentally (Figure 19, p.122). $Ru(NH_3)_6^{3+}$ shows the greatest linear increase after the time lag.

C. Motion of Cobalt (II) Complexes Containing 2,2´-Bipyridine, 2,2´-Bipyrazine, and 2,2´-Bipyrimidine Ligands in Montmorillonite

1. Introduction

In the previous section, the differences in the diffusional transport of cationic compounds, $Co(sep)^{3+}$, $Ru(NH_3)_6^{3+}$, $Co(en)_3^{3+}$, $Co(NH_3)_6^{3+}$, and $Co(bpy)_3^{3+}$ observed from the cyclic voltammetry are attributed to their molecular differences. Molecular dynamics simulation of these cationic compounds in the clay interlayer region was then applied to show that the differences in the diffusional behavior of these probes are attributed to their structural differences and charge distribution.

This time, cobalt complexes, $Co(bpy)_3^{2+}$, $Co(bpm)_3^{2+}$, and $Co(bpz)_3^{2+}$ are considered for the motional study in the clay montmorillonite.

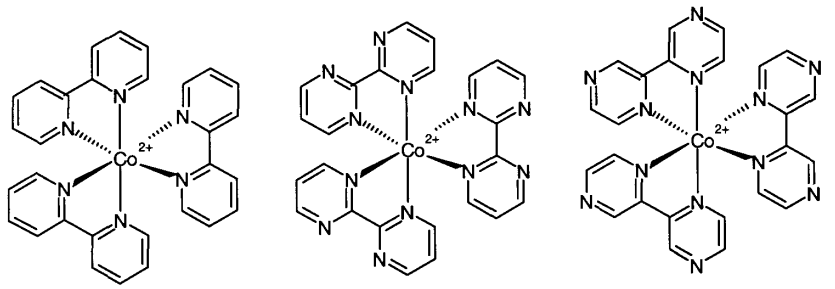

Figure 25. Structure of cobalt(II) complexes containing bpy, bpm, and bpz.

The study of these probes may be able to give more information about the role of charge distribution of the molecule in clay diffusion. They are all divalent species having formal charge of 2+. They are also structurally very similar as shown in Figure 25. Moreover, they are electronically isoelectric (having same number of electrons; 271 electrons). Therefore, the greatest differences of these cobalt complexes should be attributed to their different charge distribution throughout the molecule due to either lack ($Co(bpy)_3^{2+}$) or different location ($Co(bpm)_3^{2+}$ and $Co(bpz)_3^{2+}$) of the nitrogens which are not coordinated to the metal center.

2. *Spectroscopic Determination of Adsorption*

UV/VIS spectra of aqueous solution of cobalt(II) complexes showed strong absorption in the UV region and weak absorption in visible region. As explained in Methods, our sample includes the unbound amount of metal complex after clay-complex formation. Therefore, the high absorption peak in UV range indicates that the clay-metal complex binding effect is low and vice versa. Using the unbound amount of the complex and the molarity of the species, the adsorption amount of cobalt complex

on the clay *vs.* the equilibrium concentration in liquid phase is plotted and shown in Figure 26. The order of adsorption ability of cobalt complexes, $Co(bpy)_3^{2+}$ > $Co(bpm)_3^{2+}$ > $Co(bpz)_3^{2+}$ was obtained.

3. *Cyclic Voltammetric Diffusion Monitoring*

The transport of the cobalt complexes was monitored with multi-sweep cyclic voltammetry (MSCV). The results are shown in Figure 27. The cathodic peak currents develop in the order of $Co(bpz)_3^{2+}$ > $Co(bpm)_3^{2+}$ > $Co(bpy)_3^{2+}$ for the earlier stage (5~10 minutes) of the diffusion through the clay medium monitored by CME. The extent of SWy-1montmorillonite clay film swelling is known to be controlled by the Na^+ ion concentration from the earlier study (Fitch, 1992). The diffusion monitored by the clay-modified electrode with more swollen clay film (which has NaCl concentration of 0.01M instead of 0.1M) showed more rapid increase of the peak development both for $Co(bpm)_3^{2+}$ and $Co(bpy)_3^{2+}$. The increased interlayer spacing as a result of greater swelling may accommodate more electroactive species into the channel, therefore the total flux arriving near to the electrode surface is increased.

4. Molecular Dynamics Simulations

a. Statistical Analysis

The statistical analysis of the trajectory of each dynamics simulation is shown in Figure 28. All of the energy plots shown here are the time dependent running average as used for the previous study earlier in this Chapter. The energetics of diffusing probes within the simulation cell over the dynamics run time were shown to describe the interaction energy between particles, bonds, angles, and so on under the influence of all

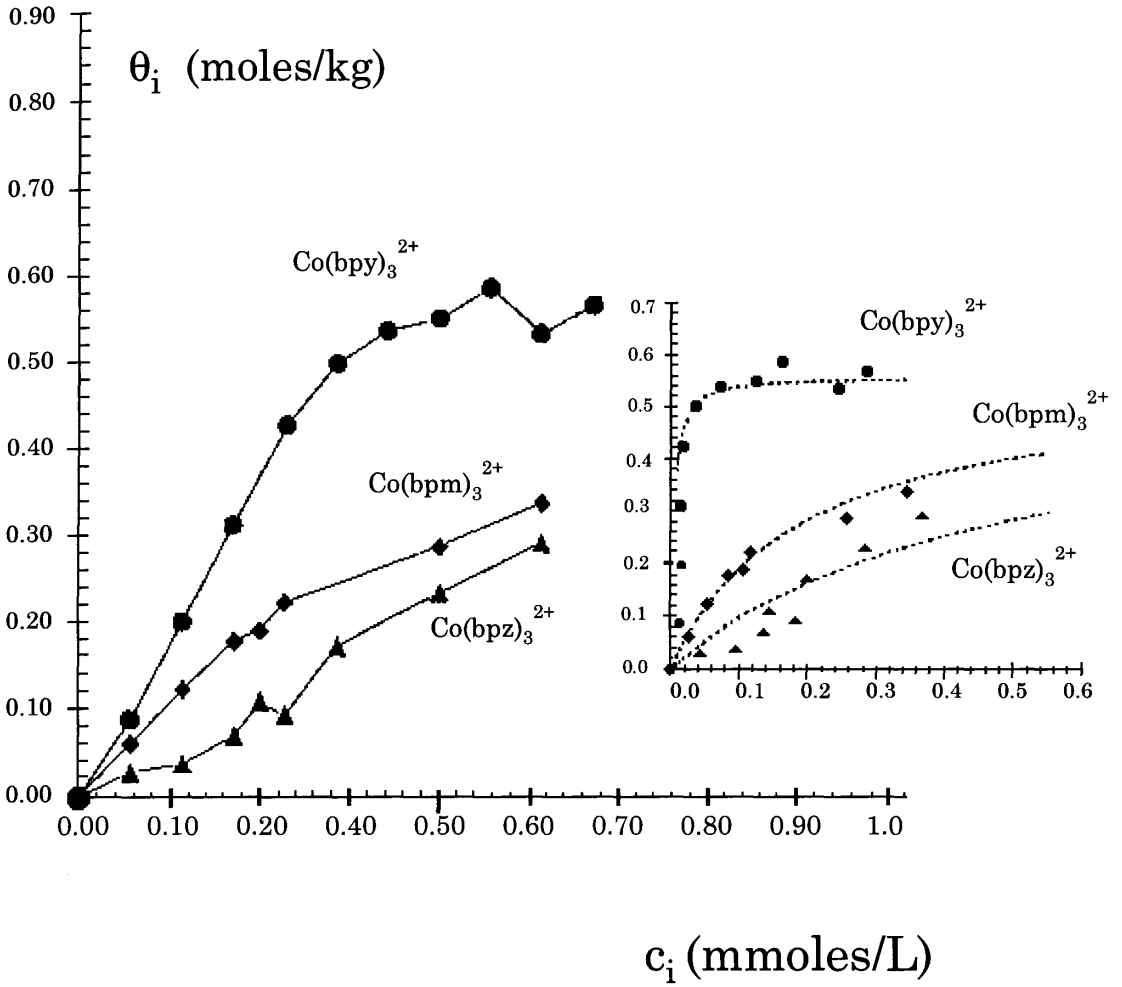

Figure 26. Adsorption of Cobalt Complexes.
Adsorption of $Co(bpy)_3^{2+}$ (circle), $Co(bpm)_3^{2+}$ (diamond), and $Co(bpz)_3^{2+}$ (triangle) on the clay. The amount of 350 μg of clay was used. The dotted lines in the insertion are calculated results by Langmuir isotherm.

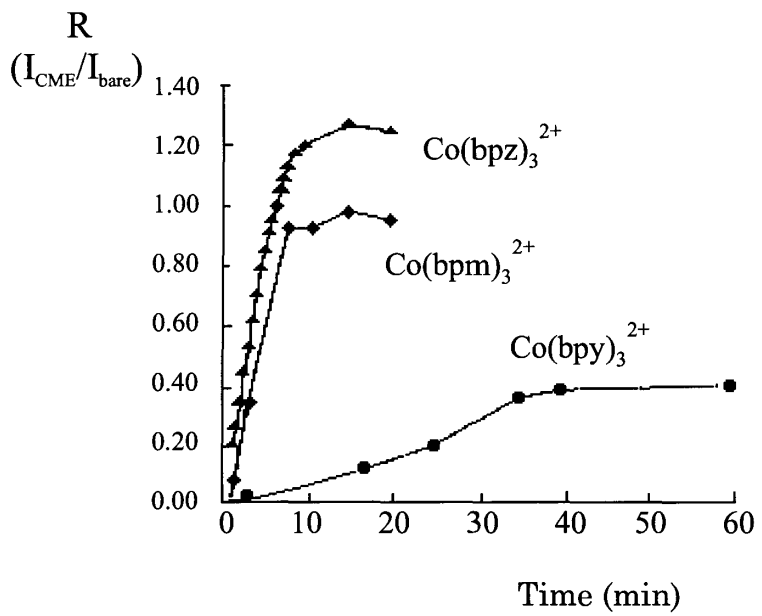

Figure 27. Reduction currents vs. time for $Co(bpy)_3^{2+}$, $Co(bpm)_3^{2+}$, and $Co(bpz)_3^{2+}$ 1.5 mM of each cobalt complex in aqueous solution with 0.01 M NaCl as supporting electrolyte used. Scan rate of 100 mV/s was used. Glassy carbon working electrode and AgCl/Ag reference electrode were used.

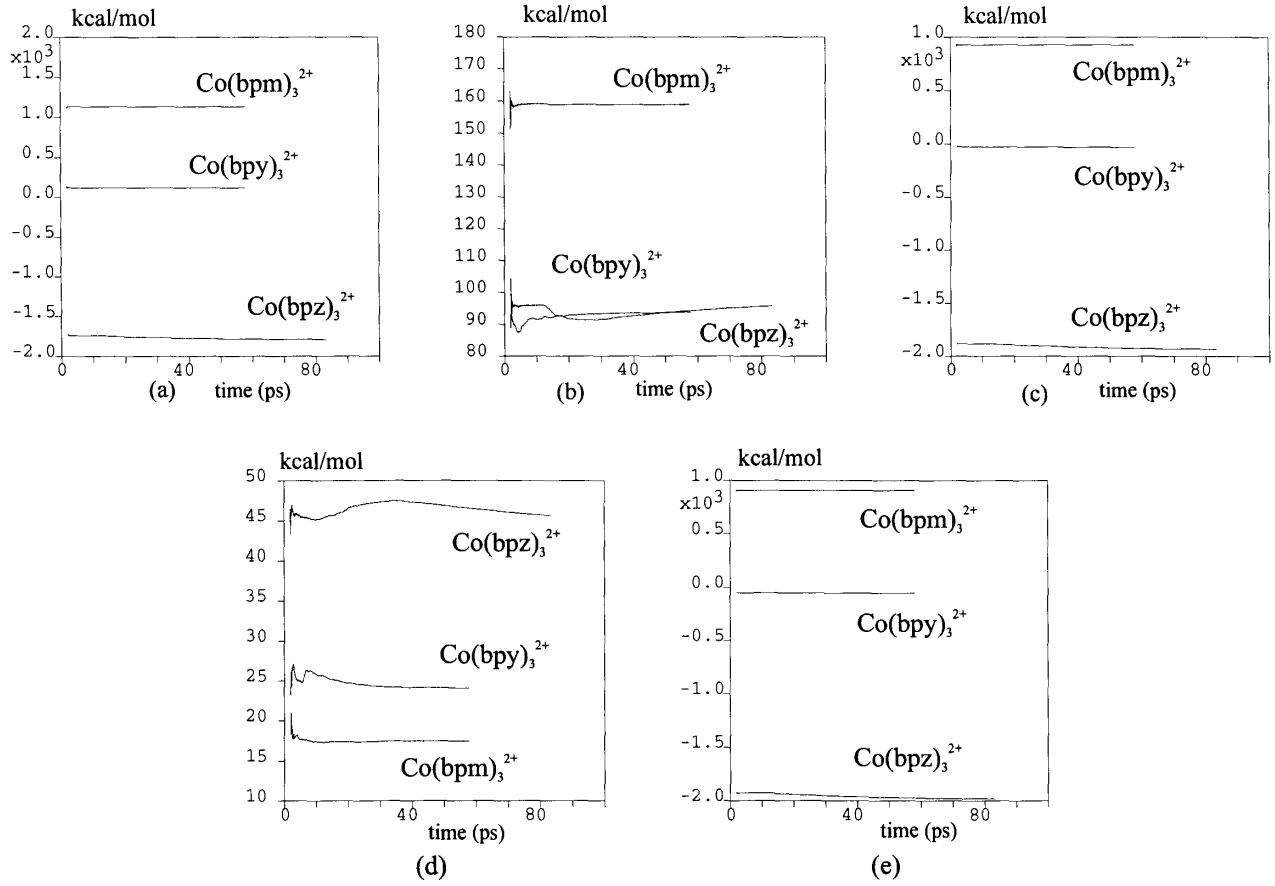

Figure 28. Statistical Analysis for MD for $Co(bpy)_3^{2+}$, $Co(bpm)_3^{2+}$, and $Co(bpz)_3^{2+}$.
(a) Total Energy; (b) Valence Energy; (c) Non-bond Energy; (d) vdW; (e) Electrostatic Energy.

forcefields and charge. Notice the general trends where the $Co(bpz)_3^{2+}$ containing system is the lowest in energy throughout the dynamics run in all of five energy profiles shown. Here again, the computed total energies are 100s of kcal/mol, values which exceed realistic interaction energies due to the use of dielectric continuum approximation previously discussed.

b. Displacement Analysis

The mean square displacement of the probe molecules is shown in Figure 29. The isotropic mean square displacement (MSD) denoted by $<D^2>$ were shown with 3 different anisotropic components of MSD, $<x^2>$, $<y^2>$, and $<z^2>$. Among these $<z^2>$ is the displacement which is perpendicular to the clay surface and the other two are for the motion parallel to the clay surface. The trajectory of last 5 ps data out of the 10 ps simulation has been used. Notice the y-axes of all graphs. Most displacement is made in x and y direction which is parallel to the clay surface. Therefore, the diffusional motion mostly occurs parallel to the clay surface.

The diffusional motion represented by the relative magnitude of $<x^2>$ and $<y^2>$ is in the order $Co(bpz)_3^{2+} > Co(bpm)_3^{2+} > Co(bpy)_3^{2+}$. The same order was observed experimentally from CME where $Co(bpz)_3^{2+}$ shows the greatest development of peak current over time (Figure 27). It is also directly opposite of the adsorption order obtained from UV Spectroscopy, that is, the compound least adsorbed at equilibrium showed greater motion.

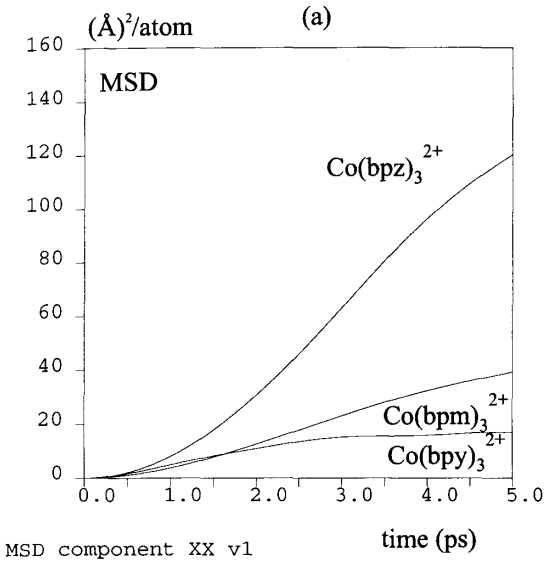

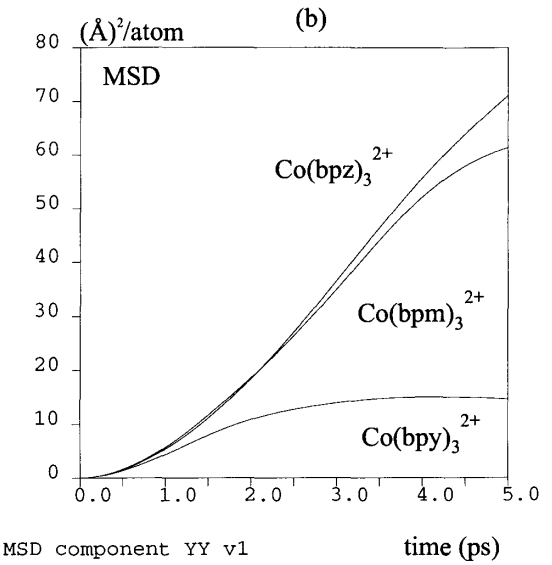

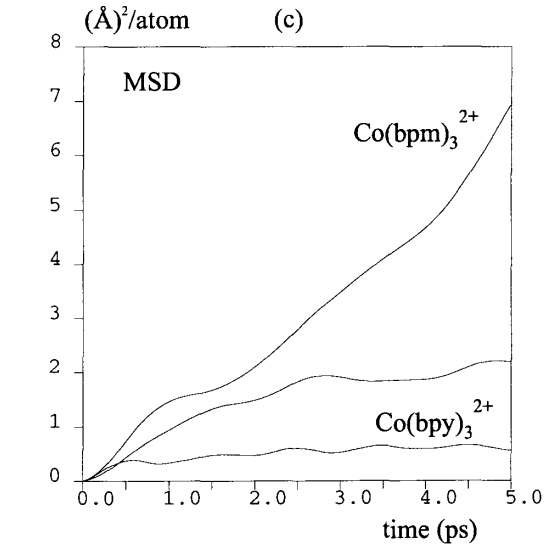

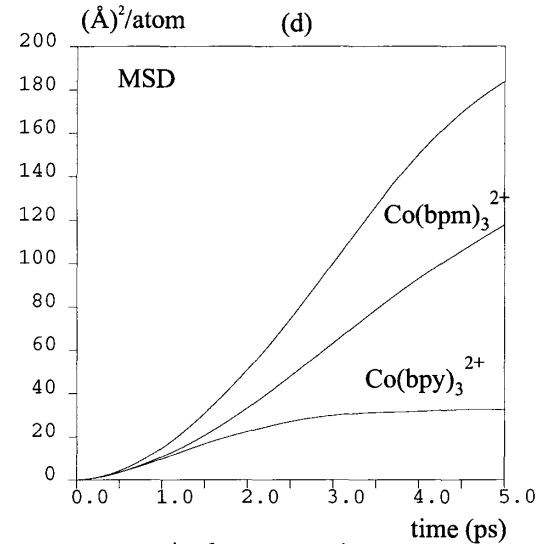

Figure 29. MSD Analysis for $Co(bpy)_3^{2+}$, $Co(bpm)_3^{2+}$, and $Co(bpz)_3^{2+}$.
(a) MSD in x direction; $< x^2 >$; (b) MSD in y direction; $<y^2>$;
(c) MSD in z direction; $<z^2>$; (d) MSD total; $<D^2>$

D. Conclusions

Clay-modified electrodes were used to monitor the activity of electroactive metal complexes through montmorillonite clay. The concept of interlayer spacing controlled by the swelling due to the solvation of interlayer cation was introduced. Some of these interlayer interaction between clay and chemicals were also observed by simple binding experiment of clay suspension using ultraviolet spectroscopy.

Molecular simulations based on quantum mechanical parameterization and forcefield calculations were compared to experiments. Even though we use dielectric medium instead of water content within the clay system, the consistency between the simulation vs. experiment was surprising. Use of the mean square displacement and its slope over time has been used as the main tool to study the diffusional properties of the probe molecules in the clay interlayer system. The author suggests that the use of this simulation technique should be continued to understand the system thoroughly in conjunction with the concurrent clay-modified electrode studies.

Inclusion of water medium may be possible considering recent findings of the water-clay system using Monte-Carlo simulations (Low et al., 1984; Skipper et al., 1989; Skipper et al., 1991; Skipper et al., 1995a; Skipper et al., 1995b; Boek et al., 1995a; Boek et al., 1995b; Delville, 1991; Delville, 1992; Delville, 1993; Delville et al., 1993; Delville, 1995; Karaborni et al., 1996). Simulation with the water, anions, salts, and at least one other probe within the simulation cell will better describe the system.

Chapter VIII.

Study of Ligand Effects in Redox Behavior of Cobalt(II)-Trisbipyridal Complexes: Electrochemical Results vs. Quantum Mechanical Study

A. Introduction

Metal trisbipyridal complexes have been of interest in many reasons. The photochemical properties of a ruthenium(II) tris(bipyrazyl) dication, $Ru(bpz)_3^{2+}$ for use as a photosensitizer in solar energy conversion schemes and $Ru(bpy)_3^{2+}$ as an energy conversion catalyst have been studied by spectroscopy and electrochemistry (Crutchley et al., 1982). They observed the low energy band in the visible region and attributed it to ruthenium's metal-to-ligand charge transfer (MLCT) as Krumholtz did for the similar system (Krumholtz, 1971) previously . The higher energy bands were attributed to π–π^* transition within the ligands, bipyridine or bipyrazine. They reported the cyclic voltammetric experimental results on these compounds and found that both $Ru(bpy)_3^{2+}$ and $Ru(bpz)_3^{2+}$ shows one oxidation and three reductions in acetonitrile (See Table 8 for corresponding electrochemical data). They concluded that the oxidation occurred at the metal center from their ESR study and reduction at the ligands based on positive shift of ligands when coordinated to metal. They could not explain why oxidation occurs at the

Table 8. Electrochemical Data for Bpy, Bpm, Bpz, $Ru(bpy)_3^{2+}$, $Ru(bpm)_3^{2+}$, and $Ru(bpz)_3^{2+}$.

		$E_{1/2}$ (V)[g]			
Reference	Compound	Oxidation	Reduction		
	bpy (5.2)[f]		-2.18[a], -2.20[b]	-2.68[a] (i)[d]	
Ernst[a]	bpm (1.3)[f]		-1.73[a], -1.80[b]	-2.44[a] (i)	
Kawanishi[b]	bpz (0.8)[f]		-1.66[a], -1.76[b]	-2.38[a]	
Crutchley[c]	$Ru(bpy)_3^{2+}$	1.354	-1.332	-1.517	-1.764
	$Ru(bpz)_3^{2+}$	1.86	-0.80	-0.98	-1.24
	$Ru(bpy)_3^{2+}$	1.27	-1.31	-1.50	-1.77
Rillema[d]	$Ru(bpm)_3^{2+}$	1.69	-0.91	-1.08	-1.28
	$Ru(bpz)_3^{2+}$	1.98	-0.68	-0.87	-1.14

a. See ref. (Ernst et al., 1986)
b. See ref. (Kawanishi et al., 1989)
c. See ref. (Crutchley et al., 1982)
d. See ref. (Rillema et al., 1983)
e. (i) denotes irreversible redox processes with peak potentials given.
f. The value in parenthesis denotes pK_a values of the corresponding ligand. See ref. (Rillema et al., 1992)
g. Potentials ($E_{1/2}$) are vs. SCE (saturated calomel electrode)

metal center from their ESR study and reduction at the ligands based on positive shift of ligands when coordinated to metal. That is, the LUMO of the metal/ligand complex was lower in energy than the LUMO of the free ligand. They could not explain why oxidation occurs at the metal or why reduction occurs at the ligands, nor could they explain why they see three reductions from the ligands. They attributed the shift of 0.5 V in the reduction potential of bipyrazyl complex compared to bipyridyl complex to the stabilization of bipyrazyl LUMO π^* orbital by 0.5 V compared to bipyridyl. Another conclusion they made was that the bipyrazyl is not a better π acceptor than bipyridyl due to the lack of strong σ-donor ability which bipyridyl has. This property also may be studied by the molecular orbital calculations.

Quantum mechanical calculations have been done on the iron(II) tris(bipyridyl) complex, $Fe(bpy)_3^{2+}$ (Jung et al., 1983). The calculations treated the metal system with approximations because transition metals require both more sophisticated basis sets and longer calculation time. They reviewed previous calculations (Hanazaki et al., 1969; Sanders, 1972; Roos, 1966) on similar systems and claimed that they described the system more accurately. They compared calculated σ-, π-, and net charge of $Fe(bpy)_3^{2+}$ to other trisdiimine complexes of iron(II) and obtained good results to account for the shift in MLCT between these complexes in electronic spectra. The other ligands of our interest, bipyrazine (bpz), and bipyrimidine (bpm), were not studied.

Further experimental works on $Ru(bpy)_3^{2+}$, $Ru(bpm)_3^{2+}$, and $Ru(bpz)_3^{2+}$ were done by Rillema and co-workers (Rillema et al., 1983). They studied low-energy MLCT

transitions and their shifts depending on the mixture of the ligands in bpy-bpz and bpy-bpm complexes. They also observed one electron oxidations and three electron reductions in acetonitrile from their cyclic voltammetric measurements (Table 8 for $E_{1/2}$ values). They found that the ease of reduction in the complexes is bpz > bpm > bpy which roughly parallels the reduction potential differences of the free ligands. (See Table 8.)

Ruminski and Petersen prepared tris(2,2´-bipyrimidine)cobalt(2+) complex, $Co(bpm)_3^{2+}$, and performed cyclic voltammetric experiments to study its redox behavior (Ruminski et al., 1984). They compared the results with the redox behavior of previously studied $Co(bpy)_3^{2+}$ (Chen et al., 1982). They observed a ~0.7V more positive reduction peak for the Co(III/II) couple as compared to $Co(bpy)_3^{2+}$ and a difference of 1.5 V between the Co(III/II) and Co(II/I) redox couples. They suggested that $Co(bpm)_3^{2+}$ and its derivatives should be studied further for use in storage batteries. In their continued study on bipyrimidine complexes, they also reported spectroscopic results on $Co(bpm)_3^{2+}$ with other metal complexes (Ruminski et al., 1985). They observed red shift[1] for the ligand field bands of $Co(bpm)_3^{2+}$ compared to $Co(bpy)_3^{2+}$.

Coordination characteristics of the ligands bpm and bpz have been studied with their isomeric bidiazine ligands and compared to that of bpy by using Hückel Molecular Orbital Calculations by Ernst and Kaim (Ernst et al., 1986). The LUMO (π^*) energies for the free ligands were reported to be in the order of bpy>bpm>bpz. This is related to

[1] shifted to lower energy (bigger λ value) band.

the reducibility of their electrochemical data as shown in Table 8. That is, the lower π^*, the more added electrons are stabilized, the more the reduction potential shifts positive. They claimed the results from their MO calculation are in good agreement with experimental values. They also used their experimental pK_a values of conjugated acids to compare the σ-donating ability. Their results showed that the pK_a values of ligands are in the order of bpy (4.45) > bpm (1.50) > bpz (0.45). The larger the pK_a value, the weaker the ionization of the complex, implying that negative charge is localized more strongly at the nitrogen group. Consequently, sigma bonding is expected to be greater. They concluded that bpz is a stronger π acceptor than bpy despite its lower lying π^* level (LUMO) because of the weak σ bonding due to its poorest basicity. This synergetic interpretation of "give and take"[1] has been pointed out earlier by Crutchley and Lever (Crutchley et al., 1982). In summary, Ernst and Kaim attempted MO calculation on ligands to account for the coordination by ligands bpy, bpm, bpz, and their isomeric bidiazine ligands.

There is a contradiction regarding the bonding of metal to ligand nitrogens as pointed out by Rillema and co-workers (Rillema, 1992). The contradiction they pointed out was on the basis of the studies mentioned above. According to the electrochemical data both on ligands and ruthenium complexes and the energy of π^* LUMOs from Hückel MO calculations, the bond distances between Ru and N should be Ru-N(bpz) < Ru-N(bpm) < Ru-N(bpy). On the other hand, the pK_a values, or the basicity of the

[1] Here "give" means σ-donating and "take" for π-back-bonding.

ligands, predict Ru-N(bpy) < Ru-N(bpm) < Ru-N(bpz) considering the importance of σ-bonding ability of ligands to the metal, ruthenium. They acquired crystallographic data on these ruthenium complexes. Their results showed that the bond distances between ruthenium and the nitrogen do not follow either of the schemes mentioned above. The actual order of crystallographic measurements of these bond distances is $Ru(bpz)_3^{2+}$ < $Ru(bpy)_3^{2+}$ < $Ru(bpm)_3^{2+}$, which have bond lengths of 2.05, 2.056, and 2.067 Å, respectively. It was suggested that a theoretical evaluation of the degree of σ and π bonding in the complexes was necessary to provide a quantitative understanding of the bonding differences that exist among ruthenium(II) complexes.

Recently, similar electrochemical studies were carried out on cobalt(II) complexes containing same series of tris-ligands, bpy, bpm, and bpz in our lab. The same compounds have been used for the probes of diffusion properties of clay medium. CME and MSCV techniques have been used and molecular dynamics simulations were performed as written in earlier chapters in this study. In the course of the diffusion study, the electrochemistry of cobalt complexes containing these ligands in acetonitrile was studied. We performed the full level of currently available *ab*-initio molecular orbital calculations on $Co(bpm)_3^{2+}$, $Co(bpy)_3^{2+}$, and $Co(bpz)_3^{2+}$ along with calculations on the ligand alone to obtain information on the σ and π bonding of these ligands to cobalt. Also, calculations for the ruthenium complexes were performed to compare with the previous X-ray crystallographic result (Rillema et al., 1992).

B. Methods

Quantum mechanical calculations on the ligands, bpm, bpy, and bpz ligands were carried out with the 3-21G basis sets. The Hartree-Fock calculations were performed with 120 basis functions for bpm and bpz while bpy has 124 basis functions. Total number of shells for bpm and bpz was 48 containing 24 S shells and 24 SP shells while bpy has 52 shells in which 28 S shells and 24 SP shells are used. All three ligands are isoelectric having a total number of 82 electrons. Ligand charge of zero and the spin multiplicity of 1 (singlet) ensured closed shell Hartree-Fock calculations.

Corresponding cobalt (II) complexes were used for *ab*-initio calculations with the same 3-21G basis sets. Single point *ab*-initio calculations without further geometry optimization were performed on each minimized structure. For minimizations, the Universal Force Field (UFF) was used. These divalent metal complexes inherently have one unpaired electron which make the spin multiplicity of 2 (doublet where α and β electrons describe the system). The complete open shell unrestricted Hartree-Fock calculations have been carried out to account for this spin flexibility. In this way α electrons and β electrons will fill up totally independent orbitals which is solely designated corresponding type of either α or β spins.

The divalent ruthenium complexes are already d^6, therefore singlet closed-shell Hartree-Fock calculations have been carried out. Minimization of each ruthenium complex with the Universal Forcefield (UFF) was followed by the single point *ab*-initio calculation with 3-21G basis sets.

Both Mulliken Population Analysis (MPA) and Löwdin Population Analysis (LPA) were performed. Charge calculations were also carried out on these schemes as well as previously used MEP (Molecular Electrostatic Potential). Electronic populations based either on MPA or LPA may give better description on intra-structural characteristics while MEP gives good value for external interactive charge values as previously mentioned in Chapter IV.

Several graphical representations were also prepared to visualize the electronic structure or density of electrons throughout the molecules and ligands as well as to see actual structural shape of the molecular orbitals of interest. These graphical tools should give a clearer understanding of the resulting molecular orbitals in terms of their relative shapes and characteristics.

C. Results and Discussion

1. Electrochemical data

The cyclic voltammograms of $Co(bpm)_3^{2+}$, $Co(bpy)_3^{2+}$, and $Co(bpz)_3^{2+}$ were recorded in acetonitrile. The oxidation peak of each complex is reversible and relatively well consistent with the previous results (Ruminski et al., 1984; Ruminski et al., 1985). Figure 30 shows a nice reversible peak for the oxidation of $Co(bpm)_3^{2+}$ while at the same time showing an irreversible reduction peak. The oxidation and reduction potentials of all complexes are tabulated in Table 9. The reducibility order of bpz > bpm > bpy follows the same trend as that of free ligands (see Table 8).

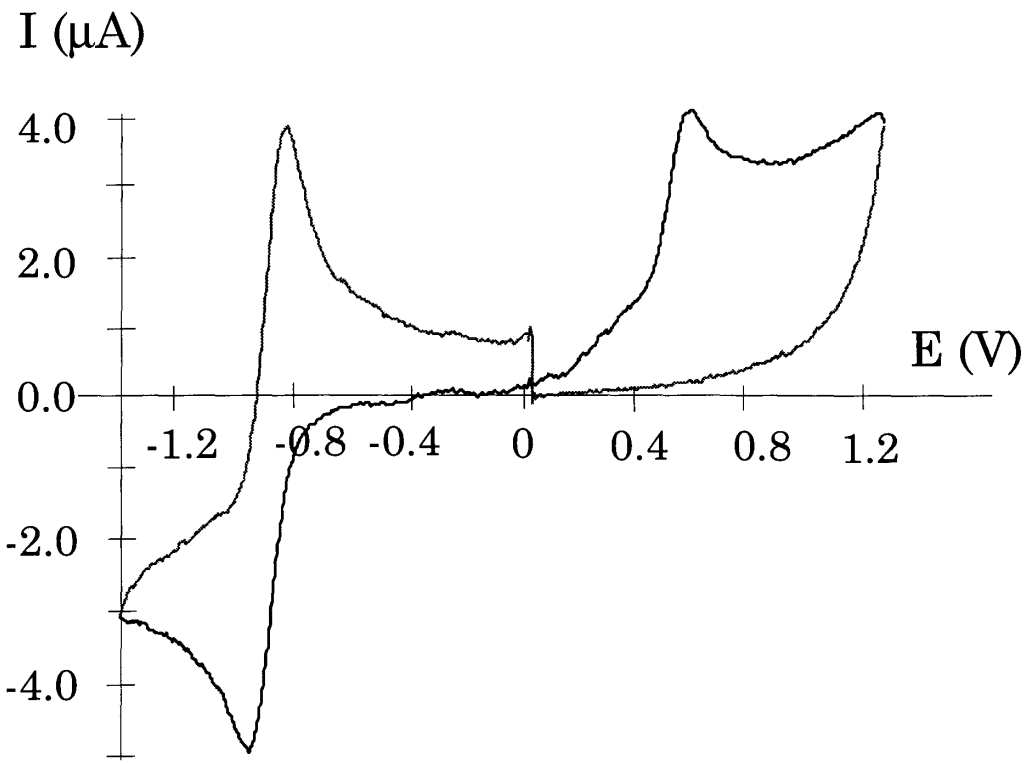

Figure 30. Cyclic Voltammogram of $Co(bpm)_3^{2+}$.
1.5 mM $Co(bpm)_3^{2+}$, scan rate 200 mV/sec, glassy carbon working electrode, Ag/AgCl reference electrode and 10 mM TBATFB used. Acetonitrile was used for non-aqueous system.

Table 9. Electrochemical Data for CoL_3^{2+} (L = bpy, bpm, and bpz).

		$E_{1/2}$ (V)[g]	
Reference	Compound	Oxidation	Reduction
Our Lab[a]	$Co(bpy)_3^{2+}$	0.44 (r)[c]	-0.86 (i)[d]
	$Co(bpm)_3^{2+}$	0.70 (r)	-0.63 (i)
	$Co(bpz)_3^{2+}$	0.97 (r)	-0.45 (q)[e]
Ruminski[b,c]	$Co(bpy)_3^{2+}$	0.31[b], 0.26[c]	-0.84
	$Co(bpm)_3^{2+}$	1.02[b], 0.80[c]	-0.50
	$Co(bpz)_3^{2+}$	N.A.	N.A.

a. See ref. (Fitch et al., submitted)
b. See ref. (Ruminski et al., 1984)
c. See ref. (Ruminski et al., 1985)
d. (r) denotes reversible redox processes with peak potentials given.
e. (i) denotes irreversible redox processes with peak potentials given.
f. (q) denotes quasi-reversible redox processes with peak potentials given.
g. Potentials ($E_{1/2}$) are vs. SCE (saturated calomel electrode)

2. Quantum Mechanical Results

As discussed in earlier, Ernst and Kaim attempted the Hückel calculations on ligands bpm, bpy, and bpz and acquired some relative measurements of π-perturbation and compared these to electrochemical and spectroscopic data (Ernst et al., 1986). However, molecular orbital calculations on ligands explain only the part of the complicated metal-ligand system where relative energetics and mixing of orbitals between metal d orbitals and ligand π^* orbitals occur in a non-uniform pattern. Ligand MO calculations are able to explain the case of the reduction of the metal complexes such as $Ru(bpy)_3^{2+}$, $Ru(bpm)_3^{2+}$, and $Ru(bpz)_3^{2+}$ where ligand π^* orbitals are the first LUMO and easily accessible energetically. This is why the reduction peak potentials of the complexes show the same pattern as the ligands. However, use of ligand MO may fail to describe electronic transitions occurring from the ground state to the excited state of the complex. Metal-to-ligand-charge-transfer (MLCT) occurs from metal d orbitals to ligand π orbitals. Therefore, a correct description of the system using molecular orbitals should include both metal d orbitals and ligand π orbitals in coordination. This complete quantum mechanical approach will also be able to supply information about the net effect of σ bonding and π-back bonding (metal-N bond distance) discussed before (Rillema et al., 1992). We attempted a MO calculation of the metal/ligand system which could describe the metal-to-nitrogen bond distance. First, we tested the accuracy of our quantum mechanical calculation on the ruthenium trisdiimine system. We applied the same methodology to our cobalt system with the same ligands.

First, we examined the ligands. The bpy, bpm, and bpz ligands differ in the position (bpm vs. bpz) or the numbers of N atoms (bpy vs. bpm and bpz)

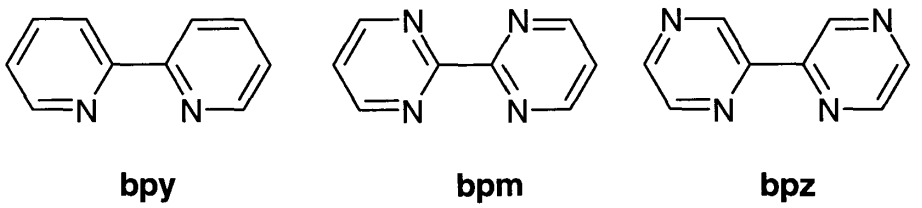

Figure 31. Structure of Bpy, Bpm, and Bpz.

as shown in Figure 31. Figure 32 shows graphical representations of these ligands as a result of ab-initio calculations. The structures of bpy, bpm, and bpz were shown with their own total electron density, actual HOMO (highest occupied molecular orbital), and LUMO (lowest unoccupied molecular orbital). From this result shown in Figure 32, the electron density was drawn with 0.08 electrons/au^3 and this size of the isosurface describes chemical bonds instead of the overall size of the molecule. Notice the encoded red sphere appears at the nitrogens indicating the existence of the lone pair electrons. Also notice that the LUMO of these ligands are composed of p orbitals which are perpendicular to the bipyrimidine-type ring. They are also in anti-bonding pattern within the ring (this is shown by the vectoral representation shown by color; blue is positive and red is negative). Notice the well built p orbitals at the nitrogen (red sphere) which will coordinate to the metal. The π^* (LUMO) ligand orbitals are known to function as electron acceptors which stabilize electrons in the ring at the time of electrochemical reduction. MLCT transition in electronic spectroscopy is also occurring at this ligand

Figure 32. Molecular Orbitals of the Ligands Bpy, Bpm, and Bpz.
The structure and molecular orbitals for (a) bpy, (b) bpm, and (c) bpz ligands are shown.
(1) Tubular representation of the ligands
(2) Electron density with 0.08 electrons/au^3 and this size of isosurface describes chemical bonds instead of the overall size of the molecule;
(3) HOMO (highest occupied molecular orbital) of the molecule
(4) LUMO (lowest unoccupied molecular orbital) the molecule

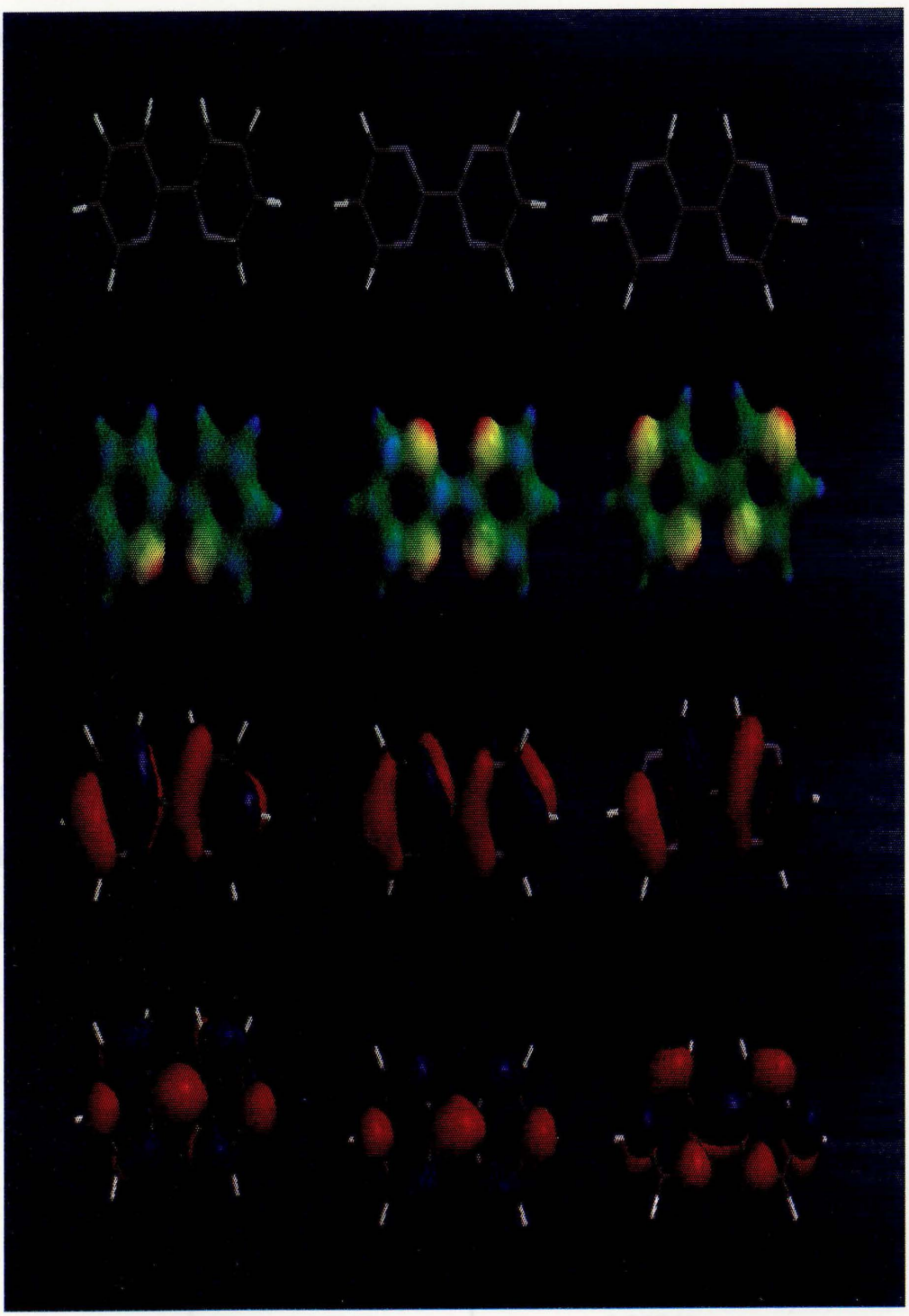
(a)
(b)
(c)
(1)
(2)
(3)
(4)

LUMO. As mentioned earlier, the calculated energy of the LUMO can now be correlated to the experimental one electron reduction potential from electrochemistry. The reduction potentials of the ligand bpy, bpm, and bpz are given in Table 8. The LUMO energies calculated with STO-3G basis sets and 3-21 G basis sets are shown in Table 10. The absolute magnitude of these energies are in 0.05 to 0.2 eV. Ernst and Kaim gave relative LUMO energy (E_{LUMO}) ratio between free ligands. Instead of giving any absolute value for the orbital energy, they used the relative correlation of orbital energy to the Coulomb integral parameter (h_N). They set the energy of SLUMO (second lowest unoccupied molecular orbital) of bpy at $h_N = 0$ as 1.0 and plotted other molecular orbitals relative to this value. The estimated ratio of E_{LUMO} (bpy) to E_{LUMO} (bpz) from their calculation was 1.15. The relative ratio of the LUMO energy of bpy to that of bpz calculated from our Table 10 is 1.21 (STO-3G) and 1.58 (3-21G). Therefore, their semiempirical results are close to our minimal basis set (STO-3G) *ab*-initio results. The calculated LUMO energies were plotted against the experimental reduction potentials and shown in Figure 33. Both basis sets give a reasonable correlation with the trends in the experimental data.

Table 10. LUMO Energies for Ligands, Bpy, Bpm, and Bpz

	E_{LUMO} (eV)	
Ligand	STO-3G	3-21G
Bpy	0.20355	0.09084
Bpm	0.17023	0.06382
Bpz	0.16829	0.05762

Figure 33. Reduction Potentials vs. Calculated LUMO Energies of Bpy, Bpm, and Bpz. Two different reduction potential values from previous experiments were compared.
(a) For the reduction potential, see ref. (Ernst et al., **1986**)
(b) For the reduction potential, see ref. (Kawanishi et al., **1989**)

(a)

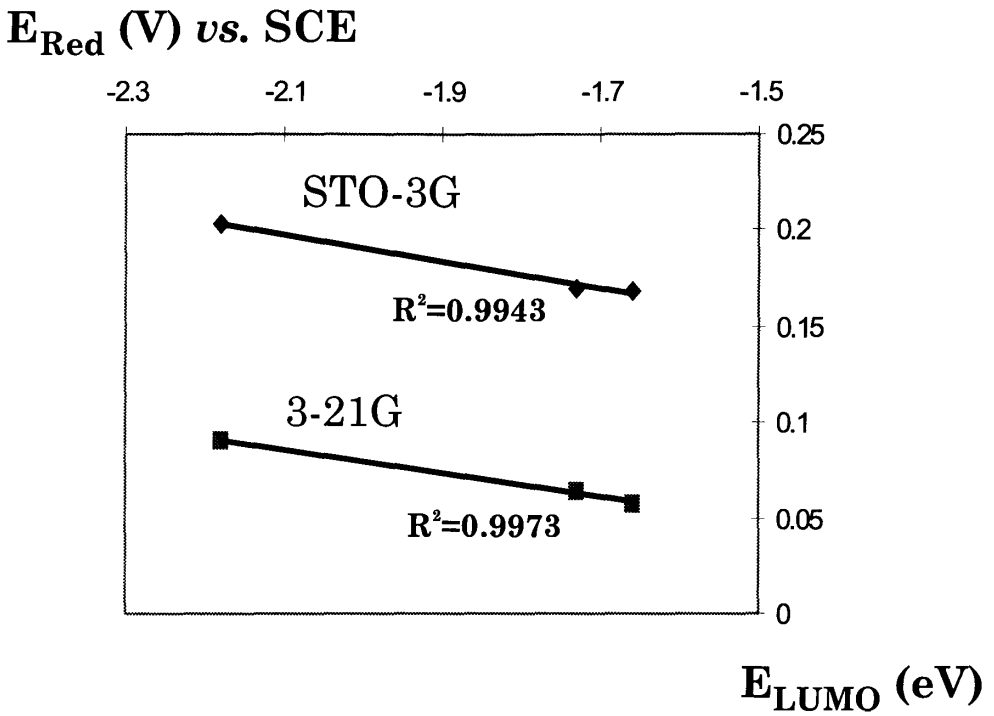
E_Red (V) vs. SCE
-2.3
-2.1
-1.9
-1.7
-1.5
0.25
0.2
0.15
0.1
0.05
0
STO-3G
R²=0.9943
3-21G
R²=0.9973
E_LUMO (eV)

(b)

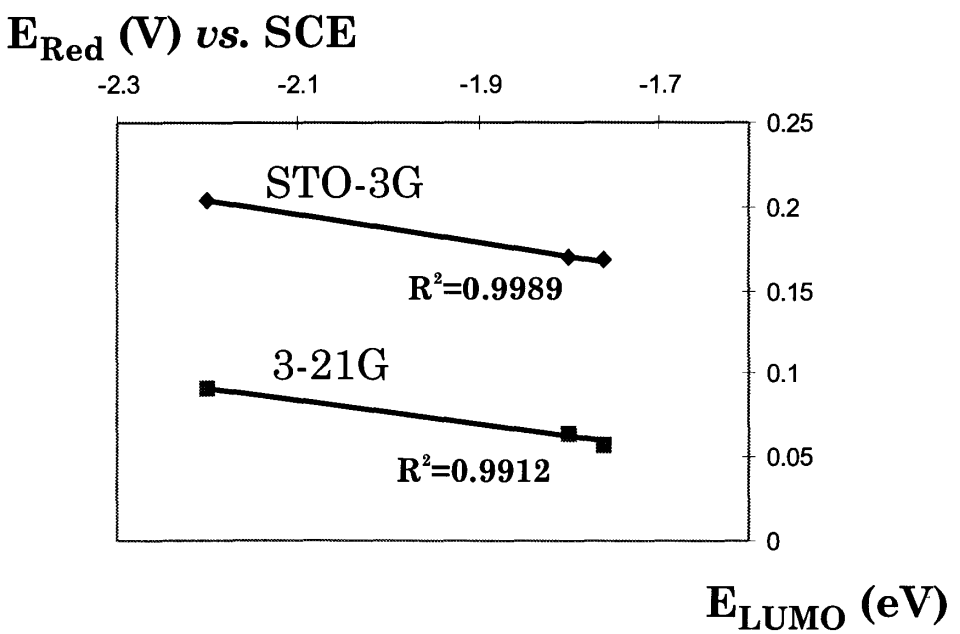
E_Red (V) vs. SCE
-2.3
-2.1
-1.9
-1.7
0.25
0.2
0.15
0.1
0.05
0
STO-3G
R²=0.9989
3-21G
R²=0.9912
E_LUMO (eV)

We next examined the ruthenium complexes, $Ru(bpy)_3^{2+}$, $Ru(bpm)_3^{2+}$, and $Ru(bpz)_3^{2+}$. The redox potentials are given in Table 8. As we did for ligands, we can correlate the calculated energy of the LUMO of the ruthenium metal complexes (not just ligand) to the one electron reduction potential. We can also correlate the HOMO energy to the oxidation potential. The calculated LUMO and HOMO energies of $Ru(bpy)_3^{2+}$, $Ru(bpm)_3^{2+}$, and $Ru(bpz)_3^{2+}$ from the *ab*-initio calculations with 3-21G basis sets are shown in Table 11. Calculated LUMO and HOMO energies were plotted against the

Table 11. Calculated LUMO and HOMO Energies for $Ru(bpy)_3^{2+}$, $Ru(bpm)_3^{2+}$, and $Ru(bpz)_3^{2+}$.

Complex	E_{HOMO} (eV)	E_{LUMO} (eV)
$Ru(bpy)_3^{2+}$	-0.52856	-0.14476
$Ru(bpm)_3^{2+}$	-0.56576	-0.17880
$Ru(bpz)_3^{2+}$	-0.57419	-0.19199

experimental reduction potentials and oxidation potential, respectively, and shown in Figure 34.

The correlation of the electronic spectra to the results from the molecular orbital calculations requires further identification of the molecular orbitals and their energies to obtain correct match of the molecular orbital pair to the corresponding electronic transitions in spectroscopy. Only metal to ligand charge transfer (MLCT) bands of ruthenium complexes have been considered for correlation. (π–π^* transition within the ligand can also be done in the same way by looking for their corresponding energies further down in the MO output.)

Figure 34. Redox Potential vs. LUMO and HOMO of RuL_3^{2+}
Redox Potential vs. Molecular Orbital Energies for RuL_3 (L = bpy, bpm, bpz):
(a) LUMO energy vs. Reduction potential (E_{red})
(b) HOMO energy vs. Oxidation potential (E_{ox})
(NOTE) For reduction and oxidation potential, see ref. (Rillema et al., 1983).

(a)

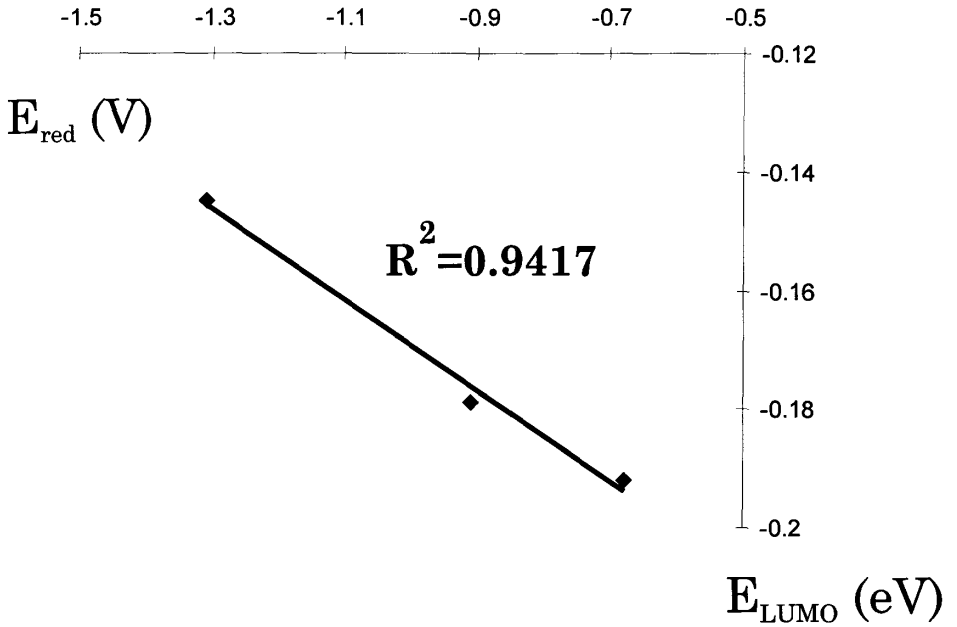
-1.5
-1.3
-1.1
-0.9
-0.7
-0.5
-0.12
-0.14
-0.16
-0.18
-0.2
E_{red} (V)
R^2=0.9417
E_{LUMO} (eV)

(b)

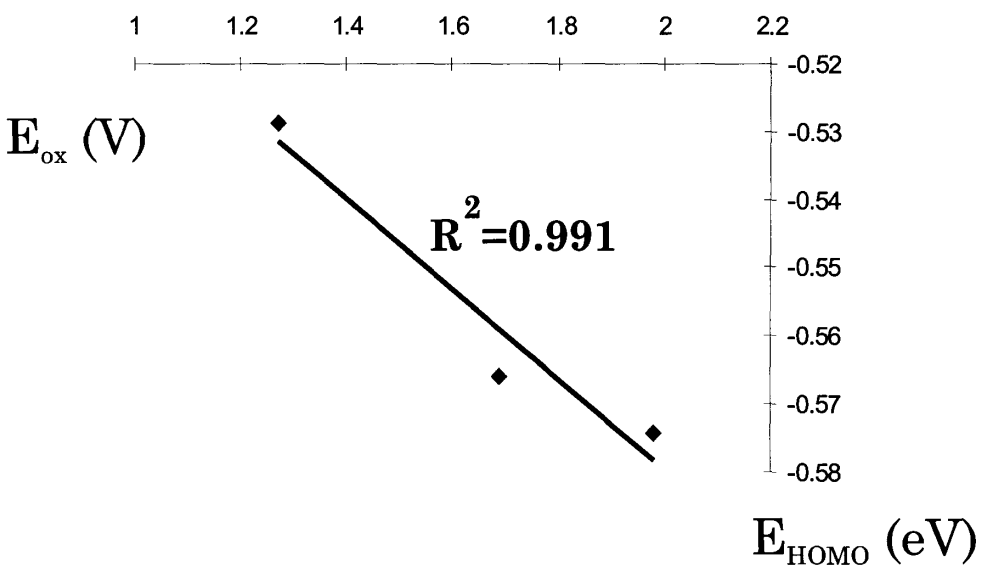
1
1.2
1.4
1.6
1.8
2
2.2
-0.52
-0.53
-0.54
-0.55
-0.56
-0.57
-0.58
E_{ox} (V)
R^2=0.991
E_{HOMO} (eV)

Crutchley and coworkers (Crutchley et al., 1982) assigned the metal to ligand transitions of $Ru(bpy)_3^{2+}$ at 22,125 cm^{-1}, 28,985 cm^{-1}, and 30,960 cm^{-1}. For the calculation of a theoretical wavenumber for MLCT bands of $Ru(bpy)_3^{2+}$, the eigenvalues for the molecular orbitals around the HOMO and LUMO were used to draw the molecular orbital vs. energy diagram. The energy levels for the molecular orbitals which are responsible for the MLCT transition were determined by considering corresponding energies of metal d orbital and ligand π^* orbitals. For the ligand π^* orbitals, their degeneracies were also examined. As a result, the molecular orbital at -0.52856 eV was assigned to the metal (Ru) *d* orbital responsible for MLCT transition. On the other hand, the molecular orbitals at -0.14476, -0.10659, and -0.09251 were assigned to the ligand π^* orbitals responsible for the first, the second, and the third MLCT transition, respectively, according to their relatively higher lying non-degenerate energies. The calculated energies of MLCT transitions (E_{MO}) are tabulated with the experimental values (E_{Spec}) in Table 12. The energy difference between molecular orbitals in eV can

Table 12. Metal to Ligand Charge Transfers (MLCT) and Calculated MO Energies of $Ru(bpy)_3^{2+}$

transition	E_{ligand}-$E_{HOMO(metal)}$	E_{MO} (cm^{-1})	E_{Spec} (cm^{-1})[1]
MLCT 1	-0.5286 - 0.14476	3095.5	22125
MLCT 2	-0.5286 - 0.10659	3403.4	28985
MLCT 3	-0.5286 - 0.09251	3516.9	30960

be converted to wavenumber in cm^{-1} by using Planck's equation:

[1] See Ref. (Crutchley et al., 1982).

[70] $$E = \frac{hc}{\lambda} = hc\tilde{\nu}$$

where h is the Planck's constant (6.62608 x 10^{-34} Js), c is the speed of the light (2.99792458 x 10^{8} ms^{-1}), λ is the wavelength, and $\tilde{\nu}$ is the wave number (cm^{-1}). The conversion factor hc (= 1.98645 x 10^{-23} J cm) can be used for convenience. Also,

[71] 1 eV = 96.485 $kJmol^{-1}$.

The calculated transition wavenumber (in cm^{-1}) was plotted against the experimental MLCT wavernumbers as shown in Figure 35. There is a good correlation between the trends in calculated transition energy for MLCT and the experimental trends in transition energy. However, the absolute value of the calculated MLCT transition energy did not give a good value which is close to the measured spectroscopic value. Ernst and Kaim also did not attempt to provide direct comparison between their calculation results and the measured MLCT energies (Ernst et al., **1986**).

Next, we examine the argument Rillema and co-workers made for the net effect on the bond between ruthenium and the coordinated nitrogen. There are several ways to get the information about the total overlap or population of the electrons found in the molecular orbitals or atoms such as Mulliken Population Analysis (MPA) and Natural Population Analysis (NPA). It would be most useful if we can have information regarding amount of bonding between atoms which include all σ and π electron effects arising between the atoms of our interest. Here, I used the Mulliken bond order matrix and Löwdin bond order matrix to examine and correlate with the bond lengths studied for Ru-N distance in RuL_3^{2+} complexes (L = bpy, bpm, and bpz) by X-ray

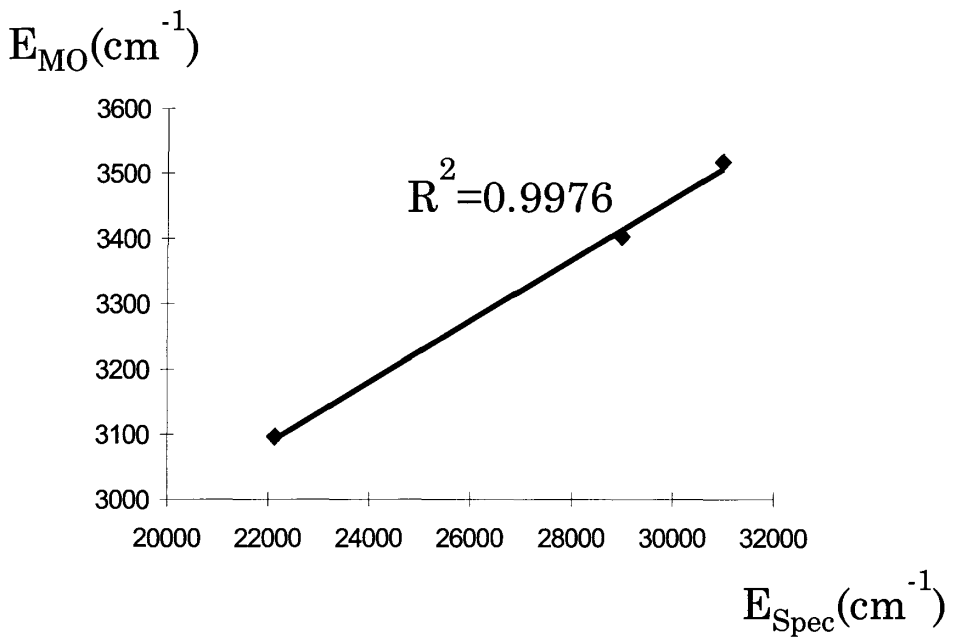

Figure 35. Calculated MLCT from Molecular Orbital Calculations vs. MLCT from UV Spectroscopy.

crystallography. The crystallographic results (Rillema et al., 1983) of the bond lengths for the ruthenium complexes are shown in Table 13.

Table 13. Ru-N Bond Distance in Ruthenium(II) Complexes.

Complex	Bond Length; Ru-N (Å)[1]
$Ru(bpy)_3^{2+}$	2.056 (2)
$Ru(bpm)_3^{2+}$	2.067 (4)
$Ru(bpz)_3^{2+}$	2.050 (1)

The Mulliken bond order is introduced by Mayer and detailed definition should be consulted if needed (Mayer, 1983; Mayer, 1984). Mulliken bond order is based on Mulliken's population analysis (see Chapter IV section C) while Löwdin bond order analysis is based on symmetrical orthogonalization of orbitals (Löwdin, 1970). From the results of the MO calculations on ruthenium complexes, these two bond order matrices were obtained. The corresponding pair of Ru-N bonds were examined by both the Mulliken bond order scheme and Löwdin bond order analysis. The direct comparison of bond order vs. bond length of Ru-N is given in Table 14.

Table 14. Bond Order *vs.* Bond Length of Ru-N in $Ru(bpy)_3^{2+}$, $Ru(bpm)_3^{2+}$, and $Ru(bpz)_3^{2+}$.

Complex	Ru-N $_{(X\text{-ray})}$ (Å)	Mulliken bond order	Löwdin bond order
$Ru(bpy)_3^{2+}$	2.056	0.28502	0.577245
$Ru(bpm)_3^{2+}$	2.067	0.28296	0.58979
$Ru(bpz)_3^{2+}$	2.05	0.28553	0.588775

[1] See Ref. (Rillema et al., 1983).

While Mulliken bond order shows good inverse correlation between the bond order and bond length from the crystallography, Löwdin bond order scheme does not. The resulting Mulliken bond order has been plotted against the X-ray crystallographic bond length data and shown in Figure 36.

In summary, computations performed on the free ligands and the ruthenium complex systems show similar trends in oxidation potential with HOMO, reduction potential with LUMOs, experimental (X-ray crystallographic) bond length with bond order, and experimental MLCT with calculated MLCT. The absolute magnitudes of these latter numbers are off by an order of magnitude. The deviation may be due to the fact that purely theoretical quantum mechanical calculation does not account for many experimental parameters such as solvent effect, the use of reference electrode to measure the relative potential, and instrumental errors.

Finally, the tested molecular orbital calculations are extended to the cobalt metal complexes CoL_3^{2+}, where L is bpy, bpm, and bpz. Co^{2+} is d^7 which bears one unpaired electron within the metal d orbital. This makes the system spin multiple meaning that the reduction of the system involves either accepting α electron or β electron. Full treatment of unrestricted open shell calculations have been performed to account for spin multiplicity.

As shown in Figure 30, $Co(bpm)_3^{2+}$ has a nice reversible oxidation peak and an irreversible reduction peak. Other cobalt complexes also have nice reversible oxidation peaks with either irreversible ($Co(bpy)_3^{2+}$) or quasi-reversible ($Co(bpz)_3^{2+}$) reduction peaks. Quantum mechanical calculations were used to obtain both energy of the HOMO

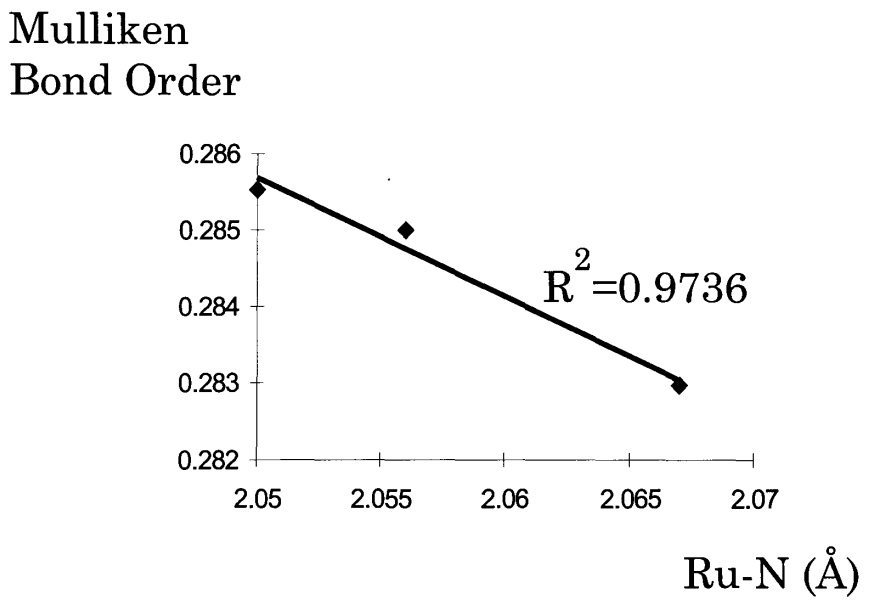

Figure 36. Bond Length (X-ray crystallography) vs.
Calculated Mullikne Bond Order.

and energy of the LUMO for correlation with oxidation and reduction potentials, respectively. (See Table 9 for redox potentials of cobalt complexes.) As was obtained for the $Ru(bpy)_3^{2+}$ complex, there was a good correlation in trends between the oxidation potential and the energy of the HOMO. The correlation in trends between the reduction potential and energy of the LUMO was also relatively good considering the reduction peak's irreversibility. (See Figures 30 and 37.) As shown in the Figure, the oxidation potential was correlated with α spin HOMO (highest occupied molecular orbital) while the reduction potential was correlated with both α spin LUMO and β spin LUMO.

The absolute magnitude of the orbital energy (eV) is similar to the values obtained by Sun and co-workers (Sun et al., 1994). However, these do not match the magnitude of experimental reduction potential due to solvation effects (Meites et al., 1977).

D. Conclusions

The method of quantum mechanical calculations has been used to study one of the most studied metal chelates, $Ru(bpy)_3^{2+}$. The attention to this compound was due to its historical photochemical importance and possible use in energy containing device molecules. Study of ligand alone, as others previously did, gave a good descriptive measure of one electron reduction of ligands and this was used to interpret the result of metal complex reduction. We extended computational studies to the metal chelates to explain bond distances and MLCT bands. Correlation of well known RuL_3^{2+} (L = bpy, bpm, and bpz) to experimental results were successful and easy to understand due to its

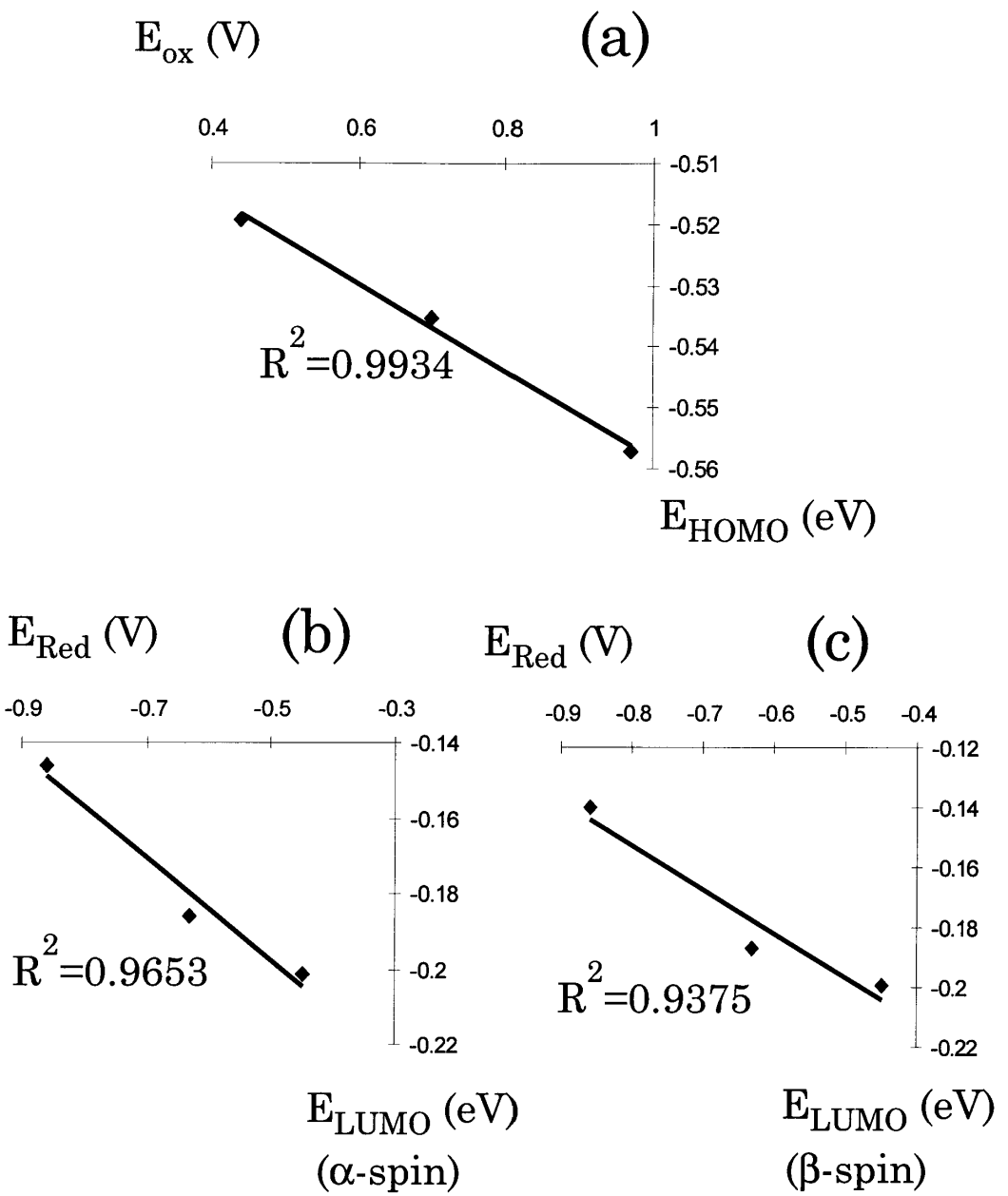

Figure 37. Redox Potential vs . HOMO and LUMO Energies of $Co(bpy)_3^{2+}$, $Co(bpm)_3^{2+}$, and $Co(bpz)_3^{2+}$
(a) oxidation potential vs. α-spin HOMO energy; (b) reduction potential vs. α-spin LUMO energy; (c) reduction potential vs. β-spin LUMO energy.

clean spin state (d^6) with no open shell property involved. The electrochemical redox potentials were correlated with the energies of corresponding LUMO and HOMO. A successful description in MLCT transition of spectrometry using the molecular orbitals and their energy differences was obtained. Bond order using Mulliken analysis gave an explanation of the determination of bond length Ru-N in ruthenium trisdiimine complexes. Löwdin bond order analysis did not give the same results.

The use of quantum mechanics in open shell system in cobalt trisdiimine also gave appropriate trends. The experimentally observed nice reversible oxidation peaks were well correlated with the energy of the HOMO of the corresponding complex. In the case of reduction, experimentally observed irreversible peaks as well as the doubly available LUMO due to its spin multiplicity made the interpretation more complex. However, the correlation between the observed reduction potential with the calculated LUMO energies both in α spin state and β spin state was relatively in good agreement considering the irreversibility of the reduction peaks.

Chapter IX.

Effects of the Substituent Group on Electrochemical Cleavage of 5-(Phenylsulfonyl)-3,4,5,6-tetrahydropyran-2-one (PSTHP): Electrochemical Observation vs. Quantum Mechanical Calculations

A. Introduction

Lactones are important compounds in biology. Lactones can be used to derive pheromones[1] such as sulcatole (Byrne et al., 1974; Mori, 1975):

Scheme III.

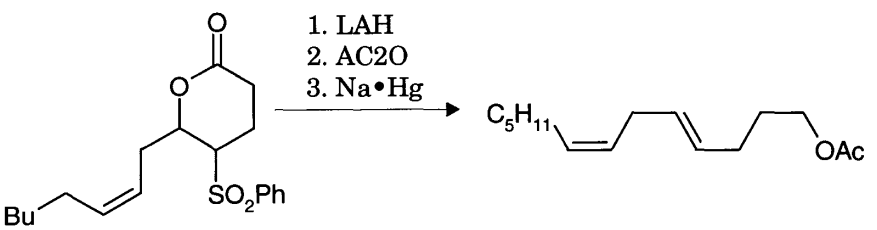

[1] pheromone: A chemical secreted by an animal, especially an insect, that influences the behavior or development of others of the same species.

A synthetic route to lactones has been proposed in which an α-carboxylate (4-phenylsulfonylbutanoic acid (4-PSBA)) is reacted with a ketone ($HCOR_1$) to give the sulfone substituted lactone (Thompson, 1987) as shown in Scheme II.

Scheme II.

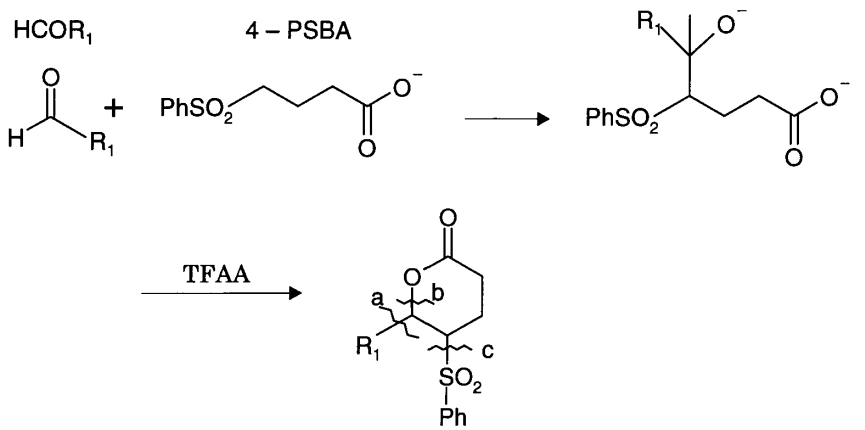

In order to remove the sulfone substituted group which is no longer needed, reductive cleavage is necessary. In developing the reductive cleavage of the phenylsulfone group shown in scheme II, possible locations of electroactive groups within the compound are examined. The R_1, ester, and sulfone groups are indicated. Since activation of the phenyl (activated by an unsaturated group) and ester groups (activated either in the α or β position) is not apparent, the most likely position is the sulfone group (denoted as c in Scheme II).

The phenyl group attached to sulfone group gives great stability to the leaving group due to its ability to delocalize charge. This delocalized effect from phenyl ensures that the cleavage is being made at sulfur-carbon bond (shown as cleavage point c in Scheme II). The delocalization of the sulfone group with the aryl group was attributed to

electronic coupling of the 3d orbitals centered on S with π orbitals in the aryl system (Lamm, et al., 1974).

Recently, the application of electrochemical cleavage to remove the sulfone group utilized in the chemical synthesis has been proposed in our lab (Lohr Jr., 1996). The purpose of the original study was to provide the electrochemical technique to remove the phenylsulfones from molecules to produce lactones and lactams. On the basis of already known electrochemical behavior of sulfones (Baizer et al., 1983) and the use of Simonet Diagram (Manoušek et al., 1968), the general mechanism of cleavage of phenylsulfones was proposed and shown in Figure 38. In general, the cleavage of all aromatic sulfone groups occurs with the breakage of the C-S bond of the sulfone anion radical as the fast reaction step (shown as step 2 in Figure 38). If the reaction of the lactone radical formation is fast and only occurred near the electrode surface (in step 2), the following reduction is enabled by the electrode and the formation of lactone anion occurs. Then, the resulting strong base can be protonated by the solvent or acidic impurities to form a lactone. If the formation of lactone radical is slow, the lactone radical may well migrate to the diffusion layer or to the bulk, and reduction occurs from the electron transfer from another phenylsulfone anion radical nearby which was formed in step 1. (See Scheme III for the reaction.)

Scheme III.

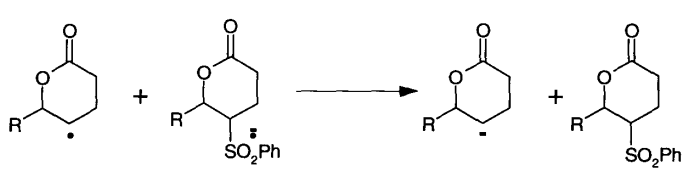

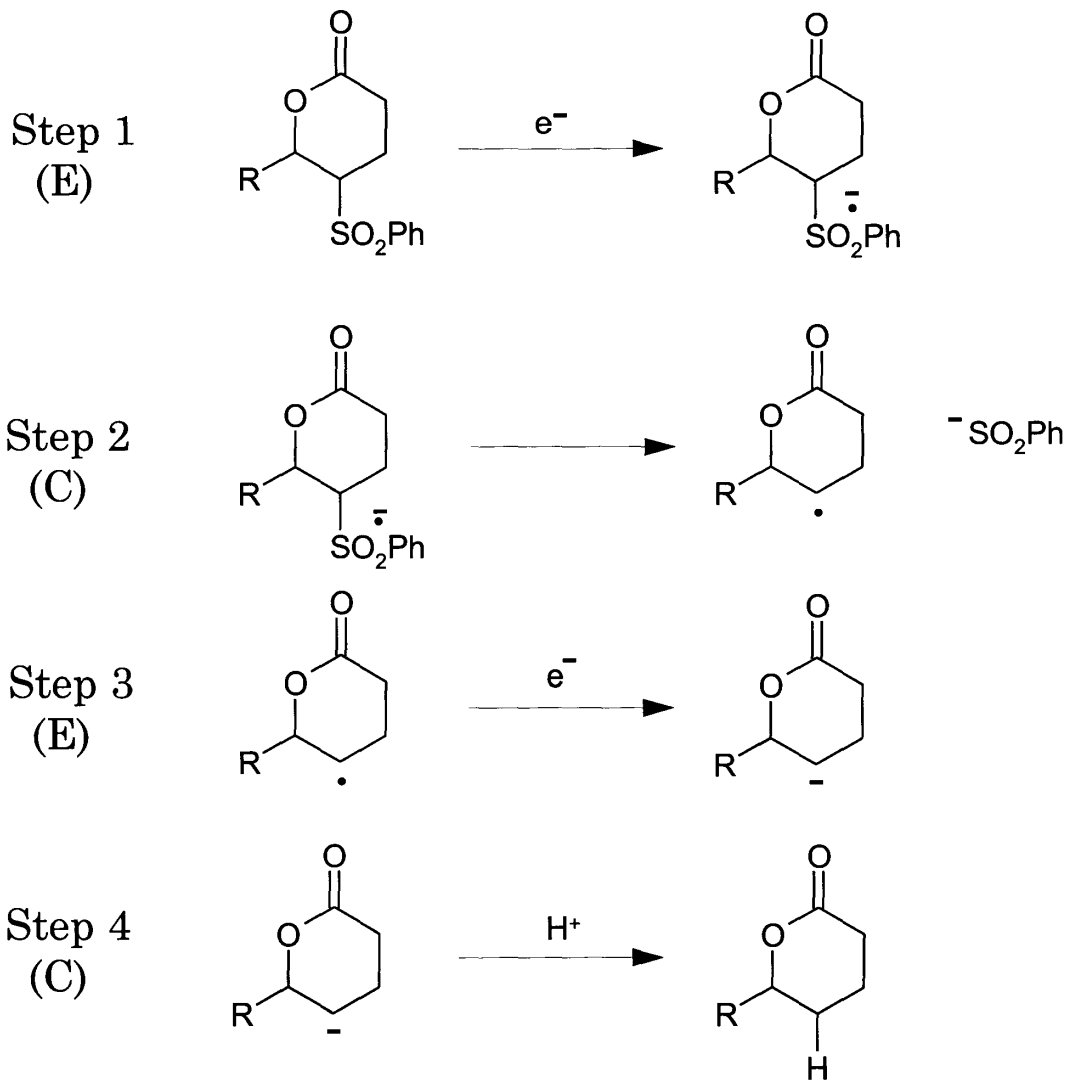

Figure 38. Electrochemcial Reduction of Phenylsulfones (Proposed Mechanism).

In Joe Lohr's study of the cleavage of phenylsulfones, the rate of the reduction and the measurements of the reduction potentials were carried out by cyclic voltammetry. For his study and my theoretical study, three different compounds have been used, TB(PSTHP), CH(PSTHP), and P(PSTHP). The structures, full name of the compounds, and molecular weight are shown in Figure 39.

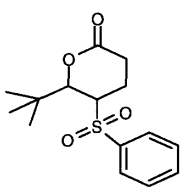

6-tert-butyl-5-(phenylsulfonyl)-3,4,5,6-tetrahydropyran-2-one
mwt 292.38
TB(PSTHP)

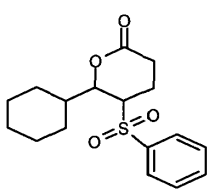

6-cyclohexyl-5-(phenylsulfonyl)-3,4,5,6-tetrahydropyran-2-one
mwt 318.43
CH(PSTHP)

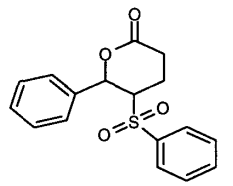

6-phenyl-5-(phenylsulfonyl)-3,4,5,6-tetrahydropyran-2-one
mwt 312.37
P(PSTHP)

Figure 39. Structures of Substituted PSTHP.

B. Methods

To investigate the redox behavior of three phenylsulfonyl compounds with respect to substituents, a total of 12 sets (six for MNDO optimization and another six for 6-31G single point ab-initio calculations) of quantum mechanical calculations have been carried out. Reactant molecules (as shown in left hand side of step 1 in Figure 38) and lactone radicals (as shown in right hand side of the arrow in step 2 in Figure 38) were used for molecular orbital calculations.

To locate the lowest-energy configurations (global minima), four different tetrahydropyran-2-one conformers were considered for beginning structures for

optimization. Depending on the relative position of the alkyl substituent and the phenyl sulfone group, four different conformers considered are shown in Scheme IV. Remember that the name of a cis conformer AE denotes the phenylsulfonyl group at 5 position being axial and the alkyl substituent at 6 position being equatorial. All of three substituted PSTHP structures were built in these four (AE, EA, EE, and AE) conformers and further minimized by the molecular mechanics calculations within Cerius[2] (see ref. Cerius[2], 1992) using a UFF (Universal Force Field). The corresponding structures were

Scheme IV.

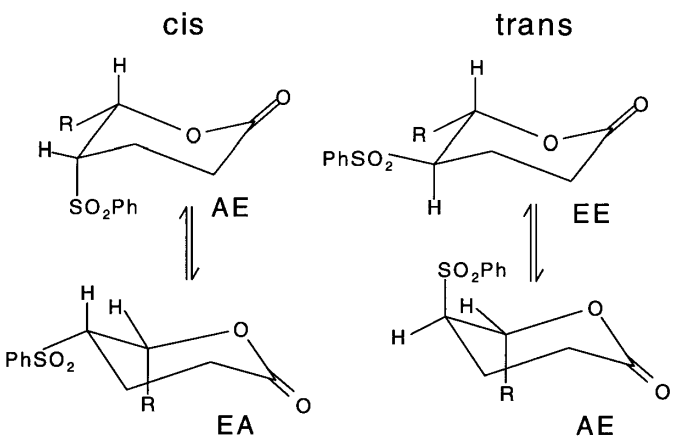

imported to Spartan (see ref. Spartan, 1993) for the further quantum mechanical calculations. Geometry optimizations using semiempirical MNDO (Modified Neglect of Diatomic Overlap, see Chapter IV for more) basis sets were carried out for the minimized conformers. Finally, single point calculations using *ab*-initio 6-31G basis set were performed for the electronically optimized conformers.

Population analysis in terms of bond order was used to explain the possible location of bond breakage at the time of electrochemical reduction. Geometry optimized

structures of all conformers were examined to find the differences between the electronically favored (low in formation energy) structure and others. Molecular orbitals, especially, HOMO and LUMO of the favored structures were also used to examine the previously proposed mechanism of electrochemical reduction. Molecular orbital energies of the favored substituted PSTHP conformers were compared and related with their electrochemical reduction potentials.

C. Results and Discussion

For comparison purposes, the previous electrochemical data for the redox potentials of the compounds, TB(PSTHP), CH(PSTHP), and P(PSTHP) are given in Table 15.

Table 15. Electrochemical Data of Phenylsulfones.

	Reduction Potential *vs.* Ag/AgCl	
Substituent	E_{red}^1 (V)	E_{red}^2 (V)
Phenyl	-2.1	-2.5
Cyclohexyl	-2.1	-2.4
t-butyl	-2.4	> -2.8[1]

As shown in the table, the reduction of phenyl substituted compound and cyclohexyl substituted compound showed very similar reductions for both the first and the second electron. However, t-butyl substituted compound was harder to reduce than cyclohexyl or phenyl substituted compounds shown by a more negative reduction potential for the

[1] reduction peak not observed within the scan range

first electron than other two compounds. The second reduction peak was not observed from the scan between -1.7V and -2.8V *vs.* Ag/AgCl. Therefore the second reduction of this compound appears to occur at more negative potential than -2.8V *vs.* Ag/AgCl.

The calculated heats of formation for the geometry optimized conformers representing local minima are listed in Table 16. Notice the lowest energy conformers

Table 16. Calculated Heats of Formation of Low Energy Conformers of Substituted PSTHP

Heat of formation (kcal/mol)	*Trans* (Initial conformation)		*Cis* (Initial conformation)	
	AA	EE	EA	AE
phenyl-PSTHP	-95.004	-96.206	-95.601	-92.284
cyclohexyl-PSTHP	-140.318	-139.268	-140.497	-131.993
t-butyl-PSTHP	-124.089	-124.160	-118.871	-117.068

for phenyl and t-butyl substituted PSTHP occur in 'trans' conformation while the cyclohexyl-PSTHP has a 'cis' conformation based on the original structure (before geometry optimization).

Two things can be observed from the table. The first is the absolute magnitude of the heats of formation in kcal/mol. These relatively large negative values are consistent with other computations of this type. For trans-1,2-difluorocyclohexane, the calculated (AM1 semi-empirical) heat of formations of -127.19 kcal for AA (axial-axial

substituted) and -128.68 kcal/mol for EE (equatorial-equatorial substituted) were previously reported (Hehr et al., 1993).

The second point to note from the table is the fact that there is relatively little energy difference between any of the four initial conformers, except that, in general, a trans conformation appears to be favored. Figure 40 shows minimized results of 4 different initial conformers for cyclohexyl-PSTHP. As shown in the figure, none of these conformers are structurally close. However, two low energy conformers, AA and EA in Table 16, are clearly different with respect to the orientation of the substitution. Therefore, they are at different local minima. On the other hand, the conformer EE looks more like AA after the optimization and we can say that axial substitution is preferred to equatorial in the case of 'trans' conformer.

From our results, the naming of these conformers of axial (A) and equatorial (E) as shown in Table 16 are no longer applicable for some of the low energy structures (local minima). However, I will use same naming scheme for convenience. Notice that the alkyl groups are at equatorial position for phenyl and *t*-butyl substituted PSTHP while cyclohexyl-PSTHP has axially substituted alkyl group. The structures of these lowest energy conformers are shown in Figure 41. None of these optimized structures adopt a text book *aa, ea* conformation.

The lowest energy phenyl substituted PSTHP is in a trans configuration as mentioned above. Previous NMR and isolation results by Thompson and co-workers[1]

[1] NMR measured by C. Thompson, Loyola University, Chicago.

Figure 40. Geometry Optimized Structures of Cyclohexyl-PSTHP From 4 Different Initial Conformers
The geometry optimization was started from the following four different initial conformers:
(a) AA (both phenylsulfone and cyclohexyl groups at axial position)
(b) EE (both phenylsulfone and cyclohexyl groups at equatorial position)
(c) EA (phenylsulfone at equatorial and cyclohexyl at axial)
(d) AE (phenylsulfone at axial and cyclohexyl at equatorial)

* The conformers AA (trans) and EA (cis) can be still called as AA and EA, respectively after geometry optimization as shown in (a) and (c). However, the conformer EE in (b) is no longer in its EE substitution pattern. Instead, it is more like a form of AA. Therefore AA conformation is preferred for the trans conformer. For more accurate information about the most preferred conformation with respect to substitution, more complete configuration search may be desired (Monte Carlo calculation does this more efficiently).

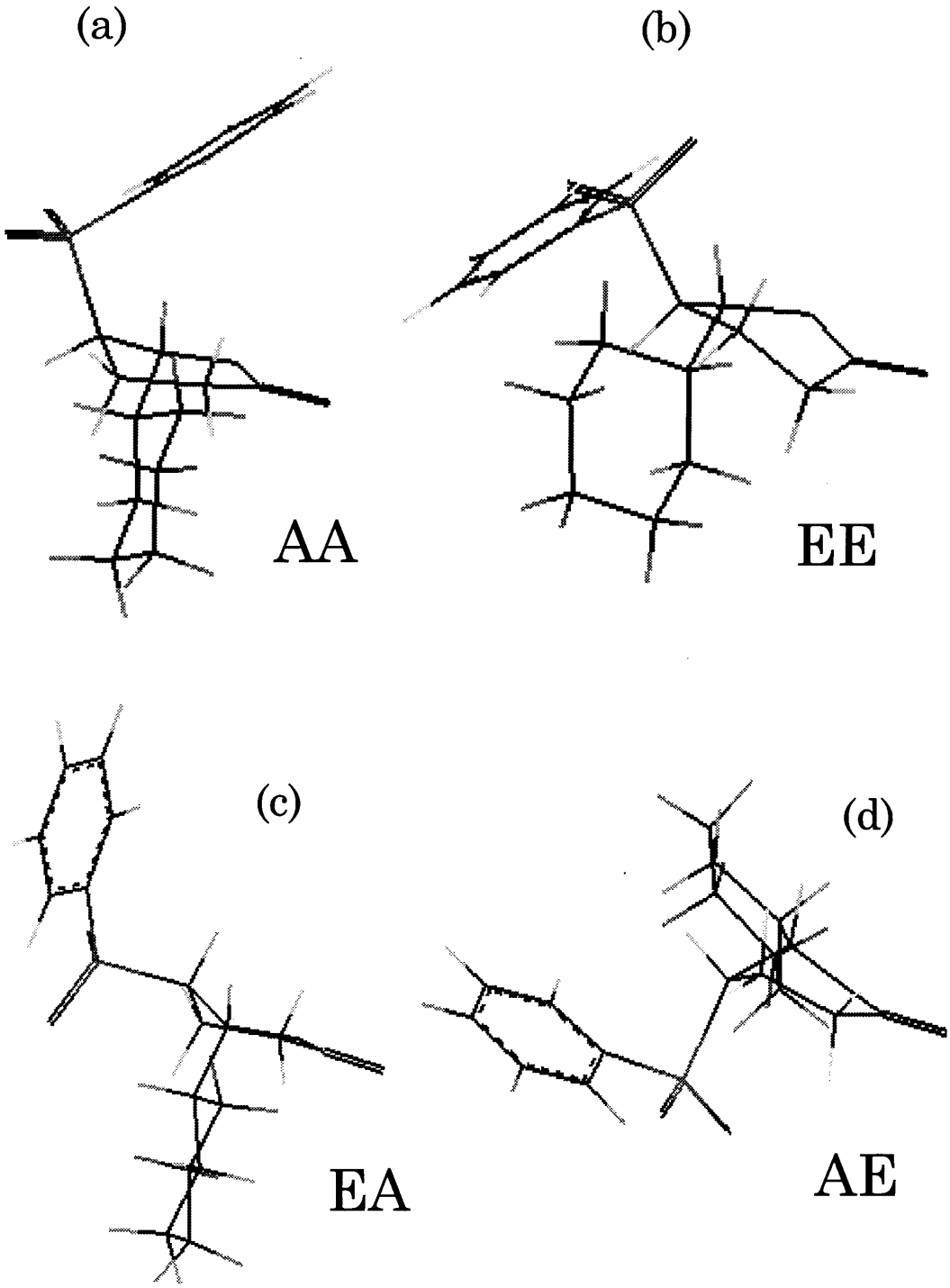
(a)
(b)
AA
EE
(c)
(d)
EA
AE

Figure 41. The Lowest Energy Conformers of Substituted PSTHPs.
Skeletal structures showing the calculated lowest energy conformers for the substituted PSTHPs are given. To search the lowest energy structure, MNDO geometry optimizations were performed with d orbitals included for sulfur atom in phenylsulfone group; (a) phenyl-PSTHP; (b) cyclohexyl-PSTHP; (c) t-butyl-PSTHP.

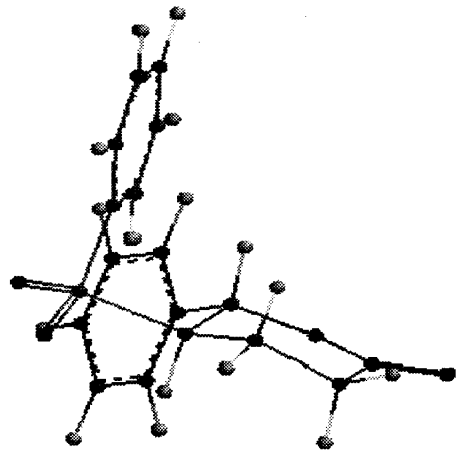

(a)

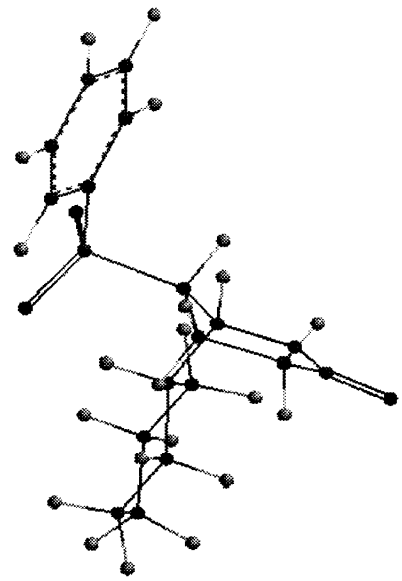

(b)

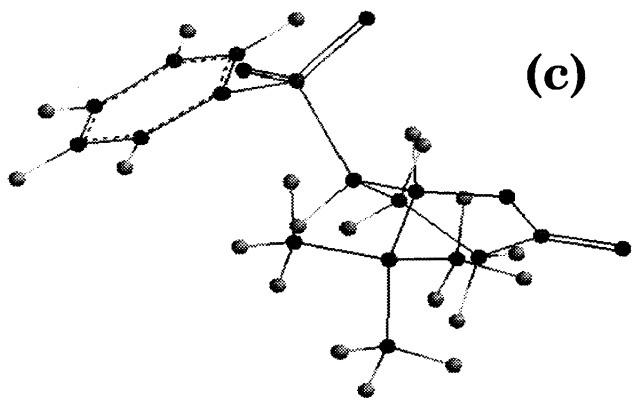

(c)

indicated a 95/5 % trans/cis isomer ratio. Notice the 'EE' conformer of phenyl-PSTHP trans isomer does not experience much steric effect even though phenylsulfone and phenyl group substituent are in equatorial position. Other conformers of phenyl-PSTHP were also examined. The steric effect is found to be the greatest in the case of AE (cis) conformer where the phenyl substituent and phenylsulfone's phenyl ring are oriented face to face.

Notice the 'EA' conformer (cis) of cyclohexyl-PSTHP has a good distance between the cyclohexyl substituent and the phenylsulfone. The chair configuration of original 'EA' conformer as shown in Scheme IV is relatively well kept after geometry optimization except for the ketone group having a different orientation from the one in Scheme IV.

The lowest energy structure for t-butyl-PSTHP is 'EE' (trans) conformer as shown in Table 16. However, the structure of EE conformer shown in Figure 41 no longer looks like 'EE' conformer of 'trans'. The tetrahydropyran (THP) moiety loses its chair conformation. The *t*-butyl substituent and phenylsulfone make somewhat AA´ or EA´ like conformer. The previous NMR data by Thompson and co-workers also showed the existence of a single conformation which is best described as intermediate between the 'cis' and 'trans' forms. They also attributed this hybrid state to the existence of bulky t-butyl group.

From the proposed mechanism of electrochemical cleavage of the phenylsulfones shown in Figure 38, the first electron was postulated to produce the phenylsulfone anion. One way to study this mechanism is by examining the LUMO of

the molecules. The LUMO of the lowest energy conformers of TB(PSTHP), CH(PSTHP), and P(PSTHP) are shown in Figure 42. Notice LUMOs for all substituted PSTHP are located at phenyl rings of phenylsulfones. The overlap between the sulfone and corresponding carbon in phenyl shows that there is a well developed orbital overlap between sulfur and phenyl ring. The delocalization of the sulfone group with the aryl group was previously attributed to electronic coupling of the 3d orbitals centered on S with π orbitals in the aryl system (here, phenyl group). This delocalized LUMO may explain delocalization of the electron uptake centered at sulfonyl moiety at the time of electrochemical reduction. As a result, phenylsulfones behave as a good leaving group and bond breakage occur between lactone ring and phenylsulfone.

Direct comparison of calculated bond orders of all possible electroactive sites may also give some hints on where the first electron reduction occurs. The comparison of bond orders for sulfone to lactone (c in Scheme II), O-C bond in possible ring opening site in lactone (b in Scheme II), and alkyl substituent to lactone (a in Scheme II) for the lowest energy conformers is shown in Table 17. From both Mulliken bond order analysis and Löwdin bond order analysis, the bond between sulfone group and lactone ring is the weakest bond (bond order of 0.83 ~ 0.90). Considering the definition of bond order that bond order of 1 describes the single bond and bond order of 2 means double bond, the lower the bond order, the weaker the bond strength, the longer the bond length. The correlation between the calculated bond order and experimental bond length of conjugated ring system was studied by using semiempirical molecular orbital calculations (Jung et al., 1983). They obtained bond order of 0.776, 0.658, 0.547, and

Figure 42. The LUMOs of Substituted PSTHPs.
The calculated LUMO surfaces are shown for PSTHPs. The geometry of these were obtained by MNDO semiempirical calculations with d orbitals included. Then the Hartree-Fock ab-initio calculations with 6-31G* basis set were carried out for the final electronic structure calculations; (a) phenyl-PSTHP; (b) cyclohexyl-PSTHP; (c) t-butyl-PSTHP.

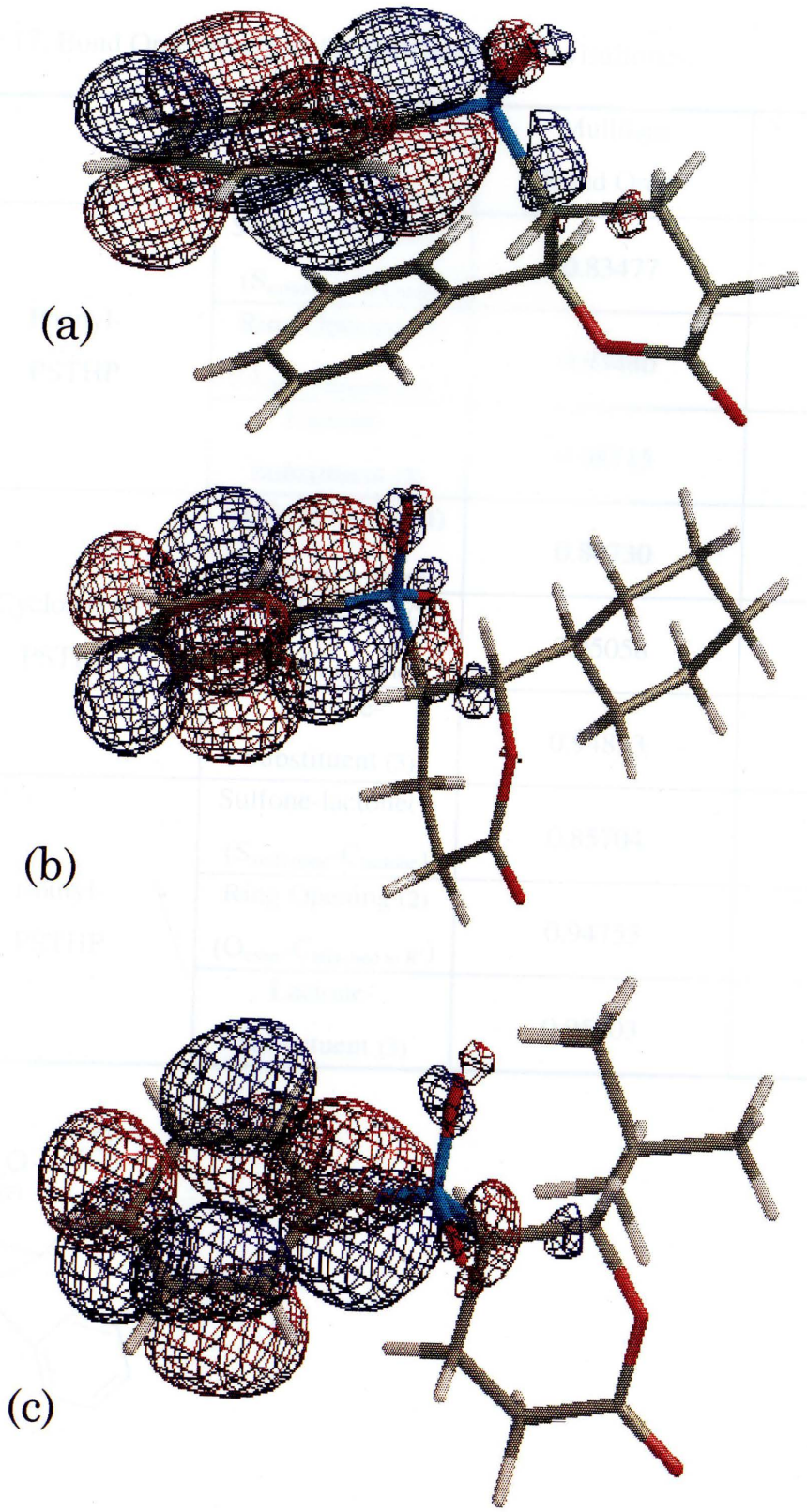
(a)
(b)
(c)

Table 17. Bond Order Analysis for Substituted Phenylsulfones.

		Mulliken Bond Order	Löwdin Bond Order
Phenyl-PSTHP	Sulfone-lactone (1) ($S_{sulfonone}$-$C_{lactone}$)	0.83477	0.89202
	Ring Opening (2) (O_{ester}-$C_{attached\ to\ R'}$)	0.93480	1.21847
	Lactone-Substituent (3)	0.98715	1.01385
Cyclohexyl-PSTHP	Sulfone-lactone(1) ($S_{sulfonone}$-$C_{lactone}$)	0.84730	0.90036
	Ring Opening (2) (O_{ester}-$C_{attached\ to\ R'}$)	0.95058	1.23435
	Lactone-Substituent (3)	0.94853	1.00683
t-butyl-PSTHP	Sulfone-lactone(1) ($S_{sulfonone}$-$C_{lactone}$)	0.85704	0.89523
	Ring Opening (2) (O_{ester}-$C_{attached\ to\ R'}$)	0.94753	1.22941
	Lactone-Substituent (3)	0.95303	0.97658

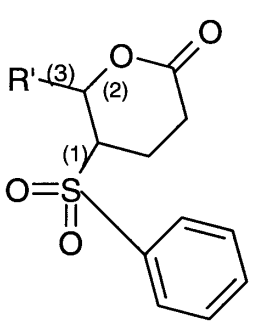

0.513 for different compounds and related with IR-stretch data of 1564, 1514, 1443, and 1414 cm^{-1}, respectively. Therefore, the 10% difference between the bond order of sulfone-lactone (0.83~0.86) and that of other possible positions of electrochemical reduction (0.93~0.99) can be considered significant. The weakest bond order of sulfone leaving group is consistent with the proposed mechanism where the first electron reduction occurs at the phenylsulfone making a phenylsulfone anion.

To compare with the experimental reduction potentials, the energy of the LUMOs of each energetically preferable substituted PSTHP was obtained and listed with its reduction potential in Table 18. The total energy of each substituted compound

Table18. Calculated LUMO energies of substituted PSTHPs

compound	$E_{hartree}$ (a.u.[1])	E_{LUMO} (eV)	E_{red}[1] (V)	conformation
phenyl-PSTHP	-1349.9	0.07727	-2.1	*trans EE*
cyclohexyl-PSTHP	-1353.4	0.07110	-2.1	*cis EA*
t-butyl	-1276.5	0.07283	-2.4	*hybrid*

from the geometry optimization was also given for reference. The magnitude of these numbers (total energies in hartree or a.u.) can also be compared with other computational results. For example, the calculated total energy of axial and equatorial chlorocyclohexane by *ab*-initio calculations with 3-21G basis set are -689.73222 and -689.73386 a.u. (Hehr et al., 1993).

[1] 1 a.u. = 627.5 kcal/mol

The LUMO of the each substituted PSTHP was not very different. Therefore the difference in the reduction potential of *t*-butyl PSTHP in the first reduction as shown in Table 15 may not be entirely explained by LUMO energies for the lowest energy conformers.

Lactone ring systems are known to flip between the conformational isomers. Experimentally, the trans form of the phenyl substituted PSTHP and t-butyl PSTHP are reduced at values differing by 300 mV despite small differences in the calculated LUMO. This may suggest that the 'trans' form of either phenyl or t-butyl substituted PSTHP further go through an electrochemical chemical electron transfer (CE) step where the trans configuration of the lactone ring flips to another conformational isomer as shown in Scheme V:

Scheme V.

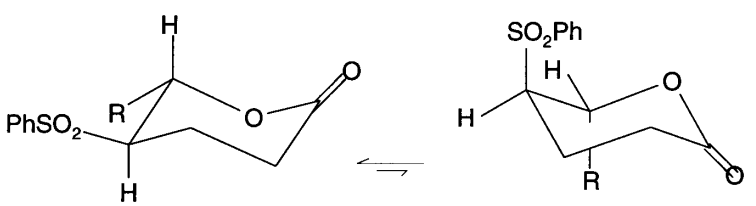

EE *AA*

Remember the configuration shown above for EE and AA conformers are ideal (but naming scheme was used for convenience) and the low energy structures obtained are not exactly same as the ones shown in Scheme V. If phenyl-PSTHP and cyclohexyl-PSTHP convert to a different conformational isomer through conformational inversion (ring flipping) while t-butyl-PSTHP does not go through ring flipping, we may be able

to explain the differences in their reduction potentials. Remember we only searched the lowest energy conformers based on four (ideal) possible chair conformations. For the ring flipping consideration, a more complete structural search such as Monte Carlo simulation should be done. However, the reason that trans conformer of t-butyl-PSTHP doesn't go through this flipping may be attributed to its bulky substituent (t-butyl). A t-butyl group is frequently employed for rigid stereo-chemical control of a ring (Eliel et al., 1965).

If one wants to see the electronic environment before the second electron electrochemical reduction, this is shown in terms of HOMO (highest occupied molecular orbital) in Figure 43. Well developed delocalization of electrons in phenyl ring in the case of phenyl substituted lactone as shown in Figure 43 is observed as it was for phenyl-PSTHP. This can contribute to the observed ease of reduction of the phenyl substituted PSTHP through mitigating the high LUMO of the intact compound.

The spin density map also supplies the information regarding the unpaired electron produced as a result of first electron reduction. The spin density maps for the substituted lactone radicals of interest are shown in Figure 44. The prevailing spin density at the cleaved carbon site of the lactone ring is a good indicator of the distribution of unpaired electron. Notice that there is also spin density development located on phenyl substituent in phenyl substituted radical. This may reflect the ideal representation of the spin density at the highest occupied molecular orbital (HOMO) assuming all electrons except that occupying the highest-energy molecular orbital of a spin are paired. This misleading spin density property can be visualized when we see the

Figure 43. HOMOs of Substituted Lactone Radicals
The calculated HOMO (highest occupied molecular orbital) surfaces are shown for substituted lactone radicals. The geometry of these were obtained by MNDO semiempirical calculations. Then the Hartree-Fock ab-initio calculations with 6-31G* basis set were carried out for the final electronic structure calculations; 1. phenyl-THP (phenyl substituted lactone fragment); 2. cyclohexyl-THP (cyclohexyl substituted lactone fragment); 3. t-butyl-THP (t-butyl substituted lactone fragment). Two different HOMOs for α and β spin states are shown for open shell calculations; (a) α-HOMO; (b) β-HOMO.

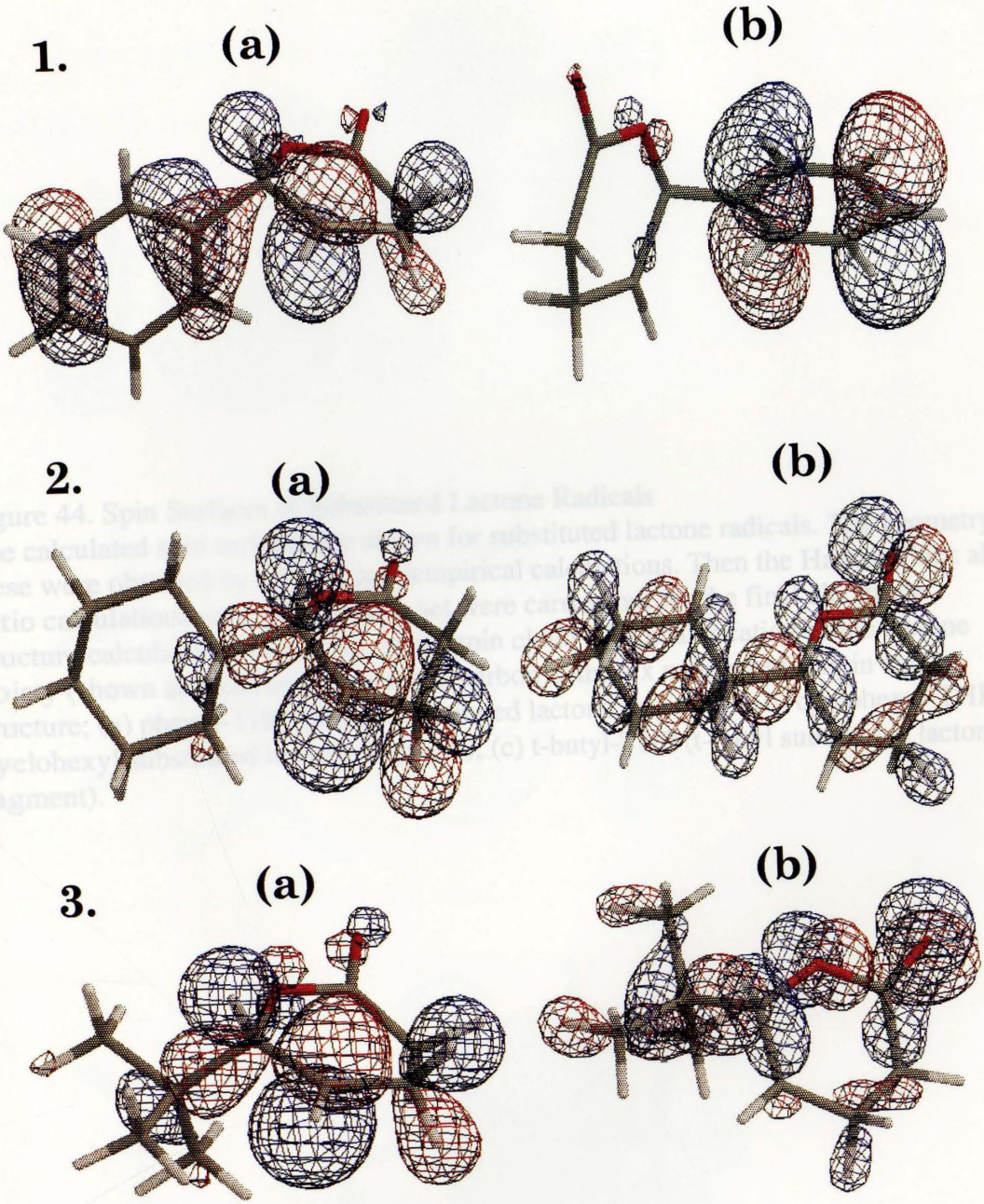
1.
(a)
(b)
2.
(a)
(b)
3.
(a)
(b)

Figure 44. Spin Surfaces of Substituted Lactone Radicals
The calculated spin surfaces are shown for substituted lactone radicals. The geometry of these were obtained by MNDO semiempirical calculations. Then the Hartree-Fock ab-initio calculations with 6-31G* basis set were carried out for the final electronic structure calculations. Notice the major spin cloud at radical location of the lactone moiety (shown as on hydrogen attached carbon at the six membered ring in each structure; (a) phenyl-THP (phenyl substituted lactone fragment); (b) cyclohexyl-THP (cyclohexyl substituted lactone fragment); (c) t-butyl-THP (t-butyl substituted lactone fragment).

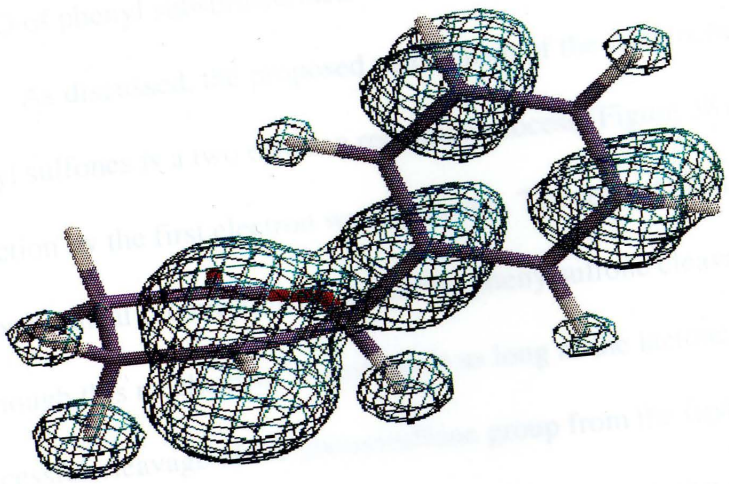

(a)

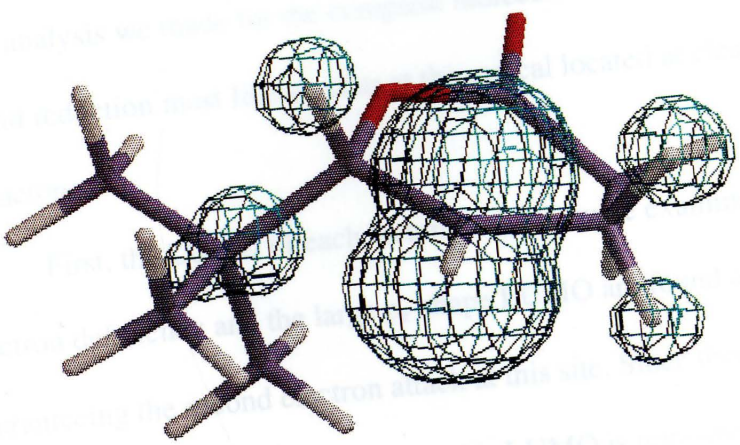

(b)

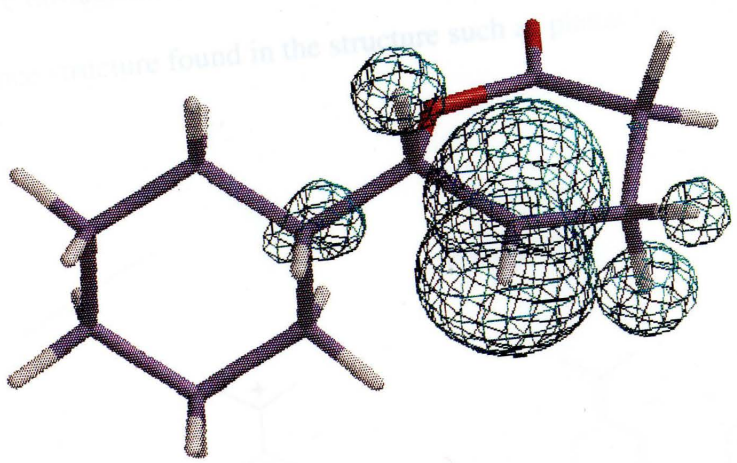

(c)

HOMO of phenyl substituted lactone radical previously presented in Figure 43.

As discussed, the proposed mechanism of the electrochemical cleavage of phenyl sulfones is a two electron reduction process (Figure 38). So far, only the reduction by the first electron was discussed. The second electron was introduced at the lactone radical produced from the earlier phenylsulfone cleavage (step 3 in Figure 38). Although this mechanism is acceptable as long as the lactone ring is intact after successful cleavage of the phenylsulfone group from the first electron reduction, the same analysis we made for the complete molecule was also carried out to examine if the second reduction most likely occur at the radical located at cleavage point to produce the lactone.

First, the LUMO of each lactone radicals were examined as shown in Figure 45. Electron deficiency and the large p_z-shape LUMO are found at the cleaved radical site guaranteeing the second electron attack at this site. Since there is no conjugated π-structure throughout the lactone ring, this LUMO is regiospecific unlike the classical resonance structure found in the structure such as planar benzyl cation shown in Scheme VI.

Scheme VI.

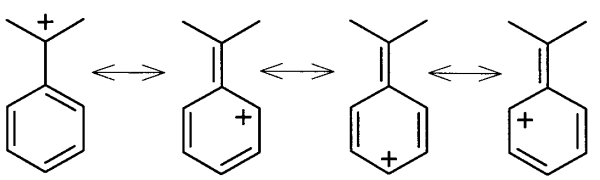

Figure 45. LUMOs of Substituted Lactone Radicals.
The calculated LUMO (lowest unoccupied molecular orbital) surfaces are shown for substituted lactone radicals. The geometry of these were obtained by MNDO semiempirical calculations. Then the Hartree-Fock ab-initio calculations with 6-31G* basis set were carried out for the final electronic structure calculations. Notice the huge unoccupied orbital at the regiospecific radical spot (also shown in Figure 44 for the spin surface) ; (a) phenyl-THP (phenyl substituted lactone fragment); (b) cyclohexyl-THP (cyclohexyl substituted lactone fragment); (c) t-butyl-THP (t-butyl substituted lactone fragment).

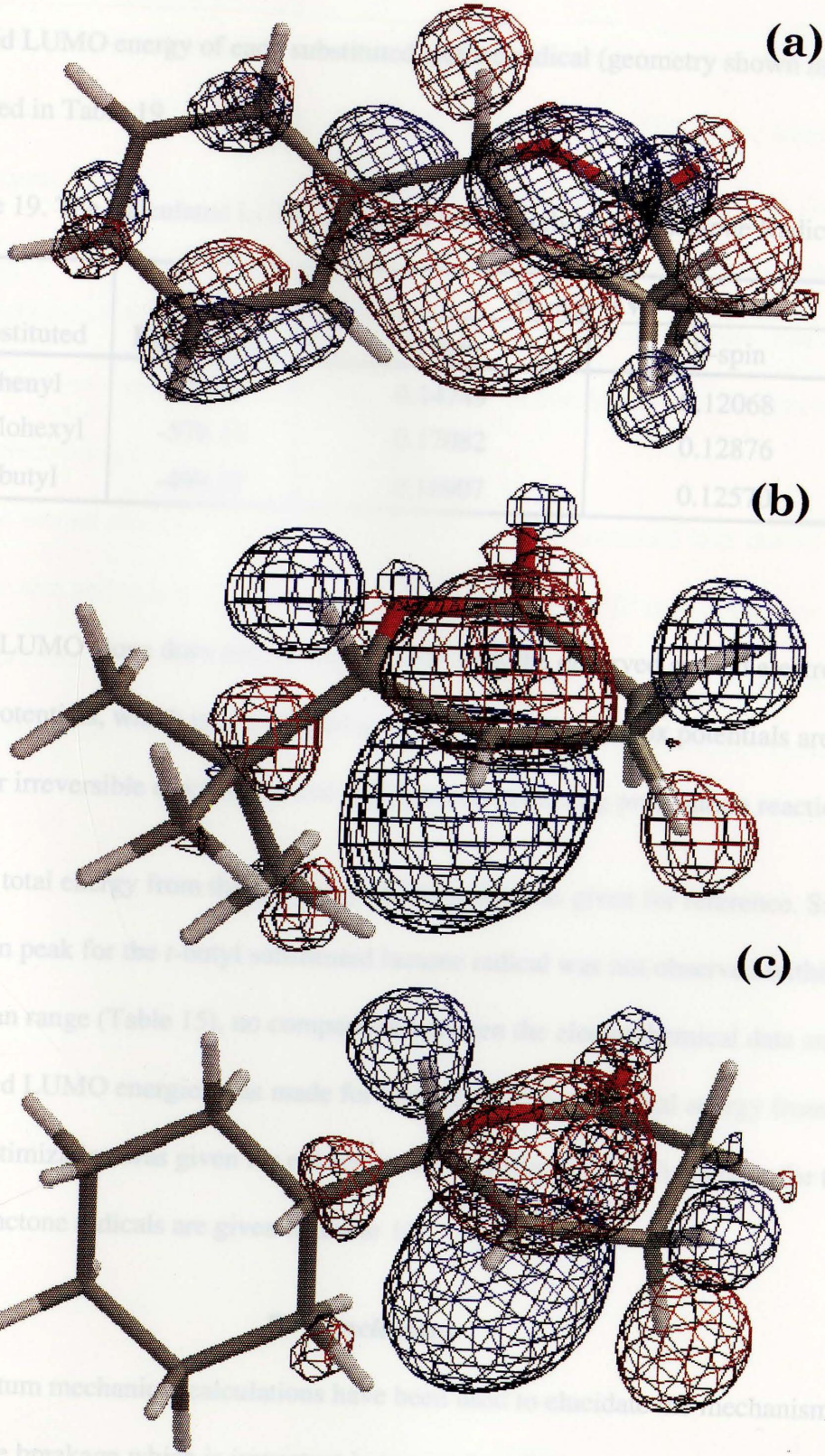
(a)
(b)
(c)

Calculated LUMO energy of each substituted lactone radical (geometry shown in Figure 44) is listed in Table 19.

Table 19. The Calculated LUMO Energies for the Substituted Lactone Radicals

substituted	$E_{hartree}$(a.u.)	E_{LUMO} (eV)	
		α-spin	β-spin
phenyl	-572.64	0.14749	0.12068
cyclohexyl	-576.14	0.17082	0.12876
t-butyl	-499.25	0.16907	0.12570

Again, the LUMO alone does not correspond well with the observed second electron reduction potentials, which is not surprising since these second redox potentials are obtained for irreversible electrochemical (EC) process reflecting protonation reactions.

The total energy from the geometry optimization was given for reference. Since the reduction peak for the *t*-butyl substituted lactone radical was not observed within the potential scan range (Table 15), no comparison between the electrochemical data and the calculated LUMO energies was made for lactone radicals. The total energy from the geometry optimization was given for reference. The calculated LUMO energies for the substituted lactone radicals are given in Table 19.

D. Conclusions

Quantum mechanical calculations have been used to elucidate the mechanism of phenylsulfone breakage which is important in terms of usefulness of the synthetic

technique to produce biologically important lactone. Semiempirical MNDO calculations were used to search the local minima for the possible conformers in cis and trans configurations. Then single point ab-initio calculations were performed to see the electronic environment and orbital energies. The lowest energy structures for phenyl-PSTHP and t-butyl-PSTHP were consistent with the previous NMR results. The two electron reduction steps were examined and found to be consistent with the previously proposed electrochemical cleavage mechanism.

The second electron reduction mechanism was also examined with the *ab*-initio results. The size and shape of LUMO of the each substituted THP radical (lactone radical) was correlated with the regioselective electrochemical reduction of the radicals. The spin density map was also used to identify the distribution of the unpaired electron.

References

Abdo, S.; Canesson, P.; Cruz, M.; Fripiat, J. J.; Damme, H. V. *Journal of Physical Chemistry* **1981**, *85*, 797-809.

Alder, B. J.; Wainwright, T. E. *J. Chem. Phys* **1957**, *27*, 1208.

Alder, B. J.; Wainwright, T. E. *J. Chem. Phys* **1959**, *31*, 459.

Allen, M. P.; Tildesley, D. J. *Computer Simulation of Liquids*; Oxford University Press: New York, 1989.

Artioli, G.; Bellotto, M.; Gualtieri, A.; Pavese, A. *Clays Clay Miner.* **1995**, *43*, 438-445.

Bachrach, S. M. *Reviews in Computational Chemistry* **1994**, *5*, 171-227.

Baizer, M.; Lund, H., **1983**. Organic Electrochemistry.

Bard, A. J.; Mallouk, T., "Electrodes Modified with Clays, Zeolite, and Rlated Microporous Solids," in Molecular Design of Electrode Surfaces, ed. Murray, R. W., Techniques of Chemistry New York: John Wiley & Sons, Inc., 1992., 271-312.

Bartett, R. J.; Stanton, J. F. *Application of Post-Hartree-Fock Methods: A Tutorial*; Bartlett, R. J.; Stanton, J. F., Ed.; VCH Publishers, Inc.: New York, 1994; Vol. 5, pp 65-169.

Berendsen, H. J. C.; Postma, J. P. M.; van Gunsteren, W. F.; Di Nola, A.; Haak, J. R. *J. Chem. Phys* **1984**, *81*, 3684-3690.

Bleam, W. F. *Rev. Geophys.* **1993**, *31*, 51-73.

Boek, E. S.; Coveney, P. V.; Skipper, N. T. *J. Am. Chem. Soc.* **1995b**, *117*, 12608-12617.

Boek, E. S.; Coveney, P. V.; Skipper, N. T. *Langmuir* **1995a**, *11*, 4629-4631

Bohn, H.; McNeal, B.; O'Connor, G. *Soil Chemistry*; John Wiley & Sons, Inc.: New York, **1979**.

Bolt, G. H.; Bruggenwert, M. G. M. *Soil Chemistry: A. Basic Elements*; 2nd ed.; Elsevier Scientific Publishing Company: Amsterdam, 1978; Vol. 5A.

Bonaccorsi, R.; Pullman, A.; Scrocco, E.; Tomasi, J. *Chem. Phys. Lett.* **1972b**, *12*, 622-624.

Bonaccorsi, R.; Pullman, A.; Scrocco, E.; Tomasi, J. *Theoret. Chim. Acta Berl.* **1972a**, *24*, 51-60.

Boyd, D. B., "Aspects of Molecular Modeling," in Reviews in Computational Chemistry, ed. Boyd, D. B. (New York: VCH Publishers Inc., 1990), 321-354.

Breneman, C. M.; Wiberg, K. B. *J. Computational Chem.* **1990**, *11*, 361.

Breu, J.; Catlow, C. R. A. *Inorg. Chem.* **1995**, *34*, 4504-4510.

Broclawlk, E.; Yamauchi, R.; Endou, A.; Kubo, M.; Miyamoto, A. *J. Chem. Phys* **1996**, *104*, 4098-4104.

Burkert, U.; Allinger, N. L. *Molecular Mechanics*; American Chemical Society: Washington, D.C., 1982.

Byrne, K. J.; Swiger, A. A.; Silverstein, R. M.; Borden, J. H.; Stokkink, E. J. *Insect Physiol.* **1974**, *20*, 1895.

Carter, M. T.; Bard, A. J. *J. Electroanal. Chem.* **1987**, *229*, 191.

Catlow, C. R. A.; Gale, J. D.; Gay, D. H.; Lewis, D. W. *Computer modeling of sorption in zeolites*; Catlow, C. R. A.; Gale, J. D.; Gay, D. H.; Lewis, D. W., Ed.; Plenum Press: Michigan State University, East Lansing, Michigan, 1995, pp 241-254.

Cerius2 1.0 User's Reference, Molecular Simulations Inc., **1992**, 152.

Chemistry, ed. Boyd, D. B. New York: VCH Publishers Inc., 1990., 321-354.

Chen, F. H. *Foundations of Expensive Soils*; Elsevier: Amsterdam, New York, N.Y., 1975.

Chen, Y.-W. D.; Santhanam, K. S. V.; Bard, A. J. *J. Electrochem. Soc.* **1982**, *129*, 61.

Chirlian, L. E.; Francl, M. M. *J. Computational Chem.* **1987**, *8*, 894.

Christiano, S. P.; Wang, J.; Pinnavaia, T. J. *Inorg. Chem.* **1985**, *24*, 1222-1227.

Cioslowski, J., "Ab Initio Calculations on Large Molecules: Methodology and Applications," in Reviews in Computational Chemistry, ed. Lipkowitz, K. B. and Boyd, D. B. New York: VCH Publishers, 1993., 1-33.

Clark, T. *A Handbook of Computational Chemistry: A Practical Guide to Chemical Structure and Energy Calculations*; John Wiley & Sons, Inc.: New York, 1985.

Corey, E. J.; Wipke, W. T. *Science* **1969**, *166*, 178.

Crutchley, R. J.; Lever, A. B. P. *Inorg. Chem.* **1982**, *21*, 2276-2282.

Delville, A. *J. Phys. Chem.* **1993**, *97*, 9703-9712.

Delville, A. *J. Phys. Chem.* **1995**, *99*, 2033-2037.

Delville, A. *Langmuir* **1991**, *7*, 547-555.

Delville, A. *Langmuir* **1992**, *8*, 1796-1805.

Delville, A.; Sokolowski, S. *J. Phys. Chem.* **1993**, *97*, 6261-6271.

Dennis Jr., J. E.; Schnabel, R. B. *Numerical Methods for Unconstrained Optimization and Nonlinear Equations*; Prentice-Hall: Englewood Cliffs, N.J., 1983.

Dennis, J.; Schnabel, R. B. *Numerical Methods for Unconstrained Optimization and Nonlinear Equations*; Prentice-Hall: Englewood Cliffs, N.J., 1983.

Derjaguin, B.; Landau, L. D. *Acta Physicochim. URSS* **1941**, *14*, 635.

Dewar, M. J. S.; Jie, C.; Yu, J. *Tetrahedron* **1993**, *23*, 5003.

Dewar, M. J. S.; Thiel, W. *J. Am. Chem. Soc.* **1977**, *99*, 4899-4917.

Dewar, M. J. S.; Zoebisch, E. G.; Healy, E. F.; Stewart, J. J. P. *J. Am. Chem. Soc.* **1985**, *107*, 3902-3909.

Dünweg, B. and K. Kremer, *J. Chem. Phys.*, **1993**, 99, 9, 6983.

Edens, G. J.; Fitch, A.; Lavy-Feder, A. *J. Electroanal. Chem.* **1991**, *307*, 139-154.

Ege, D.; Ghosh, P. K.; White, J. R.; Equey, J. F.; Bard, A. J. *J. Am. Chem. Soc.* **1985**, *107*, 5644.

Eliel, E. L.; Allinger, N. L.; Angyal, S. J.; Morrison, G. A. *Conformational Analysis*; Wiley: New York, 1965.

Ermer, O. *Structure and Bonding* **1976**, *27*, 161-211.

Ernst, S.; Kaim, W. *J. Am. Chem. Soc.* **1986**, *108*, 3578-3586.

Ewald, P. P. *Ann. Phys. Leipzig.* **1921**, *64*, 253.

Fitch, A. *Clays Clay Miner.* **1990**, *38*, 391-400.

Fitch, A. *J. Electroanal. Chem.* **1992**, *332*, 289-295.

Fitch, A., *J. Electroanal. Chem.*, **1990**, 284, 237.

Fitch, A.; Du, J. *Environ. Sci. Technol.* **1996**, *30*, 12-15.

Fitch, A.; Du, J.; Gan, H.; Stucki, J. W. *Clays Clay Miner.* **1995**, *43*, 607-614.

Fitch, A.; Fausto, C. L. *J. Electroanal. Chem.* **1988**, *257*, 299-303.

Fitch, A.; Fausto, C. L., *J. Electroanal. Chem.* 1988, *257*, 299.

Fitch, A.; Krzysik, R. J. *J. Electroanal. Chem.* **1993**, *379*, 129-134.

Fitch, A.; Lavy-Feder, A.; Lee, S. A.; Kirsh, M. T. *J. Phys. Chem.* **1988**, *92*, 6665-6670.

Fitch, A.; Lee, S. *J. Electroanal. Chem.* **1993**, *344*, 45-59.

Fitch, A.; Song, J.; Stein, J. *Clays Clay Miner.* **1996**, *44*, 370-380.

Fitch, A.; Subramanian, P. Fitch *J. Electroanal. Chem.* **1993**, *362*, 177-184.

Fletcher, R. *Practical Methods of Optimization*; 2nd ed.; John Wiley & Sons: Tiptree, Essex, United Kingdom, 1987.

Fletcher, R.; Reeves, C. M. *Comput. J.* **1964**, *7*, 149.

Fu, M. H.; Zhang, Z. Z.; Low, P. F. *Clays Clay Miner.* **1990**, *38*, 485-492.

Getzoff, E. D.; Tainer, J. A.; Weiner, P. K.; Kollman, P. A.; Richardson, J. S.; Richardson, D. C. *Nature* **1983**, *306*, 287-290.

Ghosh, P. K.; Bard, A. *J. Am. Chem. Soc.* **1983**, *105*, 5691.

Giannelis, E. P.; Pinnavaia, T. J. *Inorg. Chem.* **1985a**, *24*, 2115-2118.

Giannelis, E. P.; Pinnavaia, T. J. *Inorg. Chem.* **1985b**, *24*, 3602-3607.

Gibbs, G. V. *Am. Mineral.* **1982**, *67*, 421-450.

Gill, P. E.; Murray, W.; Wright, M. H. *Practical Optimization*; Academic Press: New York, 1983.

Guggenheim, S.; Martin, R. T. *Clays Clay Miner.* **1995**, *43*, 255-256.

Güven, N. *Rev. Mineral.* **1988**, *19*, 497-559.

Haan, F. A. M. d.; Zwerman, P. J., "Pollution of soil." in Soil Chemistry, A Basic Element, ed. Bolt, G. H. and Bruggenwert, M. G. M. Amsterdam, New York: Elsevier, 1976., 192-196.

Hagler, A. T. *Theoretical simulation of conformation, energetics, and dynamics of peptides*; Meienhofer, J., Ed.; Academic Press: New York, 1985, pp 213-299.

Haile, J., Molecular Dynamics Simulations: Elementary Methods, John Wiley, **1992**, 296-297.

Hanazaki, I.; Hanazaki, F.; Nagakura, S. *J. Chem. Phys.* **1969**, *50*, 265.

Hartree, D. R. *The Calculation of Atomic Structures*; Wiley: New York, 1957.

Hehre, W. J.; Radom, L.; Schleyer, P. v. R.; Pople, J. A. *Ab Initio Molecular Orbital Theory*; John Wiley & Sons: New York, 1986.

Hehre, W. J.; Burke, L. D.; Shusterman, A. J.; Pietro, W. J. *Experiments in Computational Organic Chemistry*; Wavefunction, Inc.: Irvine, CA, 1993.

Hetzel, F.; Tessier, D.; Jaunet, A.-M.; Doner, H. *Clays Clay Miner.* **1994**, *42*, 242-248.

Hoh, Y.-C. *J. Nucl. Sci. Technol.* **1992**, *29*, 131-139.

Holthausen, M. C.; Fiedler, A.; Schwarz, H.; Koch, W. *Journal of Physical Chemistry* **1996**, *100*, 6236-6242.

Hoover, W. H., *Phys. Rev. A.*, **1985**, 31, 1695.

Hopfinger, A. J. *Conformational Properties of Macromolecules*; Academic Press: New York, 1973.

Israelachvili, J. N. *Intermolecular and Surface Forces*; Academic Press: London, 1985.

Itaya, K.; Bard, A. J. *J. Phys. Chem.* **1985**, *89*, 5565.

Jayaran, B.; Beveridge, D. L. *J. Phys. Chem.* **1990**, *94*, 4666.

Joo, P.; Fitch, A. *Environ. Sci. Technol.* **1996**, *30*, 2681-2686.

Jorgensen, W. L.; Chandrasekhar, J.; Madura, J. D.; Impey, R. W.; Klein, M. L. *J. Chem. Phys.* **1983**, *79*, 926-935.

Jung, C.; Ristau, O.; Jung, C. *Theoret. Chim. Acta Berl.* **1983**, *63*, 143-159.

Karaborni, S.; Smit, B.; Heidug, W.; Urai, J.; Oort, E. v. *Science* **1996**, *271*, 1102-1104.

Karasawa, N.; Goddard, W. A. *J. Phys. Chem.* **1989**, *93*, 7320.

Keldsen, G. L.; Nicholas, J. B.; Carrado, K. A.; Winans, R. E. *J. Phys. Chem.* **1994**, *98*, 279-284.

Kennard, O., Cambridge Crystallographic Data Centre, University Chemical Laboratory, Lansfield Road, Cmbridge, CBZ 1 EW, UK.

Kijima, T.; Tanaka, J.; Goto, M.; Matsui, Y. *Nature* **1984**, *310*, 45-47.

Kohn, W.; Sham, L. J. *Phys. Rev.* **1965**, *140*, A1133.

Krumholtz, P. *Structure and Bonding* **1971**, *9*, 139.

Laird, D. A. *Clays Clay Miner.* **1996**, *44*, 553-559.

Lamm, B.; Simonet, J. *Acta Chem. Scand.* **1974**, *B. 28*, 147.

Lee, S. A.; Fitch, A. *J. Phys. Chem.* **1990**, *94*, 4998-5004.

Lee, S. Y.; Tank, R. W. *Appl. Clay Sci.* **1985**, *1*, 145-162.

Lee, S.A.; Fitch, A., *J. Phys. Chem.* 1990, *94*, 4998.

Lewis, D. F. F., "Computer-Assisted Methods in the Evaluation of Chemical Toxicity," in Reviews in Computational Chemistry 1992., 173-222.

Li, J.; Schreckenbach, G.; Ziegler, T. *J. Am. Chem. Soc.* **1995**, *117*, 486-494.

Liebmann, P.; Loew, G.; Rurt, S.; Lawless, J.; MacElroy, R. D. *Inorg. Chem.* **1982**, *21*, 1586-1594.

Lippman, S. B. C++ Primer; 2nd ed.; Addison-Wesley Publishing Company: New York, 1993.

Liu, H. Y.; Anson, F. C. *J. Electroanal. Chem.* **1985**, *184*, 411.

Lohr Jr., J. E., M.S. Thesis, Loyola University of Chicago, 1996.

Low, P. F.; Cushman, J. H.; Diestler, D. J.; Mulla, D. J. *Journal of Colloid and Interface Science* **1984**, *100*, 576-580.

Löwdin, P.-O. *Adv. Quantum Chem.* **1970**, *5*, 185.

Macha, S. M.; Fitch, A. submitted for publication in *Mikrochim. Acta* **1997**.

Maegdefrau, E. Hoffmann, U. *Z Kristallgr., Kristallgeom., Kristallphys. Kristallchem,* **1937**, 98-299.

Magda, J. J., M. Tirrell, and H. T. Davis, *J. Chem. Phys.*, **1983**, 83, 4, 1888-1900.

Magee, B. R.; Lion, L. W.; Lemley, A. T. *Environ. Sci. Technol.* **1991**, *25*, 323-331.

Manoušek, O.; Exner, O.; Zuman, P. *Collection Czechoslov. Chemical Communications* **1968**, *33*, 3988.

Mathiowetz, A. M., Ph.D. Thesis, California Institute of Technology, 1993.

Matsouka, O.; Clementi, E.; Yoshimine, M. *J. Chem. Phys.* **1976**, *64*, 1351-1361.

Mayer, I. *Chem. Phys. Lett.* **1983**, *97*, 270.

Mayer, I. *Chem. Phys. Lett.* **1984**, *110*, 440.

McCammon, J. A.; Gelin, B. R.; Karplus, M. *Nature* **1977**, *267*, 585-90.

Mercier, l.; Detellier, C. *Environ. Sci. Technol.* **1995**, *29*, 1318-1323.

Metropolis, N.; Rosenbluth, A. W.; Rosenbluth, M. N.; Teller, A. H.; Teller, E. *J. Chem. Phys* **1953**, *21*, 1087-92.

Meites, L.; Zuman, P. *Handbook Series in Organic Electrochemistry*; CRC Press: Cleveland, Ohio, 1977; Vol. I and II.

Mooney, R. W.; Keenan, A. G.; Wood, L. A. *J. Am. Chem. Soc.* **1952**, *74*, 1367-1371.

Mooney, R. W.; Keenan, A. G.; Wood, L. A. *J. Am. Chem. Soc.* **1952**, *74*, 1371-1374.

Moore, D. M.; Robert C. Reynolds, J. *X-Ray Diffraction and the Identification and Analysis of Clay Minerals*; Oxford University Press: New York, **1989**

Mori, K. *Tetrahedron* **1975**, *31*, 3011.

Morrell, W. E.; Hildebrand, J. H. *J. Chem. Phys* **1936**, *4*, 224-27.

Müller-Plathe, F, S.C. Rogers, W. F. van Gunsteren, *J. Chem. Phys.* **1993**, 98, 2, 9895.

Mulliken, R. S. *J. Chem. Phys* **1955a**, *23*, 1833.

Mulliken, R. S. *J. Chem. Phys* **1955b**, *23*, 1841.

Mulliken, R. S. *J. Chem. Phys* **1955c**, *23*, 2338.

Mulliken, R. S. *Life of a Scientist*; Springer-Verlag: Berlin, 1989.

Murray, R. W., ed. Molecular Design of Electrode Surfaces, ed. Saunders Jr., W. H., Techniques of Chemistry, vol. 22 New York: John Wiley & Sons, Inc., 1992.

Naegeli, R., Redepenning, J., Anson, F. C., *J. Phys. Chem.* **1986**, 90, 6227.

Newman, A. C. D., ed. Chemistry of Clays and Clay Minerals, ed. Society, M., Monograph, vol. 6 New York: John Wiley & Sons, 1987.

Newton, M. D.; Gibbs, G. V. *Phys. Chem. Minerals* **1980**, *6*, 221-246.

Nosé, S. J. *J. Chem. Phys* **1984**, *91*, 511.

Nosé, S. J. *Mol. Phys.* **1984**, *52*, 255.

O'Keeffe, M.; Brese, N. E. *J. Am. Chem. Soc.* **1991**, *113*, 3226.

Overcash, M. R.; McPeters, A. L.; Dougherty, E. J.; Carbonell, R. G. *Environ. Sci. Technol.* **1991**, *25*, 1479-1485.

Park, S.-H., "Theoretical Investigation of the Pi-Bonding Ability of P-, S-, and N-Containing Ligands in Group VI Transition Metal Complexes" Eastern Michigan University, 1994.

Pauling, L. *The Nature of the Chemical Bond*; Cornell University Press: Ithaca, New York, 1960, p. 239.

Petridis, D.; Falaras, P.; Pinnavaia, T. J. *Inorg. Chem.* **1991**, *31*, 3530-3533.

Pietro, W. J. ; Hehre, W. J, *J. Comput. Chem.*, **1983**, 4, 241.

Pople, J. A.; Beveridge, D. L. *Approximate Molecular Orbital Theory*; McGraw-Hill: New York, 1970.

Pople, J. A.; Nesbet, R. K. *J. Chem. Phys* **1954**, *22*, 571.

Rabinowitch, E.; Wood, W. C. *Trans. Faraday Soc.* **1936**.

Rappé, A. K.; Goddard, W. A. *J. Phys. Chem.* **1991**, *95*.

Rappé, A. K.; Casewit, C. J.; Colwell, K. S. *J. Am. Chem. Soc.* **1992**, *114*, 10046-10053.

Rappé, A. K.; Casewit, C. J.; Colwell, K. S.; Goddard, W. A.; Skiff, W. M. *J. Am. Chem. Soc.* **1992**, *114*, 10024-10035.

Rappé, A. K.; Colwell, K. S.; Casewit, C. J. *Inorg. Chem.* **1993**, *32*, 3438-3450.

Rappé, A. K.; Goddard III, W. A. *J. Phys. Chem.* , submitted.

Reed, A. E.; Weinstock, R. B.; Weinhold, F. *J. Chem. Phys* **1985**, *83*, 735-746.

Reynolds, C. A.; Ferenczy, G. G.; Richards, W. G. *J. Mol. Struct.* **1992**, *256*, 249.

Rillema, D. P.; Allen, G.; Meyer, T. J.; Conrad, D. *Inorg. Chem.* **1983**, *22*, 1617-1622.

Rillema, D. P.; Jones, D. S.; Woods, C.; Levy, H. A. *Inorg. Chem.* **1992**, *31*, 2935-2938.

Rong, D.; Kim, Y. I.; Mallouk, T. E. *Inorg. Chem.* **1990**, *29*, 1531-1535.

Roos, B. *Acta Chem. Scand.* **1966**, *20*, 1673.

Rudzinski, W. E.; Bard, A. J. *J. Electroanal. Chem.* **1986**, *199*, 323.

Ruminski, R. R.; Petersen, J. D. *Inorg. Chim. Acta* **1984**, *88*, 63-66.

Ruminski, R. R.; Petersen, J. D. *Inorg. Chim. Acta* **1985**, *97*, 129-134.

Sanders, N. *J. Chem. Soc., Dalton Trans.* **1972**, 345.

Sato, H.; Yamagishi, A.; Kato, S. *J. Am. Chem. Soc.* **1992a**, *114*, 10933-10940.

Sato, H.; Yamagishi, A.; Kato, S. *Journal of Physical Chemistry* **1992b**, *96*, 9377-9382.

Sato, H.; Yamagishi, A.; Naka, K.; Kato, S. *1996* **1996**, *100*, 1711-1717.

Schrader, M. E.; Loeb, G. I. *Modern Approaches to Wettability: Theory and Applications*; Plenum Press: New York, 1992.

Schwertmann, U.; Taylor, R. M., "Iron oxides," in Minerals in Soil Environments, ed. Dixon, J. B. and Weed, S. B. Madison, Wisconsin: Soil Sci. Soc. Am., 1977., 145-176.

Serne, R. J.; Rai, D.; Mason, M. J.; Molecke, M. "K_d Measurements of Nuclides to Estimate Migration Potential as the Proposed Waste Isolation Pilot Plant in New Mexico," Pacific Northwest Laboratory, 1977.

Shang, C.; Thompson, M. L.; Laird, D. A. *Clays Clay Miner.* **1995**, *43*, 128-130.

Skipper, N. T.; Chang, F.-R. C.; Sposito, G. *Clays Clay Miner.* **1995a**, *43*, 285-293.

Skipper, N. T.; Refson, K.; McConnell, J. D. C. *Clay Minerals* **1989**, *24*, 411-425.

Skipper, N. T.; Refson, K.; McConnell, J. D. C. *J. Chem. Phys.* **1991**, *94*, 7434-7445.

Skipper, N. T.; Sposito, G.; Chang, F.-R. C. *Clays Clay Miner.* **1995b**, *43*, 294-303.

Slade, P. G.; Quirk, J. P.; Norrish, K. *Clays Clay Miner.* **1991**, *39*, 234-238.

Smith, J. A.; Jaffè, P. R. *Water, Air, and Soil Pollution* **1994**, *72*, 205-211.

Snook, I.; van Megen, W. *J. Chem. Phys.* **1979**, *70*, 3099-3105.

Spartan 3.0 Computer Modeling Software, Wavefunction, Inc., **1993.**

Sposito, G. *The Chemistry of Soils*; Oxford University Press: New York, 1989.

Stein, J. A.; Fitch, A. *Anal. Chem.* **1995**, *67*, 1322-1325.

Stein, J. A.; Fitch, A. *Clays Clay Miner.* **1996**, *44*, 381-392.

Stein, J. A.; Fitch, A. *Electroanalysis* **1994**, *6*, 23-28.

Stewart, J. J. P. *J. Comput. Chem.* **1989a**, *10*, 209-220.

Stewart, J. J. P. *J. Comput. Chem.* **1989b**, *10*, 221-264.

Subramanian, P.; Fitch, A. *Environ. Sci. Technol.* **1992**, *26*, 1775-1779.

Sullivan, D. E. *J. Chem. Phys.* **1980**, *72*, 1170-1174.

Sullivan, D. E.; Stell, G. *J. Chem. Phys.* **1978**, *69*, 5450-5457.

Swope, W. C.; Andersen, H. C.; Berens, P. H.; Wilson, K. R. *Phys. Rev.* **1982**, *76*, 637-649.

Taniguchi, M.; Yamagishi, A.; Iwamoto, T. *Inorg. Chem.* **1991**, *30*, 2462-2467.

Thompson, C. M. *Tetraheron Letters* **1987**, *28*, 4243-4246.

Torrie, G. M.; Kusalik, P. G.; Patey, G. N. *J. Chem. Phys.* **1988**, *89*, 3285-3294.

van Olphen, H. *An Introduction to Clay Colloid Chemistry*; 2nd ed.; Drieger Publishing Company: Malabar, Florida, 1991.

Verlet, L. *Phys. Rev.* **1967**, *159*, 98-103.

Verwey, E. J. W.; Overbeek, J. T. G. *Theory of the Stability of Lyophobic Colloids*; Elsevier: New York, 1948.

Wagner, J.; Chen, H.; Brownawell, B. J.; Westall, J. C. *Environ. Sci. Technol.* **1994**, *28*, 231-237.

Wang, Y.; Fitch, A.; Park, S.-H., *J. Phys. Chem.* **1997**, submitted.

Xu, S.; Boyd, S. A. *Environ. Sci. Technol.* **1995**, *29*, 312-320.

Xu, X.; Nieber, J. L.; Gupta, S. C. *Soil Sci. Soc. Am. J.* **1992**, *56*, 1743-1750.

Yamagishi, A. *Inorg. Chem.* **1985**, *24*, 1689-1695.

Yamagishi, A. *Inorg. Chem.* **1985**, *24*, 1689-1695.

Yamagishi, A. *J. Chem. Soc., Dalton Trans.* **1983**, 679-681.

Yamagishi, A. *Journal of Physical Chemistry* **1982**, *86*, 2472-2479.

Yamagishi, A.; Soma, M. *J. Am. Chem. Soc.* **1981**, *103*, 4640-4642.

Yamanaka, S.; Okumura, M.; Yamaguchi, K.; Hirao, K. *Chem. Phys. Lett.* **1994**, *225*, 213-220.

Zerner, M. C., "Semiempirical Molecular Orbital Methods," in Reviews in Computational Chemistry, ed. Lipkowitz, K. B. and Boyd, D. B. New York: VCH Publishers, Inc., 1991., 313-365.

Zhang, Z. Z.; Sparks, D. L.; Scrivner, N. C. *Environ. Sci. Technol.* **1993**, *27*, 1625-1631.

VITA

The author, Sung-Ho Park, was born on May 28, 1964, in Seoul, Korea. He did his undergraduate studies at Sogang University in Korea and obtained his Bachelor of Science degree with a major in Chemistry and with a minor in Physics on February 15, 1988. He started his studies at Eastern Michigan University in 1989 and received his Masters of Science degree in Chemistry with the emphasis on Physical Chemistry in 1992. During this time, he was working as a teaching assistant for chemistry and biochemistry laboratory classes. He was awarded EMU CORE Grant for his excellence in graduate research. He entered Ph.D. program in Chemistry at Loyola University of Chicago in 1992. He joined Dr. Fitch's analytical physical chemistry group and was supported by a research assistantship funded by her NSF grant for the clay diffusion study until he finished his Ph.D. in 1997. He has been a member of the American Chemical Society since January 1992.

The dissertation submitted by Sung-Ho Park has been read and approved by the following committee:

Fitch A., Ph.D., Director
Professor, Chemistry
Loyola University Chicago

Olsen K., Ph.D.
Professor and Chair, Chemistry
Loyola University Chicago

Herlinger A. W., Ph.D.
Associate Professor, Chemistry
Loyola University Chicago

Greene-Johnson W., Ph.D.
Assistant Professor, Chemistry
Loyola University Chicago

Schatz G. C., Ph.D.
Professor, Chemistry
Northwestern University

The final copies have been examined by the director of the Committee and the signature which appears below verifies the fact that any necessary changes have been incorporated and that the dissertation is now given final approval by the committee with reference to content and form.

The dissertation is, therefore, accepted in partial fulfillment of the requirements for the degree of doctor of philosophy.

4/10/97
Date

Director's Signature